SYNTHESIS AND CHARACTERISATION OF HYDROTHERMALLY TREATED AND FUNCTIONALISED ZINC AND ALUMINIUM SURFACES

Anže Abram

Doctoral Dissertation
Jožef Stefan International Postgraduate School
Ljubljana, Slovenia

Supervisor: Asst. Prof. Dr. Goran Dražić, IPS, Jožef Stefan Institute and National Institute of Chemistry, Ljubljana, Slovenia

Evaluation Board:
Asst. Prof. Dr. Nina Daneu, Chair, IPS, Jožef Stefan Institute, Ljubljana, Slovenia
Asst. Prof. Dr. Srečo Davor Škapin, Member, IPS, Jožef Stefan Institute, Ljubljana, Slovenia
Prof. Dr. Urška Lavrenčič Štangar, Member, Faculty of Chemistry and Chemical Technology, University of Ljubljana, Slovenia

MEDNARODNA PODIPLOMSKA ŠOLA JOŽEFA STEFANA
JOŽEF STEFAN INTERNATIONAL POSTGRADUATE SCHOOL



Anže Abram

SYNTHESIS AND CHARACTERISATION OF HYDROTHERMALLY TREATED AND FUNCTIONALISED ZINC AND ALUMINIUM

Doctoral Dissertation

SINTEZA IN KARAKTERIZACIJA HIDROTERMALNO OBDELANIH IN FUNKCIONALIZIRANIH POVRŠIN CINKA IN ALUMINIJA

Doktorska disertacija

Supervisor: Asst. Prof. Dr. Goran Dražić

Ljubljana, Slovenia, January 2017

If you are lonely when you are alone, you are in bad company.

- S.

Acknowledgments

Firstly, I would like to thank my PhD supervisor Asst. Prof. Dr. Goran Dražić, for his guidance and valuable discussions during my work, for the encouragement, understanding and support during my postgraduate study at the Jožef Stefan Institute.

I would like to thank Prof. Dr. Klemen Bohinc and his colleagues Asst. Prof. Dr. Mojca Jevšnik and Damijan Nipič from the Faculty of Health Sciences, University of Ljubljana, for their continuing collaboration on surface characterisation and bacterial adhesion.

My thanks also go to Bojan Ambrožič (Department for Nanostructured Materials, Jožef Stefan Institute) for his help with the FIB scanning electron microscope work, Andreja Eršte (Condensed Matter Physics, Jožef Stefan Institute) for her dielectric measurements and Dejan Klement (Advanced Materials Department, Jožef Stefan Institute) for his work on the Empyrean diffractometer XRD system, as well as Slovenian industrial partners in our projects: Cinkarna Celje, Impol Slovenska Bistrica, Iskra Pio, Iskra Semič (PE Kondenzatorji) and Steklarna Hrastnik.

I would like to thank my colleagues at the Department for Nanostructured Materials for all their support and the nice moments that we have shared together over the past four years, especially Luka Suhadolnik, Martina Lorenzetti, Matic Krivec and Barbara Horvat for the discussions regarding TiO_2. I would like to express my gratitude to the members of the Center for Electron Microscopy and microanalysis (CEMM), Dr. Janez Zavašnik, Andreja Šestan and Maja Koblar for the discussions about sample preparation and SEM/TEM imaging.

Special thanks go to Manca Krošelj and Žiga Abram for the help with illustrations and graphics.

Finally, I would like to thank my family for their support, encouragement and patience.

Abstract

Fabrication and design of functionalised coatings on metals is attractive because of the wide range of applications and consequently the large impact such materials potentially have. In my work I evaluated the possibilities of hydro- and solvothermal treatment along with simple post-processing methods on metallic aluminium and zinc to obtain new materials with novel or improved properties, such as self-cleaning, superhydrophilicity, superhydrophobicity, photocatalytic degradation of organics and dielectric properties. These improved properties were achieved by the formation of nano- and micro-sized coatings of titanium dioxide (TiO_2), zinc oxide (ZnO) and aluminium oxide hydroxide – boehmite (γ-AlO(OH)) that were prepared in general-purpose autoclaves at temperatures up to 200 °C in deionised water, ethanol and isopropyl alcohol with precursors for Ti (titanium(IV) isopropoxide) and Zn (zinc nitrate hexahydrate, zinc acetate dihydrate) ions. Two and three-layer structures were hydrothermally prepared on aluminium sheet, either with 1.5–2 μm thick boehmite layer or with boehmite and nanolayer of photoactive TiO_2. Dielectric response was measured on the aluminium/boehmite system and was found to be very stable with ε' values in the range from 5.5 to 6.5 over broad temperature (275–350 K) and frequency (1 kHz–1 MHz) ranges. TiO_2 coated aluminium substrates were characterised for photocatalytic activity towards 10 ppm caffeine solution. Hydrothermally prepared TiO_2 powder achieved comparable degradation rates to Degussa P 25 reference. As expected, immobilised TiO_2 samples achieved lower degradation rates than the powder sample, but offer great improvement in catalyst handling, secondary pollution by erosion of photocatalyst into the environment while still retaining comparable efficiency. Hydro- and solvothermal treatment on zinc results in a formation of a diverse range of ZnO morphologies depending on synthesis conditions, solvent and precursor used, and additives. 50–100 nm thick ZnO needles, growing from the same base, form hedgehog-like structures that significantly increase the surface of the substrate and offer the base for preparation of superhydrophobic materials in conjunction with dip-coating in fluoroalkyl oligosiloxane. I showed that such superhydrophobic zinc surfaces exhibit no adhesion of *E. coli* bacteria.

Povzetek

Funkcionalizacija kovinskih materialov s površinsko obdelavo je široko uporaben in zanimiv pristop, s katerim lahko z nanotehnologijo povezane lastnosti implementiramo na široki paleti materialov in produktov. Raziskal sem možnosti uporabe hidro- in solvotermalne sinteze za pripravo funkcionalnih prevlek na aluminiju in cinku z novimi lastnostmi, kot so samočistilnost, superhidrofilnost, superhidrofobnost, fotokatalitičnost, ter izboljšanimi dielektričnimi lastnostmi. Nove lastnosti sem dosegel s pripravo nano- in mikrometerskih plasti titanovega dioksida (TiO_2), cinkovega oksida (ZnO) in aluminijevega oksihidroksida – bemita (γ-AlO(OH)) v avtoklavih pri temperaturah do 200 °C v deionizirani vodi, etanolu ter izopropanolu, skupaj s prekurzorji za Ti (titanov(IV) izopropoksid) in Zn (cinkov nitrat heksahidrat, cinkov acetat dihidrat) ione. S hidrotermalno obdelavo substratov iz aluminija sem pripravil dvo- ter tro-slojno plastovito strukturo na površini, sestavljeno iz 1,5–2 μm debele bemitne plasti in nanoplasti fotoaktivnega TiO_2. Dielektrični odziv na z bemitom prekrito aluminijevo folijo je stabilen z dielektrično konstanto ε' med 5,5 in 6,5 v širokem temperaturnem (275–350 K) in frekvenčnem (1 kHz–1 MHz) območju. Meritve fotokatalitične razgradnje kofeina sem opravili na hidrotermalno pripravljenem prahu ter na aluminijevem substratu, prevlečenem z nanoplastjo TiO_2 in komercialno dostopnim Degussa P 25 prahom kot referenco. Imobiliziran TiO_2 pričakovano počasneje razgrajuje kofein kot TiO_2 prah, predvsem zaradi manjše aktivne površine. Kljub nižji fotoaktivnosti so imobilizirane TiO_2 prevleke velikega pomena zaradi enostavnosti uporabe, predvsem pri ločevanju aktivne substance od medija, manjšega sekundarnega onesnaževanja okolja z odrabljenimi fotokatalitičnimi materiali ter drugih. Pri hidro- in solvotermalni obdelavi cinka se na površini ustvari plast cinkovega oksida (ZnO), katere morfologija je zelo odvisna od pogojev sinteze (čas, temperatura, polnitev avtoklava) ter sestave začetne raztopine (pH, tip in količina Zn prekurzorja). S pravilnim postopkom lahko pripravimo plast 50–100 nm velikih ZnO iglic, ki rastejo iz skupne osnove in ustvarjajo ježasto strukturo. S tem se bistveno poveča specifična površina substrata, ki jo lahko uporabimo kot osnovo pri pripravi superhidrofobnih površin v kombinaciji s fluoroalkil oligosiloksani. Pokazali smo, da take površine onemogočijo adhezijo bakterij (na primeru *E. coli*), kar je velikega pomena v medicini in prehrambni industriji.

Contents

List of Figures **xv**

List of Tables **xix**

Abbreviations **xxi**

Symbols **xxiii**

1 Introduction **1**
1.1 Overview ... 1
1.2 Nanomaterials ... 2
1.2.1 Semiconducting nanomaterials ... 4
1.2.1.1 Synthesis methods ... 5
1.2.1.2 Hydro- and solvothermal synthesis ... 5
1.2.2 Immobilisation of nanoparticles ... 8
1.2.2.1 Methods of immobilisation ... 8
1.3 Aluminium ... 8
1.3.1 Passivation of aluminium ... 9
1.3.2 Aluminium under hydrothermal conditions ... 10
1.4 Zinc ... 11
1.4.1 Zinc oxide ... 11
1.4.2 Hydrothermal treatment and ZnO nanostructures ... 12
1.5 Stainless steel ... 13
1.6 Functionalised Coatings on Metals ... 14
1.6.1 Photocatalytic coatings ... 14
1.6.1.1 Titanium dioxide - TiO_2 ... 16
1.6.1.2 Synthesis of TiO_2 nanoparticles and coatings ... 17
1.6.1.3 Primary processes upon irradiation of TiO_2 ... 18
1.6.1.4 Determination of TiO_2 photodegradation efficiency ... 20
1.6.2 Coatings and surface wettability ... 21
1.6.2.1 Superhydrophilicity of TiO_2 coatings ... 25
1.6.2.2 Superhydrophobicity (Lotus effect) on ZnO coatings ... 27
1.6.3 Coating with improved dielectric response ... 28
1.6.4 Bacteriostatic coatings ... 29
1.6.4.1 Direct bacteria attachment determination methods ... 29
1.6.4.2 Indirect bacteria attachment determination methods ... 30

2 Aims and Hypothesis **33**

3 Materials and Methods **35**
3.1 Processing and Sample Preparation ... 35
3.1.1 Chemicals and Materials ... 35

3.1.2 Sol preparation 36
3.1.3 Hydro- and solvothermal conditions 36
3.1.4 Other pre- and post-treatment processes 36
3.1.4.1 Dip-coating and annealing 36
3.1.4.2 Abrasion treatment 37
3.1.4.3 Surface plasma treatment 37
3.2 Characterisation 38
3.2.1 X-ray powder diffraction (XRD) and low-angle Empyrean XRD 38
3.2.2 Surface metrology (AFM, Profilometer) 38
3.2.3 Scanning electron microscopy (SEM) and FIB 39
3.2.4 Transmission electron microscopy (TEM) 40
3.2.5 Dielectric measurements 41
3.2.6 Photocatalytic measurements 41
3.2.7 Contact angle and hydrophobicity measurements 43
3.2.8 Bacteria counting for adhesion determination 44

4 Results and Discussion 45
4.1 Aluminium 45
4.1.1 Structural and morphological properties 45
4.1.1.1 Hydro and solvothermally treated aluminium 46
4.1.1.2 Addition of titanium precursor to HT of aluminium 49
4.1.2 Surface topology, roughness and contact angle measurements 57
4.1.3 Photocatalytic activity 59
4.1.4 Dielectric response 60
4.2 Zinc 64
4.2.1 Structural and morphological properties 64
4.2.1.1 Hydrothermally treated zinc 64
4.2.1.2 Solvothermally treated zinc 67
4.2.2 Superhydrophobic coating on ZnO 69
4.3 Bacterial Adhesion to Zinc and Steel Substrates 70
4.3.1 Roughness and contact angle measurements 70
4.3.2 Bacterial adhesion to surfaces of different roughness 72
4.3.3 Bacterial adhesion to surfaces of different contact angle 74

5 Conclusions 77

References 79

Bibliography 87

Biography 89

List of Figures

Figure 1.1: Schematic representation of two main approaches in nanotechnology: top-down and bottom-up. 3
Figure 1.2: Absolute conduction band and valence band energy levels of potential semiconductors versus the standard electrochemical potential scale and the vacuum energy scale [17]. 4
Figure 1.3: General-purpose autoclave with Teflon inner capsule as used in my experimental work. 6
Figure 1.4: Correlation of pressure and temperature for pure water, with the degree of filling of the sealed autoclave as a parameter. Pressures up to 2000 bar are achieved with filling factors between 50 and 80% [22]. 6
Figure 1.5: Representation of sol-gel and hydrothermal synthesis. Initial solution properties, precursor hydrolysis and condensation are crucial for both processes. In sol-gel synthesis, final products are achieved by drying or calcination. In the case of hydrothermal synthesis, nanoparticles are formed by precipitation from the solution at elevated temperature and pressure. 7
Figure 1.6: (a) At ambient conditions, aluminium forms a few nm thick Al_2O_3 coating on the surface that acts as a corrosion barrier. (b) Under hydrothermal conditions between 100–200 °C a few µm thick γ-AlO(OH) coating forms. (c) Aluminium can also be protected electrochemically by anodisation. 9
Figure 1.7: p-T diagram of the Al–H_2O system. Four main phases are present: gibbsite ($Al(OH)_3$), boehmite (γ-AlO(OH)), diaspore (α-AlO(OH)) and corundum (Al_2O_3) [35]. ..10
Figure 1.8: Zinc oxide wurzite hexagonal structure with marked growth directions. Fastest growth is in [0001] direction, followed by the growth of prismatic planes $[10\bar{1}0]$. Growth is minimal in $[000\bar{1}]$ direction. 12
Figure 1.9: Three examples of zinc oxide morphologies: (a) tetrapods, (b) stacked nanorods and (c) hedgehog-like structure. 13
Figure 1.10: The three main TiO_2 polymorphs: (a) metastable, tetragonal rutile, (b) tetragonal anatase and (c) orthorhombic brookite. 16
Figure 1.11: Structural formulas of two alkoxides used as Ti precursors: (a) titanium isopropoxide and (b) titanium butoxide. 17
Figure 1.12: (a) Schematic representation of primary processes upon UV irradiation of photocatalytic semiconductor material. Light with the energy greater than E_{bg} excites the electron to conduction band. (b) Band structure change upon contact with electrolyte [55], [56]. 19
Figure 1.13: Force equilibrium at the triple junction of solid, liquid and gas phase represents Young's equation. 21
Figure 1.14: Droplet-surface relations and contact angle; from superhydrophilic (close to zero degree) to superhydrophobic (above 150 degrees). 22
Figure 1.15: Different relations between the droplet and the surface: (a) ideal surface and Young's contact angle, (b) rough but homogeneous surface and Wenzel angle (θ_W) and (c) Cassie-Baxter hydrophobic state when various phases and materials are involved. 23

Figure 1.16: Extrand surface with ideal geometrical shapes. Asperities will cause a droplet into the Cassie-Baxter state for $\Lambda > \Lambda_C$. 24
Figure 1.17: Schematic representation of oxygen vacancies generation as a consequence of UV irradiation. Further reactions with dissociated water produce superhydrophilic surfaces [75]. 26
Figure 1.18: Ti facets have different terminal atom configuration. Facets with bridging oxygen atoms are more favorable for hydrophilic applications [75]. 27
Figure 1.19: Self-cleaning effect on lotus leaf. Appropriate roughness and waxy hydrophobic coating make the surface of the lotus leave superhydrophobic. 28
Figure 1.20: (a) direct observation of *Pseudomonas aeruginosa* by scanning electron microscopy and (b) optical microscopy micrograph of in-direct Gram staining by crystal violet. 31
Figure 3.1: Three-step process of hydrophobic coating attachment to the surface. After initial hydrolysis, silane undergoes polycondensation that bridges Si sites between each other with oxygen bridges as well as cross-linking Si sites to the surface. 37
Figure 3.2: Schematic of measuring setup equivalent: capacitor (C) and resistor (G) in parallel. 41
Figure 3.3: Spectral intensity of the two lights I used for photocatalytic degradation measurements: OSRAM ULTRA-VITALUX Ultraviolet high-pressure lamps light and LED UV 365 nm. 42
Figure 3.4: (a) Assembled reactor with the aluminium sample and (b) 3D model of the bottom halve. 43
Figure 3.5: Reactor system with peristaltic pump, reactor with UV LED array, UV/VIS spectrometer and small reservoir. 43
Figure 4.1: SE-SEM micrographs of (a) untreated aluminium surface and (b) aluminium sample after 24 h in dH_2O. Both samples still exhibit abrasions on the surface that are a consequence of mechanical deformation during rolling of the sheets. The formation of hydroxide particles can be observed in the inset of the treated sample. 45
Figure 4.2: XRD diffractogram of boehmite layers on substrates: (a) untreated aluminium sample, (b) hydrothermally treated aluminium substrate at 150 °C / 12 h without Ti precursor and (c) hydrothermally treated aluminium substrate at 200 °C / 12 h without Ti precursor. The appearance and increase of boehmite peaks at 14.49°, 28.21° and 49.3° indicates the presence and increase in the thickness of boehmite layer with the increase of synthesis temperature from 150 °C to 200 °C. 47
Figure 4.3: BE-SEM micrograph of cross-section aluminium substrate with boehmite coating, hydrothermally prepared at 200 °C / 12 h with TTIP precursor. (a) Aluminium substrate, (b) 1.75 µm thick boehmite layer and (c) epoxy resin. 47
Figure 4.4: SEM micrographs of (a) hydrothermally treated aluminium surface at 150 °C / 12h without Ti precursors. Sub-micron boehmite crystal clusters form nonhomogeneously over the surface and (b) aluminium sample treated in abs. ethanol at 150 °C / 12 h with TTIP. Formations are amorphous. 48
Figure 4.5: (a) SEM micrographs of solvothermally treated aluminium in isopropyl alcohol at 200 °C / 12h with TTIP. EDXS confirms the presence of titanium but no new crystallised phase was observed. (b) Aluminium sample, prepared in deionised water at 200 °C / 12h without Ti precursor. Blocky boehmite crystals are covering the whole surface. 49
Figure 4.6: (a) Boehmite crystals with planar defects on hydrothermally treated aluminium samples at 200 °C / 12h with TTIP and (b) prolonged synthesis to 48 hours at the same conditions. Planar defects are marked in the inset. 50

Figure 4.7: TEM image and EDXS spectra on (1) the area with defects and Ti present and (2) on the area without defects. Layered phase in the area with the defects could be a tivanite-like structure of (Al,Ti)-oxyhydroxyde.....51
Figure 4.8: EDXS elemental mapping of TiO_2 nanoparticle on boehmite layer.....51
Figure 4.9: SEM micrographs of (a) boehmite crystals with TiO_2 globular nanoparticles on hydrothermally treated aluminium substrate at 200 °C / 12 h with TTIP at pH 7 and (b) higher magnification close-up. Boehmite crystal with the defects is marked with an arrow. 52
Figure 4.10: Calculated X-ray penetration depth for low incident angles where $\alpha \sim \alpha_c$ (critical angle) for TiO_2. 53
Figure 4.11: Low-angle XRD diffractogram of hydrothermally treated aluminium substrate at 200 °C / 12 h with TTIP. Anatase and boehmite peaks are clearly seen due to lower penetration depth compared to conventional XRD. 54
Figure 4.12: Schematic presentation of aluminium substrate covered with 1.5–2 μm thick boehmite layer and nano-sized TiO_2 particles prepared at 200 °C / 12 h with TTIP at pH 7.....54
Figure 4.13: SEM micrographs of (a) hydrothermally treated aluminium substrate at 200 °C / 12 h with TBT at pH 7 and (b) prolonged synthesis (62h) at 200 °C with TTIP at pH 7.....55
Figure 4.14: SEM micrographs of (a) calcined substrates at 400 °C for 3 h and (b) 600 °C for 6 hours. Cracks in boehmite/TiO_2 coating are due to the difference in linear thermal expansion coefficients.....56
Figure 4.15: Corrosion of aluminium substrate due to the presence of HF.....56
Figure 4.16: AFM imaging of (a) untreated and (b) hydrothermally treated aluminium substrate at 200 °C / 12 h. Fourfold increase in roughness is observed between the samples due to the presence of boehmite crystals. Waviness from manufacturing is retained.....57
Figure 4.17: Roughness comparison between hydrothermally treated aluminium substrates. An increase in R_a and R_q is observed on the surface with boehmite crystals. Additional layer of TiO_2 smooths the surface as it fills the pits and holes between boehmite crystals. 58
Figure 4.18: Contact angle measurements on (a) unirradiate aluminium/boehmite/TiO_2 surface and (b) UV irradiated TiO_2 coated substrate. A drop from 80° to below 15° is observed.....58
Figure 4.19: Caffeine degradation curves for Degussa P 25 (anatase/rutile) and HT 200 °C 12h TTIP pH7 sample: with and without stirring as well as extracted TiO_2 powder from the autoclave. 59
Figure 4.20: SEM micrographs of (a) hydrothermally treated aluminium foil at 120 °C / 12h at low magnification and (b) small clusters of pseudoboehmite particles. 60
Figure 4.21: FIB cross-section on boehmite-coated aluminium foil, hydrothermally treated at 200 °C / 12 h.....61
Figure 4.22: Temperature dependences of the real part of the complex dielectric constant, ε', the dielectric losses, $\tan\delta$, and the real part of the complex electrical conductivity, σ', of the boehmite layer on the aluminium foil.....62
Figure 4.23: The real part of the complex dielectric constant vs. the temperature and frequency, revealing that the boehmite layer on the aluminium foil exhibits stable ε' values over broad temperature and frequency ranges. 63
Figure 4.24: XRD diffractogram of (a) metallic untreated zinc substrate, (b) hydrothermally treated zinc at 120 °C / 12h with ZnO hedgehog-like morphology and (c) hydrothermally treated sample at 120 °C / 6 h with the addition of DAP structural agent. 65

Figure 4.25: (a) Hydrothermally grown ZnO in water at 120 °C / 12h forms spikey hedgehog-like structures that homogeneously cover the substrate. (b) Higher magnification micrograph shows wurtzite needles forming structures that greatly increase the specific surface on the sample. 66
Figure 4.26: SEM micrographs of hydrothermally treated zinc sample at 120 °C / 2 h in alkaline medium (pH 10) with ZnO leaf-like hexagonal morphology. 66
Figure 4.27: SEM micrographs of ZnO submicron rods on zinc substrate hydrothermally treated in water with the addition of the Zn precursor..... 67
Figure 4.28: The amount of Zn precursor is crucial for homogenous coverage of ZnO in solvothermal treatment. (a) 0.6 g of zinc nitrate hexahydrate in 50 ml ethanol initial solution was not enough to achieve complete coverage at 120 °C / 12 h (b) while 1.2 g sufficed. 67
Figure 4.29: Prolonged solvothermal synthesis causes the abnormal growth over ordered hexagonal ZnO coating observed on samples treated at 120 °C / 48 h. (a) The sample in ethanol at 120 °C / 48 h retains the initial ZnO coating but forms 3–4 µm wide pillar-like structures on top. (b) The morphology of the coating in isopropyl alcohol at the same conditions completely changes and forms platelet-like morphology. 68
Figure 4.30: SEM micrograph and high-magnification insert of hydrothermally treated zinc substrate at 120 °C / 6 h with zinc nitrate hexahydrate and DAP structural agent.69
Figure 4.31: Water droplets on the zinc surfaces that underwent different treatment. (a) Untreated zinc is hydrophobic and has a contact angle of 110°. (b) Hydrothermally treated zinc with ZnO coating is hydrophilic with contact angle 40° while (c) the same surface that was treated with FAS displays superhydrophobic properties with a contact angle above 150°. 70
Figure 4.32: Roughness (R_q) and contact angle characteristics of AISI 304 substrates that underwent different procedures. 71
Figure 4.33: Time dependence of the contact angle. Plasma-treated sample achieves relaxation in 3 hours. 72
Figure 4.34: Relative adhesion rate for different bacteria on metal surfaces determined by optical density at 584 nm for different bacteria on metal disks. 73
Figure 4.35: Adhesion of *E. coli* ATCC 35218 on AISI 304 substrates. No bacteria were observed on the superhydrophobic zinc substrate. 75
Figure 4.36: SEM micrographs with adhered bacteria for (a) brushed and (b) electropolished AISI 304 samples. The microbes preferentially adhere in pits, cavities and other non-regularities and grow laterally in one layer on surfaces with a low roughness (a). On the surfaces with a higher roughness, (b) the microbes are concentrated in pores and scratches and grow in multilayers. 76

List of Tables

Table 4.1: Parameters for hydro- and solvothermal treatment of aluminium in deionised water, ethanol and isopropyl alcohol. 46
Table 4.2: Size, morphology and crystallinity of particles forming the coatings as a function of hydrothermal conditions. 60
Table 4.3: Parameters for hydro- and solvothermal treatment of zinc in deionised water, ethanol and isopropyl alcohol. 64
Table 4.4: Average bacterial cell hydrophobicity determined with xylene. 72

Abbreviations

ABF	. . . annular bright-field
AFM	. . . atomic force microscopy
BE	. . . backscattered electrons
BF	. . . bright-field
CFU	. . . colony forming unit
CV	. . . crystal violet
CVD	. . . chemical vapour deposition
DAH	. . . 1,6-diaminohexane
DAP	. . . 1,3-diaminopropane
DF	. . . dark field
DLF	. . . diamond-lapping film
EELS	. . . electron energy loss spectroscopy
EFTEM	. . . energy filtered transmission electron microscopy
EDXS	. . . energy-dispersive X-ray spectroscopy
EtOH	. . . ethanol
FAS	. . . fluoroalkyl oligosiloxane
FEG	. . . field-emission gun
FIB	. . . focused ion beam
FT-IR	. . . Fourier transform infrared spectroscopy
HRTEM	. . . high-resolution transmission electron microscopy
HT	. . . hydrothermal treatment
ICSD	. . . inorganic crystal structure database
IPA	. . . isopropyl alcohol
OD	. . . optical density
p-T	. . . pressure-temperature
PBS	. . . phosphate buffer saline
PIPS	. . . precision ion polishing system
PV	. . . photo-voltaic
PVD	. . . physical vapour deposition
QY	. . . quantum yield
SAED	. . . selected-area electron diffraction
SDD	. . . silicon drift detector
SE	. . . secondary electrons
SEM	. . . scanning electron microscopy
ST	. . . solvothermal treatment
STEM	. . . scanning-transmission electron microscopy
STM	. . . scanning tunnelling microscopy
TBT	. . . titanium(IV) butoxide
TEM	. . . transmission electron microscopy
TMAH	. . . tetramethylammonium hydroxide
TSB	. . . tryptic soy broth

TTIP	...	titanium(IV) isopropoxide
UV/Vis	...	ultraviolet–visible spectroscopy
XRD	...	X-ray powder diffraction

Symbols

δ_p ... penetration depth
h^+ ... positive hole
e^- ... electron
E_{bg} ... band gap energy
γ_{ab} ... surface tension between phases a and b
Λ ... contact line density
θ^* ... apparent contact angle
μ ... absorption coefficient
α ... incident angle
ε^* ... complex dielectric constant
ε_0 ... permittivity of free space
$tan\delta$ ... dielectric losses
σ' ... complex electrical conductivity
A ... absorption

Chapter 1

Introduction

1.1 Overview

The use of nanoparticles for functionalised coatings covers a wide range of substrates and applications. Photocatalytic and self-cleaning properties have been utilised for air purification in ventilation systems, as self-cleaning roof and floor tiles, for antibacterial and sterilisation applications in medicine, food processing, and others [1], [2]. By the introduction of layered structure of different oxides and other compounds that influence certain surface characteristics, one can achieve wide arrange of novel applications that substrate would not attain without the use of the nanotechnology. Superhydrophobic and superhydrophilic surfaces are opening new areas for applications for passive self-cleaning and bacteriostatic surfaces.

Photocatalytic materials tackle another great issue that is the availability of the freshwater. Access to clean freshwater is becoming one of the most important challenges for many communities around the world. Drinking water is essential for life on Earth and with rapid industrial growth and society's passive attitude towards the problem it has become a major issue that more and more people will have to face on a daily basis. A large majority, over 97%, of all the world's water supply is seawater and therefore unusable for sustaining life. With more than three quarters of the remaining fresh water being trapped in glaciers or ice caps, the remaining usable fresh water falls below 1% of all water supplies [3]. This small fraction of water is further threatened by contamination and disposal of chemicals from agriculture, industry, residues from medicines and common households. While world population growth rate is slowly decreasing, the total world population is expected to keep growing, where estimates have put the total population at 9.6 billion by mid-2050. Population growth is fastest in the developing countries where access to potable water is already a problem. Development of simple and economically viable water treatment methods is therefore of great importance.

Conventional water treatment combines both physical and biological processes, namely sedimentation, flocculation, aeration, chlorination, and others [4]. Advanced oxidation processes provide an additional process in which organic compounds can achieve partial degradation or even complete mineralisation to CO_2 and water by means of oxidation through reactions with hydroxyl radicals. Photocatalytic systems, based on semiconductor oxides, have proven to be a reliable and cost-effective option. The best photocatalytic effect is achieved when the catalyst is in a form of nanoparticles, maximizing the surface to volume ration and therefore increasing degradation of organics since photocatalysis is a surface reaction. Separation of treated substance and photocatalytic nanoparticles is a persistent problem when considering batch-type reactors as well as residual nanoparticle waste and its accidental removal to the environment.

Extensive research has been conducted in recent years in order to tackle this issue by catalyst immobilisation on different substrates, addition of photocatalytic nanoparticles to micro-sized particles for ease of filtration and so on [5].

1.2 Nanomaterials

The field of nanotechnology and thereby synthesis of nanomaterials has seen, especially in recent years, a rapid development trend. Since its conceptual inception in 1959 by physicist Richard Feynman's "There's Plenty of Room at the Bottom" lecture at California Institute of Technology and gradual development through the years, nanotechnology and nanomaterials became a part of everyday life [6]. Milestones, such as the development of the scanning tunnelling microscope (STM) in 1981, atomic force microscope (AFM) in 1982 and advances in electron microscopy, provided tools to observe and manipulate objects at the nanoscale.

Nanomaterials are, by definition, materials of which a single unit measures under 100 nm in at least one dimension. This reduction in size greatly alters the surface to volume ratio, increasing the amount of surface atoms compared to the bulk. As many chemical reactions and physical properties are strongly surface-dependent, such materials exhibit modified electrical, mechanical, chemical or optical properties. In the field of nanotechnology scientists seek to develop novel applications, based on nanomaterials and nanostructures, with improved properties such as superior toughness, hardness, hydrophobicity and hydrophilicity, photoluminescence, materials for chemical sensing and (photo)catalytic applications, and others.

Two principal approaches, used in nanotechnology, are the so-called "bottom-up" and "top-down" approach [7], [8]. By "top-down" path, materials are constructed from bulk (or larger entities" with specific control on atomic level. Typical methods for such approach are photolithography, milling and etching. The "bottom-up" approach tackles the problem from a different direction by fabrication or manipulation of components which assemble themselves chemically or physically atom-by-atom, molecule-by-molecule or cluster-by-cluster. The "bottom-up" approach is essential for the preparation of highly crystallised nanomaterials and nanostructures and has many advantages over the "top-down" path, such as the formation of more chemically homogenous materials, with fewer defects and better short and long-range ordering (Figure 1.1) [9].

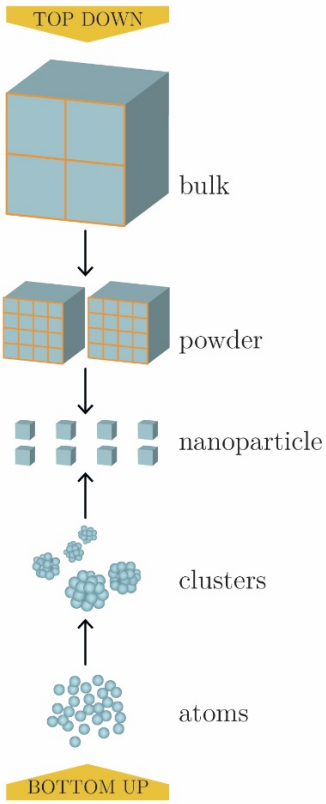


Figure 1.1: Schematic representation of two main approaches in nanotechnology: top-down and bottom-up.

Due to the exceptional properties of nanoparticles, their toxicity and general impact on the environment and human health have been studied extensively in recent years [10]–[12]. Micron size (and larger) TiO_2 is considered to be an inert and safe material and has been used for decades. Increased usage of nano TiO_2, either intentional or unintentional, however, calls for more thorough toxicological studies. Oxidative stress is the main result of adverse effects of nano-sized TiO_2, resulting in cell damage and inflammation. Data shows no significant inflammation caused by transdermal TiO_2 intake but long-term effects and photo-induced TiO_2 effects could have potential adverse effects [13], [14]. Dermal exposure is, however, not the only route of entry. TiO_2 as food additive E171 is permitted in food and pharmaceutical products as a whitening agent and currently there is no reliable data on its distribution, activity and toxicity by oral exposure. It has been shown that most commercially available TiO_2 as a whitening agent have, in fact, nanoparticles present alongside larger (main) particles [15], [16]. Many existing slurry-type photocatalytic reactors use TiO_2 nanoparticles in suspension where separation and reuse of catalyst from the final product is difficult to achieve. Immobilized TiO_2 in a form of hard coating is a promising solution and opens the possibility for manufacturing of reactors with reusable photocatalysis with minimal erosion of nanoparticles into the environment.

1.2.1 Semiconducting nanomaterials

Semiconductors are a family of materials of high technological relevance. Advances in electronics and information revolution, starting with the first computers in the 50', rely mainly on the archetypical semiconductor material, silicon. This is the basic constituent of current transistors and diodes in any kind of electronic devices from computers to cell phones. In the field of energy production, the photovoltaic (PV) cells take the advantage of the interaction of light with semiconductors for electrical power generation, similarly as photocatalysts do. Semiconducting materials are nominally small band gap insulators which, among other things, make them susceptible to photo irradiating effects in or near the visible spectre. At 0 K, a semiconductor is primarily an insulator. However, at room temperature the valence band is slightly thermally depopulated and the conduction band slightly populated due to a small energy gap between two bands (~ few eV). This is directly related to the particular electronic structure of those solids, their composition, crystal structure and dopants. Figure 1.2 shows extrinsic semiconductor candidates. Valence band gap of around 3 eV and below could easily be overcome with light excitation from UV and near-UV spectra, promoting photo-inducted effects on the surface.

Most common examples of semiconducting materials and their band gap are listed in Figure 1.2. Titanium dioxide, TiO_2, is one of the most studied photocatalysts that can be used for production of self-cleaning surfaces, water and air cleaning and other applications. Strictly speaking it is an n-type semiconductor as a bulk material due to oxygen vacancies in the TiO_2 lattice, this definition is blurred and not so obvious for nanostructured TiO_2. Studies have been conducted to determine the influence of primary particle size, dopants and other factors, influencing the band gap and n- or p-type behaviour of a native system [1].

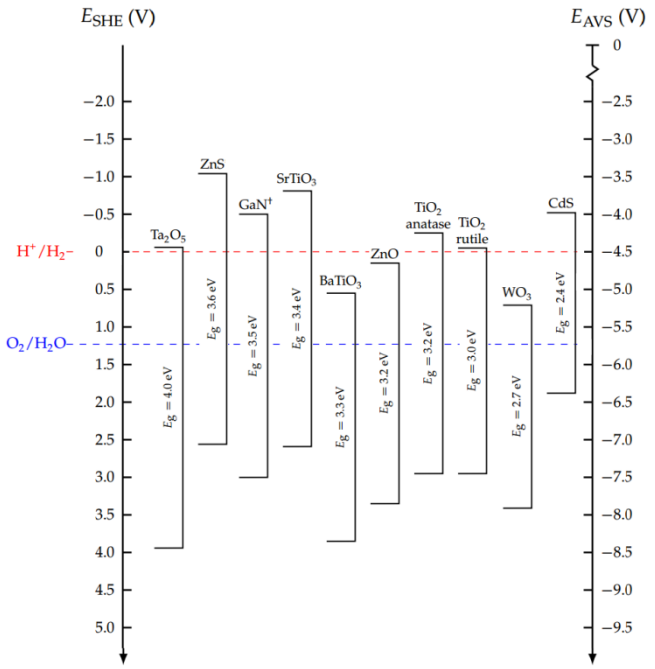


Figure 1.2: Absolute conduction band and valence band energy levels of potential semiconductors versus the standard electrochemical potential scale and the vacuum energy scale [17].

1.2.1.1 Synthesis methods

Synthesis techniques for producing nanostructured materials can be separated into two categories by the general approach taken, namely "bottom-up" and "top-down" approach. Among top-down nanofabrication techniques such as high-energy ball milling, grinding, pyrolysis, focused ion-beam and chemical etching, different forms of lithography are most widely used. Thus, nanostructured features are achieved by selective etching of bulk materials down to the micro- and nano-level.

Photolithography is a simple method utilizing selective etching in combination with photo resistive film. Nanostructures significantly smaller than 100 nm are difficult to produce by this approach due to diffraction effects. This can be overcome with electron-beam or X-ray lithography where the pattern is written in a polymer film with electrons and X-rays of smaller wavelength, improving the resolution greatly and reducing the blurring of features. Though the operation costs of those methods are low once the pattern masks are prepared (in the case of photolithography), photolithographic tools are very costly, making the whole process expensive. Although it offers unprecedented ability of manipulating the structure of bulk down to the nano-level that cannot be achieved by other methods, it remains a complex, expensive and most importantly, slow method compared to other synthesis techniques [18].

Bottom-up methods work in the opposite direction, starting with atoms or molecules and building up to nanoparticles and nanostructures. This is achieved by employing techniques related to crystal and epitaxial growth, precipitation from solutions and formation of nanoparticles from colloidal dispersions, the latter provides great control over formation mechanisms which directly influence the promotion of desired properties. Bottom-up methods are also generally less expensive than top-down methods. The approach has been frequently used with other top-down methods to form complex hierarchical structures and different composites. Some of such methods are atomic layer deposition, sol-gel, hydro- and solvothermal synthesis, STM and AFM single particle manipulation, molecular beam epitaxy and chemical vapour deposition and all are usually considered bottom-up techniques.

1.2.1.2 Hydro- and solvothermal synthesis

One of the methods capable of producing finely shaped and crystalized nanomaterials is hydrothermal synthesis. It is a *bottom-up* approach especially useful when seeking to create very small nanoparticles of uniform size, based on simple oxides. The nature of the process also allows for higher pressures and temperatures which are normally used in wet chemistry. This allows reactants that are otherwise difficult to dissolve to go into solution as complexes [19], [20].

Hydro- or solvothermal synthesis is a method of crystallising substances under high pressure and at elevated temperature where water (in the case of hydro) or some other substance is used as solvent in the case of solvothermal treatment. The crystal growth is performed in an autoclave; a thick-walled steel pressure vessel that is hermetically sealed and allows a solvent to be kept at high temperature and high pressure for a long time. Corrosion and solvent contamination are problems as those processes are even more prominent in conditions at which the synthesis occurs. Autoclave walls are therefore protected with inert material in respect to the solvent. For applications up to 200 °C Teflon is used due to its inert properties, wetting angle and ease of manufacturing. Apart from those used in medicine for sterilising, there are few different types of autoclaves, specifically designed for synthesis of materials. Figure 1.3 a shows general-purpose

autoclave which is commonly used in laboratory due to its size, ease of operation and ability to exchange the Teflon inner capsule.



Figure 1.3: General-purpose autoclave with Teflon inner capsule as used in my experimental work.

Pressure inside the autoclave can be directly measured using a pressure gauge or indirectly estimated from filling of an autoclave; the same pressure will be achieved at a lower temperature with high filling as shown in Figure 1.4. In recent years, stirring reactors have become widely used as they provide means to continuously stir the solvent at different rates, lead a different atmosphere in the reactor and sample while the reactor is still pressurized [21]. This allows a better understanding of reaction kinetics, determination of intermediate phases and optimisation of the process. There are several other types of reactors: microwave reactor, electro- and sonochemical reactor and flow reactor just to name a few.

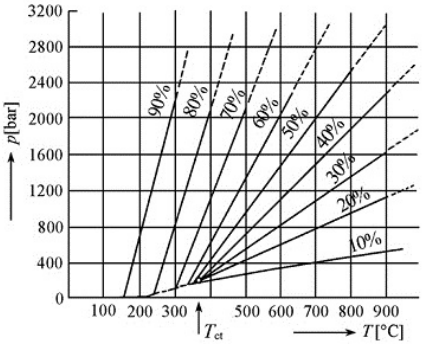


Figure 1.4: Correlation of pressure and temperature for pure water, with the degree of filling of the sealed autoclave as a parameter. Pressures up to 2000 bar are achieved with filling factors between 50 and 80% [22].

Chemist Robert Bunsen was the first one to synthesize barium and strontium carbonate in glass apparatus at 200 °C and under pressure of 100 bars [23]. At first, only crystals of microscopic sizes were produced (Schafhäult and de Sénarmont, circa 1850), while macroscopic crystals were synthesized by Spezzia in 1905 [24]. War effort in the first half of the 20th century forced a rapid development of industrial scale hydrothermal

manufacturing, primarily for quartz. This method is nowadays used to prepare new materials with specific properties, unique morphology and for studying of multicomponent systems at high temperatures and pressures.

Hydrothermal processing can be defined as any heterogeneous reaction in the presence of aqueous solvents or mineralizers under high pressure and temperature, either to dissolve or recrystallise materials that are relatively insoluble under normal conditions. The word 'hydros' comes from Greek for water, but the term hydrothermal covers reactions in non-aqueous solvents as well. There are several other terms under the term solvothermal, specifying reactions in different solvents, like glycothermal, alcothermal, and so on. Medium is important as it transfers pressure, it is a solvent for nutrient and it accelerates reaction because of higher diffusion and solubility.

Preparation of proper nutrient solution is where initial chemistry of desired compound can be influenced the most. Many practices are therefore similar to sol preparation in sol-gel processing [25]. Sol-gel is a synthesis method for producing solid materials, usually in the form of films, fibres or powders, from small molecules. The process involves the preparation of colloidal solution (sol) by conversion of monomers. This solution acts as the precursor for gel in a state of continuous network after the stabilising component is removed through the polymerisation of the particles. Sols are usually used to coat substrates by spraying, spin-coating or dip-coating. Same suspension could as well be used as a precursor in hydrothermal synthesis. Schematic representation of sol-gel processing steps and hydrothermal synthesis is presented in Figure 1.5.

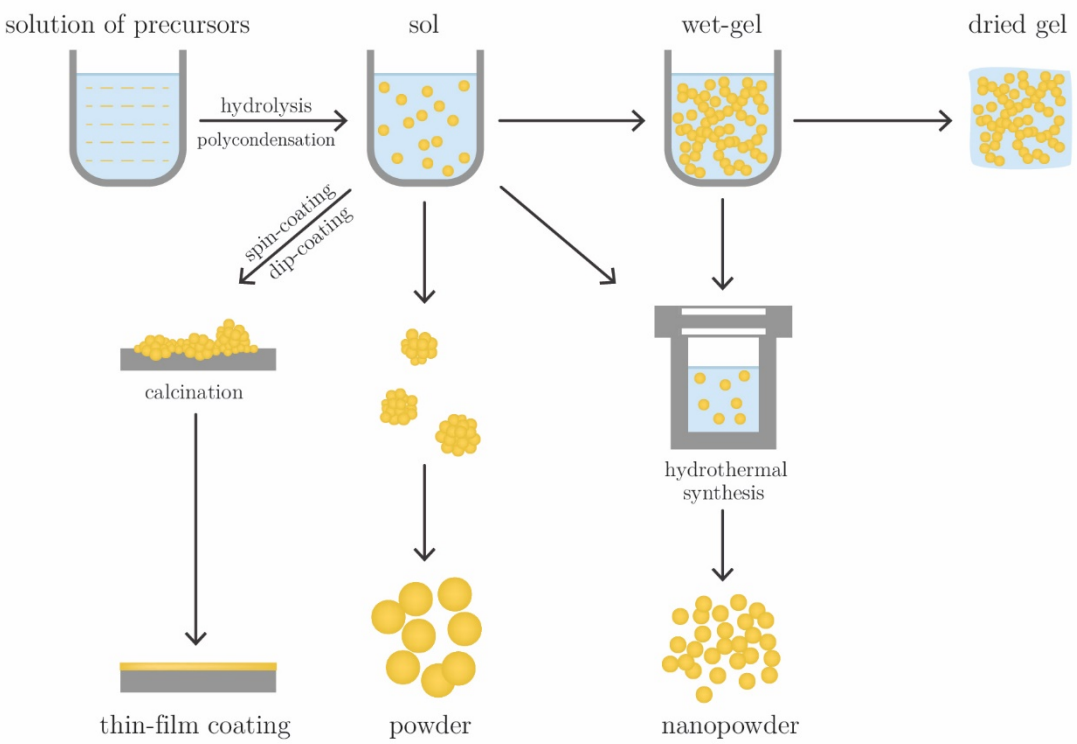


Figure 1.5: Representation of sol-gel and hydrothermal synthesis. Initial solution properties, precursor hydrolysis and condensation are crucial for both processes. In sol-gel synthesis, final products are achieved by drying or calcination. In the case of hydrothermal synthesis, nanoparticles are formed by precipitation from the solution at elevated temperature and pressure.

1.2.2 Immobilisation of nanoparticles

Due to the intrinsic enhanced activity of nanoparticles in the form of powders and suspensions it is crucial that such materials are not released freely into the environment as the effects could prove toxic and harmful for living organisms. Many existing slurry-type reactors use catalytic nanoparticles in suspension where separation and reuse of catalyst from the final product is difficult to achieve. The removal itself is not too problematic since the addition of coagulants and/or flocculants can lead to rapid separation of active nanoparticles and treated substance but once the catalyst is agglomerated it is difficult to recycle it and to achieve the same size distribution and surface properties as the initial material. Immobilisation of active agent on a substrate is therefore of great technological and environmental importance. Nanoparticles can be prepared on the surface of micron-sized structures or membranes [26], retaining most of their size-dependent activity while allowing for a much simpler filtration and reintroduction back into reaction. Another possibility are nanoparticles, especially the metal oxide ones in a form of hard coatings on the substrates, either mesh-like metallic membranes or solid metal sheets. This opens the possibility for the manufacturing of reactors with reusable active nanoparticles with minimal erosion into the environment [5], [27].

1.2.2.1 Methods of immobilisation

Immobilisation of nanoparticles on the surface of larger objects has been heavily studied in the past [28], [29]. While it generally lowers their activity it offers numerous possibilities for applications in nanotechnology as it improves the ease of handling.

Immobilisation of nanoparticles on the surface can be achieved via several different methods. Very homogenous coating can be obtained with dip-coating and spin-coating techniques, both mainly in conjunction with the sol-gel method. While those methods produce coatings with great activity, the adhesion between coating and the substrate is weak and prone to erosion in high-flow applications. Magnetron sputtering and plasma deposition methods offer better adhesion but are expensive and do not offer comparable homogeneity and degree of crystallisation of nanoparticles. Hydrothermal synthesis is a simple and cost-efficient method of preparing nanoparticles of simple metal oxides on substrates of any desired shape.

As with any synthesis method, it comes with its share of drawbacks. Nanoparticle precursor, solvent and the substrate are all submerged in the autoclave so secondary (often undesired) reactions occur due to the chemistry of the substrate and its reaction with the precursors or characteristics of the medium, its acidity or inability to dissolve the precursor at ambient conditions.

1.3 Aluminium

Aluminium is lightweight, ductile, soft metal. It is naturally passivated and therefore it is considered a very corrosion-resistant metal. It is the third most abundant element in nature and the most abundant metal. Elemental aluminium is scarce in nature due to its activity and tendency to passivate, but there are more than 270 naturally occurring minerals containing aluminium.

Due to its density, good mechanical properties and corrosion resistance, aluminium has found its place in a wide array of applications. It is the most broadly used non-ferrous metal and it is often used as construction material for special applications in aeronautics, transportation and other areas of use where weight of the final product is a

key factor [30]. In addition, aluminium is widely used in electronics, packing, food and other industries. It is also a deoxidising agent in steelmaking.

Aluminium is almost always alloyed unless used for application where high electrical conductivity is required with no consideration for mechanical properties. Alloying aluminium increases its mechanical properties, especially when tempered and hardened due to precipitation hardening. Most common alloying elements are silicon, magnesium, copper, iron, manganese and zinc.

1.3.1 Passivation of aluminium

Pure unalloyed aluminium rapidly forms 2–3 nm thick surface layer of amorphous aluminium oxide when exposed to oxygen in the atmosphere. This creates a physical barrier that prevents further corrosion or oxidation of the surface. Figure 1.6 shows different ways of achieving passivation in the case of aluminium.

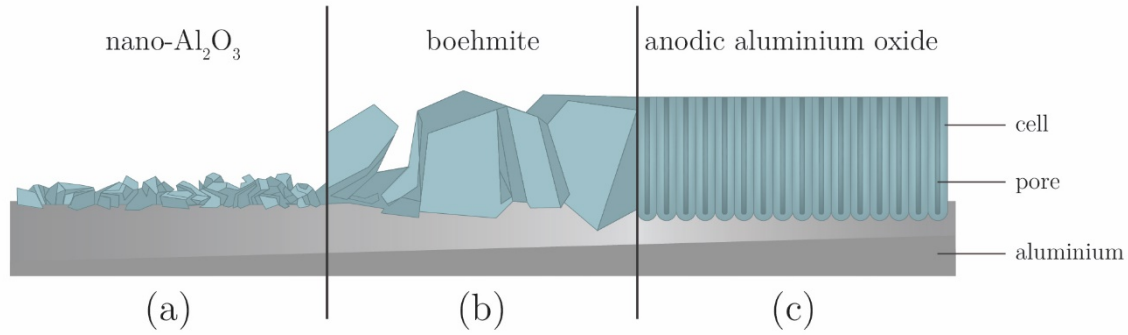


Figure 1.6: (a) At ambient conditions, aluminium forms a few nm thick Al_2O_3 coating on the surface that acts as a corrosion barrier. (b) Under hydrothermal conditions between 100–200 °C a few µm thick γ-AlO(OH) coating forms. (c) Aluminium can also be protected electrochemically by anodisation.

Aluminium alloys, which are technologically more suitable than pure aluminium, are more prone to corrosion so other passivation methods are used. Typically, aluminium alloys are passivated by three methods [31], [32]:

- Alclading, which is metallurgical bonding of pure aluminium sheet to high-strength aluminium alloy core material.
- Chromate and phosphate conversion coating, which are processes improving corrosion resistance, retainment of electrical conductivity and as a decorative finish of aluminium and various other metal. The process involves application of phosphoric acid with phosphate slats or chromic acid for hexavalent chromium by spraying or immersion which is very toxic.
- Anodisation, an electrolytic passivation process for introduction of thicker oxide protective coating on the surface, increasing corrosion resistance, allowing dyeing (colouring by the addition of pigment in the eloxation process) and improvement of lubrication and adhesion.

Hydrothermal treatment is not widely used as the surface treatment method of aluminium but it is important to note the implications of introducing an active substrate such as aluminium into the reaction vessel. The surface undergoes morphological and

chemical changes at temperatures as low as 50 °C in the autoclave when in water [33], [34]. The surface of aluminium kitchenware, for example, will also oxidise significantly with time and wear since high temperature alone will be enough for enhanced oxidation of surface layer.

1.3.2 Aluminium under hydrothermal conditions

While there are no direct studies on hydrothermal treatment of metallic aluminium that would take into account diffusion processes of aluminium into water at the surface, the Al – H_2O p-T diagram is well studied [35]–[37]. It consists of aluminium oxides and hydroxides with various degrees of crystallinity, depending on conditions:

- Gibbsite ($Al(OH)_3$), with polymorphs Bayerite, Doyleite, and Nordstrandite
- Boehmite (γ-AlO(OH))
- Diaspore (α-AlO(OH))
- Corundum (Al_2O_3)

Figure 1.7 shows the temperature and pressure dependencies in the Al–H_2O p-T diagram. It is worth noting that filling of the autoclave and therefore pressure has some impact on phase composition but the main influencing factor is temperature, especially at higher pressures.

My work has been carried out in general-purpose autoclaves at temperatures limited to 200 °C due to the Teflon lining, which makes gibbsite the preferred phase at temperatures up to 100 °C (depending on the pressure) and boehmite at temperatures above that [38].

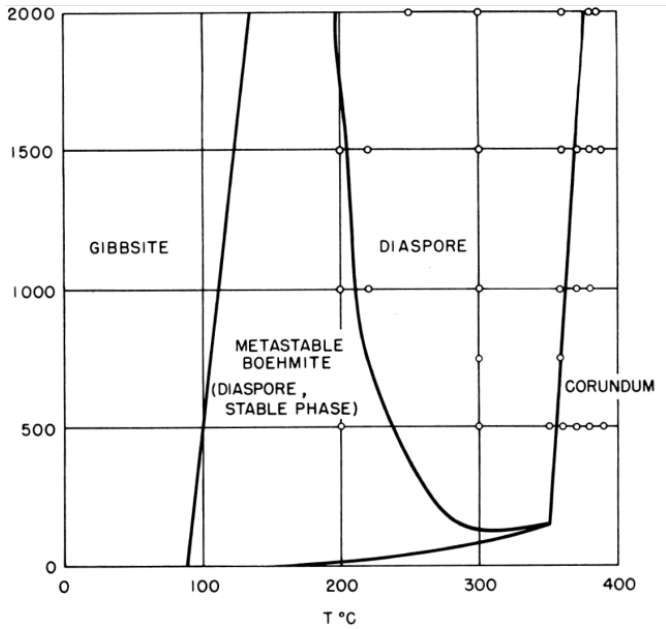


Figure 1.7: p-T diagram of the Al–H_2O system. Four main phases are present: gibbsite ($Al(OH)_3$), boehmite (γ-AlO(OH)), diaspore (α-AlO(OH)) and corundum (Al_2O_3) [35].

1.4 Zinc

Zinc is a bluish-white, hard and brittle metal with high corrosion resistance due to its electrochemical characteristics. It is the 24th most abundant element in Earth's crust. It becomes malleable between 100 and 150 °C which allowed for very early adaptations on pure zinc (6th century BC) and zinc brass alloys as early as third millennium BC in the areas of Middle East and eastern parts of Indian peninsula [39].

It is less dense than iron and has a hexagonal close-packed lattice. The chemistry of zinc is dominated by the +2 oxidation state.

The majority of zinc is used for galvanisation of other metals, such as iron and steel, to increase corrosion resistance. It is applied electrochemically or as molten zinc by hot-dip galvanizing or spraying. Zinc is more reactive than iron, steel or aluminium so oxidation will preferentially occur there. In principle, it acts as a sacrificial anode. A protective surface layer of oxide and carbonate ($Zn_5(OH)_6(CO_3)_2$) forms as the zinc corrodes. This protection lasts even after the zinc layer is scratched but degrades with time as the zinc corrodes away [40].

Zinc is also used for alloying, including brass, nickel silver and aluminium solder.

1.4.1 Zinc oxide

Zinc forms binary compounds with most of the metalloids and all the non-metals, bare the noble gases. Zincite (ZnO) is the most widely used compound of zinc with a wide variety of applications. It is nearly insoluble in natural aqueous solutions but it displays amphoteric properties, dissolving in acids to give the aqueous Zn^{2+} ions and in alkali to give the zincate ion, $[Zn(OH)_4]^{2-}$.

Zinc oxide is a white inorganic compound that mainly crystallises in hexagonal wurtzite polymorph (Figure 1.8). Wurtzite structure is stable at ambient conditions and is thus more common. Both zinc and oxygen positions are tetrahedral coordinated. ZnO is an n-type semiconductor of the II-VI group with a wide band gap, high electron mobility, good transparency and strong luminescence at room temperature. It is widely used in the rubber industry for vulcanisation along with the stearic acid. It protects the final product from fungi and UV light. It is also used in the production of plastics, ceramics, as pigment in paints and adhesives. Due to its semiconductor nature, ZnO is used in liquid crystal displays, in electronics as thin-film transistors, varistors and LEDs [41].

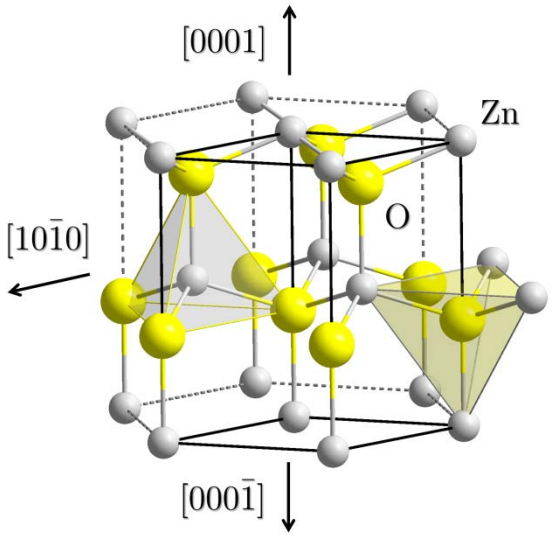


Figure 1.8: Zinc oxide wurzite hexagonal structure with marked growth directions. Fastest growth is in [0001] direction, followed by the growth of prismatic planes [10$\bar{1}$0]. Growth is minimal in [000$\bar{1}$] direction.

Due to the lack of inversion symmetry, both ZnO structures are piezoelectric while wurtzite polymorph is also pyroelectric. Wurtzite crystal exhibits partial polar characteristics with lattice parameters a = 0.3296 and c = 0.52065 nm in a hexagonal structure. Polar axes are always the basal planes (0001). On one end the basal plane terminates with partially positive Zn lattice sites while the other terminates in partially negative oxygen lattice sites. The oppositely charged ions at terminal surfaces result in a normal dipole moment and spontaneous polarisation along the c-axis as well as a variance in surface energy. To maintain a stable structure, the polar surfaces are generally faceted or exhibit massive surface reconstructions, but ZnO ±(0001) surfaces are exceptions: they are atomically flat, stable and exhibit no reconstruction. ZnO has a relatively large direct band gap of 3.3 eV at room temperature. Advantages associated with a large band gap include higher breakdown voltages in varistors, ability to sustain large electric fields and lower electronic noise.

1.4.2 Hydrothermal treatment and ZnO nanostructures

Zincite crystals can be grown by different methods [20]:

- from gas phase, normally on a pre-seeded substrate to produce ZnO needles
- from high-temperature solution using PbF_2 to produce plate-like crystals
- and hydrothermally to produce a great variety of 2D and 3D structures utilizing different zinc precursors, solvents and most importantly, structuring agents for preferential growth of the desired facet or inhibition of others

The first two synthesis methods often yield technologically unsatisfactory results due to imperfections in the crystals and the unsuitable habits. Hydrothermal synthesis is the most promising approach for the production of zinc oxide crystals of high crystallinity for many applications. In respect to this, understanding and controlling of crystal

morphology is of fundamental importance as incorrectly defined crystals may have an impact on the quality of the desired characteristics.

ZnO nanostructures attracted much attention lately due to their exceptional properties compared to the bulk. A variety of morphologies have been hydrothermally prepared such as nanocrystals [42], nanowires [43], nanorods [44], tetrapods [45], nanobelts [46], flower-like structures [47], nanosheets [48] and nanorings (Figure 1.9) [46]. The Zn source, solvent, pH, temperature, pressure and the additives, such as Au, all control the size and shape of the particles [48], [49]. The final morphology depends on growth conditions of the fastest growing direction. Unmodified ZnO grows fastest in [0001] direction, followed by $[10\bar{1}0]$ and slowest in $[000\bar{1}]$ direction. Crystal kinetics differs between crystal planes, resulting in different three-dimensional objects, depending on the conditions of the synthesis.

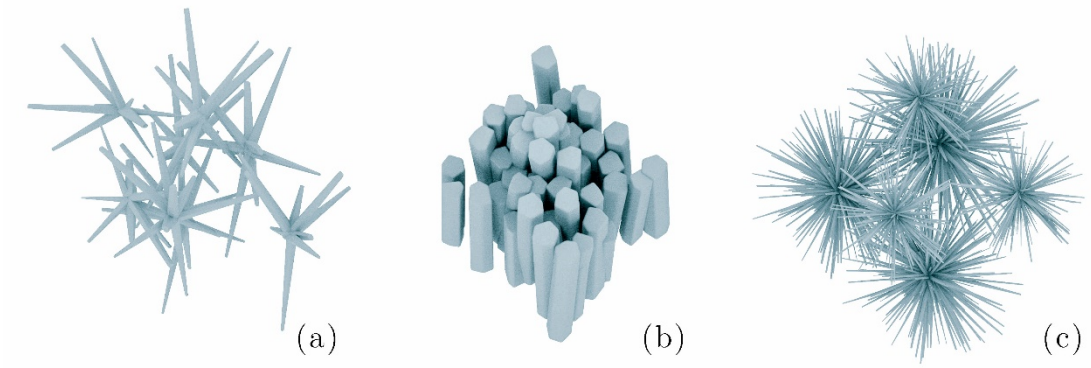


Figure 1.9: Three examples of zinc oxide morphologies: (a) tetrapods, (b) stacked nanorods and (c) hedgehog-like structure.

1.5 Stainless steel

Stainless steels are a family of corrosion resistant steel alloys with high mass content of chromium (10.5–26%). Chromium forms a passivation layer of chromium(III) oxide (Cr_2O_3) on the steel surface when exposed to oxygen that protects the bulk from corrosion. Different steel grades are used for different applications and can be categorised by the metallurgical phases present in their microstructure:

- Ferritic
- Martensitic
- Austenitic
- Duplex Steels (mix of ferrite and austenite)

Austenitic stainless steels are most widely used due to superior corrosion properties (no yield point, formability and deformation response tailored by chemical composition). Martensitic stainless steels can be heat treated while ferritic strainless steels essentially have no nickel content (which is always present in austenitic ones).

Because of good mechanical properties and low price, stainless steel is widely used in construction, transportation industry, medicine and for laboratory equipment, to name a

few. Due to its wide use in everyday life it is important to understand the surface conditions that promote or inhibit bacterial adhesion.

1.6 Functionalised Coatings on Metals

Most of the manufactured final products nowadays are covered with a coating, be it simply for decoration, an additional functional layer, or both. Lacquers and paints are coatings that have a dual function of protecting the substrate and being decorative. Both are applied as a final step in material production. Other materials, such as coloured magnetic plastic, have a pigment or functional material mixed in the material itself. Metals that are suitable for anodisation, aluminium for example, can also be dyed while being treated by anodisation techniques to form a corrosion resistance coating.

Pure functional coatings range from improvements in corrosion resistance, wettability, wear resistance in the form of hard coatings and adhesion to coatings for specialized applications, such as super hydrophobicity and hydrophilicity, photocatalysis, layers with piezoresponse for actuators and others.

Many specialized coatings are used in nanotechnology since the desired effects become prominent only at coating (and more importantly, particle) sizes from 100 nm down. This sub-chapter presents applications of metal oxide nanoparticles in conjunction with parent metallic substrate and the possible applications of such systems. It covers typical synthesis and deposition methods for specific metal oxide but focus mainly on hydro- and solvothermal synthesis as this was my method of choice.

Many metals and metallic alloys undergo passive oxidation at ambient conditions which is sometimes desired, when it helps with corrosion resistance, and sometimes less so, especially for processing of materials that require highly reactive starting compounds. Oxygen is always present when it comes to processing and final application of desired material, be it molecular in air for gas reactors or bonded in water as the most common solvent in liquid reactors.

Hydrothermal conditions involve elevated temperatures and high pressures, both critical elements for the pace of passivation as it is strongly diffusion-dependent. Introducing proper precursor, solvent and acidity, it is possible to influence the growth of the oxide coating that would cover the metal in normal circumstances. Such coatings can therefore act as a physical barrier for potential corrosion as well as an inert substrate for the deposition or growth of nanoparticles.

By the formation of layered structure, passive protection of metallic substrate is achieved, allowing it to be used in aqueous environment (or in the atmosphere containing oxygen) while still offering strong support for active nanoparticles on top of it. Mid-layer can also heavily change surface morphology, often increasing the roughness and therefore the surface on which active elements can adhere.

1.6.1 Photocatalytic coatings

Developments in the field of photocatalytic materials in recent years have led to cost-effective solutions for photodegradation of organic compounds in water and air. Clean water availability could directly benefit by cheap treatment devices based on promising photocatalysts. Among many photocatalytic semiconductor metal oxides, TiO_2 and ZnO (with band gaps of 3.2 eV and 3.37 eV, respectively) have been widely used and researched due to excellent chemical, optical and electronic properties and relative low-cost. Photodegradation is achieved by reaction between organic molecules and radical that form on the surface after electrons are excited from valence to conductive band by

UV light irradiation. Recombination of electron-hole pairs decreases the photocatalytic efficiency while increased activity is achieved with the increase in a specific surface area. In the case of TiO_2, anatase crystal form is more stable for particles up to 11 nm [50]. Anatase also shows a higher surface density of hydroxyl groups. Oxygen and water are adsorbed on the surface and initiate photocatalysis faster than in the case of rutile. Commercially, powders with high photocatalytic activity are often a mix of anatase and rutile nanoparticles with proper oxygenated surface for enhanced activity.

TiO_2 photocatalysis is just one in a wide array of methods used for degradation of organic pollutants. Advanced oxidation processes (or AOPs) is an umbrella term that covers processes for total mineralisation of extra-stable organics. It mimics naturally occurring degradation processes that use energy to product intermediates with high oxidation or reduction potential. Generation of highly reactive hydroxyl radicals ($^{\bullet}OH$) is a component of majority of AOPs. It can initiate the oxidation of organic species in three possible ways [51]: by removal of hydrogen from the organic molecule and formation of organic radical alongside water, by the addition to the two- or three-bond atom in a molecule or by the electron transfer to the hydroxyl radicals and formation of second-degree oxidants.

The system with H_2O_2 and UV light radiation has been widely used in the removal of low levels of pollutants in grey- and wastewater and as a disinfectant. A major drawback of the approach is low reaction rates that can be improved by the dissociation of H_2O_2 into two hydroxyl radicals after the breakage of O-O bond by strong UV light of 280 nm wavelength or lower.

Water itself can also be split to form hydrogen and hydroxyl radicals by UV light irradiation below 190 nm. Additionally, hydrated (solvated) electrons (e^-_{aq}) are generated and form superoxide radical anions ($O_2^{\bullet -}$) by combining with dissolved molecular oxygen. Hydrogen atoms can transform into hydroperoxyl radical ($HO_2^{\bullet}$) by reacting with dissolved oxygen molecules. A major advantage of the process involving homolysis of water is the absence of catalyst or other chemical, saving the need for post-processing of cleaned medium [52].

Homogenous photocatalysis is primarily based on Fenton's experiments from the 19th century where he demonstrated the oxidation of tartaric and malic acids by the solution of H_2O_2 and Fe^{2+} salt (Eq. (1.1)). At pH values below 3 the reaction becomes autocatalytic as Fe^{3+} decomposes H_2O_2 into O_2 and H_2O reducing Fe^{3+} to Fe^{2+} at the same time, but the reaction rate is very low. AOPs nowadays use the so-called photo-Fenton reaction based on Fenton's work with the addition of photoreduction of Fe^{3+} ions and its complexes in acidic pH (2.5–5). This way, Fe^{2+} ions recycle continuously by the irradiation of Fe^{3+}-H_2O complexes and are not depleted during the course of the oxidation reaction (Eq. (1.2)). $Fe(OH)^{2+}$ complex absorbs in the UV/Vis range below 400 nm, allowing the utilizing of solar light for catalysis.

Ozone is a widely used homogeneous photocatalyst due to its highly selective reactions and the reactions of hydroxyl radicals which decompose from the ozone in water. Ozonation is widely used and successfully applied to many water treatment procedures thanks to reactive terminal electrophilic oxygen atoms.

$$Fe^{2+} + H_2O_2 \rightarrow Fe^{3+} + OH^- + HO^{\bullet} \tag{1.1}$$

$$[Fe(OH)]^{2+} + h\nu \rightarrow Fe^{2+} + HO^{\bullet} \tag{1.2}$$

Heterogeneous photocatalysis, on the other hand, uses two different phases, the medium and (usually) solid semiconductor catalysis (TiO_2, ZnO, CdS, $SrTiO_3$, etc.) that

help with the generation of reactive species such as superoxide radical anions and hydroxyl radicals. Semiconducting nature of catalyst produces these species after photogeneration of electron/hole pairs on the surface of the catalyst.

Ozone and H_2O_2 pose a health and environmental risk and should be carefully removed after the process. Photo-Fenton reactions are used in solar-powered systems without the need of dedicated UV lights since sunlight with a wavelength up to 450 nm is adequate. The main disadvantages of the photo-Fenton process are low pH conditions and removal of iron at the end of the process. Heterogeneous photocatalysis, especially on immobilised semiconductor oxides, is a promising technology that could lower the environmental impact due to limited secondary pollution and lower the costs of the whole process, making the technology available for mass deployment in places where traditional waste-water cleaning processes are infeasible.

1.6.1.1 Titanium dioxide - TiO_2

TiO_2 is a naturally occurring oxide of titanium. It belongs to the family of transition metal oxides. Industrial production of TiO_2 started at the beginning of the 20^{th} century after it replaced lead oxide as a white pigment in paints. It has low light absorption and high scattering capabilities, which gives it a distinctive white colour. Its high refractive index (2.4) makes titanium dioxide useful in many applications, mainly as a white pigment for food, cosmetics, textiles, wall paints, and pharmaceutics, as anti-reflection coating in silicon solar cells and other optical devices, as reflective component in sunscreens, and many others. Nano-sized TiO_2 has some niche uses: as catalyst for selective reduction of NO_x to N_2, for decomposition of organics via photocatalysis, for hydrogen production (water splitting), as a key element in dye-sensitized solar cells (DSSC), as a reversibly intercalating material for anode in lithium batters and many others [53].

TiO_2 occurs in three main crystal structures: rutile, anatase and brookite (Figure 1.10). Rutile is thermodynamically the most stable polymorph with a tetragonal crystal structure at all temperatures and pressures up to 60 kPa [53]. Anatase also crystallises in the tetragonal crystal system where titanium ions have octahedral coordination with six oxygen ions while oxygen is surrounded with three titanium ions. In rutile there is only corner-sharing and in anatase also an edge-sharing of octahedra. Brookite is less common and has an orthorhombic structure. The difference in the Gibbs free energy is minimal between the three polymorphs, which contributes to their stability at ambient conditions. The metastable anatase and brookite phases transform to rutile upon heating to temperatures above 600 °C.

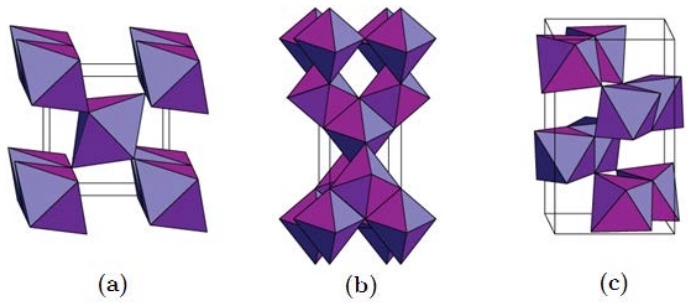


Figure 1.10: The three main TiO_2 polymorphs: (a) metastable, tetragonal rutile, (b) tetragonal anatase and (c) orthorhombic brookite.

The stability of different polymorphs also depends on the particle size. Rutile is the stable form for particles 35 nm or more in size while anatase particles are generally smaller than 11 nm. Brookite is stable when TiO_2 is between 11 and 35 nm [50].

1.6.1.2 Synthesis of TiO_2 nanoparticles and coatings

Titanium dioxide can be synthesised in the form of a powder, single crystals or thin films with various thicknesses ranging from a few nanometres to micron-sized particles or larger agglomerates. Smaller particles tend to agglomerate so special care should be taken concerning synthesis method and handling with final material or intermediates before their deposition.

Physical and chemical properties of TiO_2 depend strongly on the preparation method. Generally, TiO_2 synthesis methods can be divided to gas-phase and solution methods. Physical vapour deposition (PVD), chemical vapour deposition (CVD), spray pyrolysis (SPD) and sputtering are typical gas-phase methods for the deposition of a final compound on a substrate after forming it by chemical reaction, decomposition of a precursor, directly from a gas phase for those compounds that are stable in the gas phase or by aerosol formation and deposition in the case of spray pyrolysis. Solution routes are especially convenient for deposition of thin films via dip-coating or spin-coating techniques. Homogeneity of products and the ability to form complex composites with great control over stoichiometry are the main advantages of those methods. Typical solution methods are hydro- and solvothermal synthesis, sol-gel, electrochemical methods, precipitation (reduction by irradiation), microemulsion and combustion method.

In my work, initial steps of sol formation were used with solvo- or hydrothermal after-treatment. This gives us the benefit of great control of precursor hydrolysis, formation of desired intermediates along with high crystallinity and homogenous substrate coverage due to the hydrothermal step. Sol-gel process employs colloids of a metal or metalloid element surrounded by organic ligands as precursors. Those are often metal alkoxides that readily react and decompose in water. Common TiO_2 precursors are titanium isopropoxide ($Ti[OCH(CH_3)_2]_4$) and titanium butoxide ($Ti[O(CH_2)_3CH_3]_4$) (Figure 1.11).

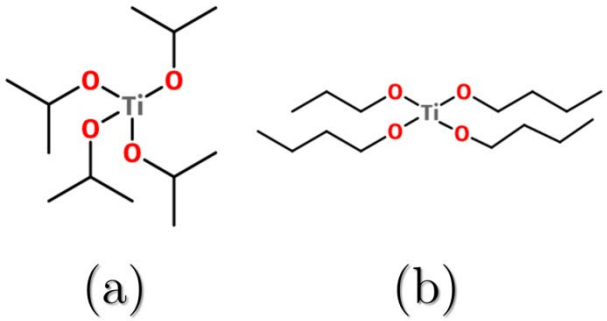


Figure 1.11: Structural formulas of two alkoxides used as Ti precursors: (a) titanium isopropoxide and (b) titanium butoxide.

Titanium alkoxide hydrolysis partially dissociates one chain of the alkoxide to titanium complex and alcohol (Eq. (1.3)). Partially hydrolysed products can combine with O-O bridges in condensation reaction with either alcohol (Eq. (1.4)) or water as a by-product (Eq. (1.5)). Both reactions are usually quick and exothermic. To obtain

desired sols, stabilising agents have to be added to control the rate of hydrolysis and condensation.

$$Ti(OR)_4 + H_2O \rightarrow HO\text{-}Ti(OR)_3 + ROH \qquad R = \text{alkyl radical} \tag{1.3}$$

$$(OR)_3Ti\text{-}OH + HO\text{-}Ti(OR)_3 \rightarrow (OR)_3Ti\text{-}O\text{-}Ti(OR)_3 + ROH \tag{1.4}$$

$$(OR)_3Ti\text{-}OH + HO\text{-}Ti(OR)_3 \rightarrow (OR)_3Ti\text{-}O\text{-}Ti(OR)_3 + H_2O \tag{1.5}$$

Cross-linked sols are obtained after continuous condensation and polymerisation of metal-containing molecules. The final result of condensation/polymerisation reactions is a gel, consisting of a three-dimensional network that extends throughout the solution. As most gels are amorphous, a final step is needed for crystallisation of the final product. This can be achieved by annealing at high temperatures or with hydrothermal treatment of the gel. Since amorphous TiO_2 is not photocatalytic, crystallisation is a necessary step in the catalyst preparation, achieved by heating (annealing, HT).

1.6.1.3 Primary processes upon irradiation of TiO_2

Adsorption of photons on semiconductor surface initiates photo-induced reactions such as photodegradation of organic compounds and water splitting (H_2 generation). Titanium dioxide has so far been proven to be the most promising semiconductor photocatalyst, both in fundamental studies and practical applications due to its high photoactivity and availability, chemically and biologically is largely inert when not UV irradiated, it is nontoxic and has high photonic efficiency of around 10%. Degradation mechanism for different pollutants on a photocatalysis varies but primary responsible reactions are always interfacial redox reactions of electrons and holes that are generated after irradiation of semiconductor catalyst with a light of sufficient energy [54].

The anatase band gap is 3.2 eV which corresponds to a wavelength of 388 nm. This makes it photocatalytic under UV light. The band gap of rutile is smaller (3.0 eV, 413 nm) and thus better photocatalytic properties would be expected, but photocatalytic activity is based on other factors as well:

- Due to the smaller energy differences between conductive and valence band in rutile, the recombination of electrons with positive holes is quicker.
- Anatase shows higher surface density of hydroxyl groups. Oxygen and water are adsorbed on the surface and initiate photocatalysis faster than in the case of rutile.
- Smaller particles have a larger specific surface area which enhances photodegradation of organic compounds.
- The presence of trap states can limit recombination and thus increase photocatalytic yield

Schematic representation of semiconductor irradiation process is described in Figure 1.12 and the electron/hole pair generation process with (Eq. (1.6)). Photogenerated e^-_{CB} and h^+_{CV} are conduction band electron and positive hole in the valance band, respectively. Pairs are created in the outer surface region of the material because of the short penetration depth δ_p ($\delta_p \approx 160$ nm). Migration of both species to the surface of the semiconductor and in contact with electrolyte forms a Schottky-barrier. The electric field produced by the Schottky-barrier introduces a separation of e^-_{CB} and h^+_{CV} in opposing

directions which causes the bending of the energy bands at the solid-liquid interface and subsequent retardation of undesired recombination. The Fermi level of the semiconductor then moves to equilibrate with the potential of the redox couple. Both types of charge carriers transit to surface trapping sites in the picosecond range.

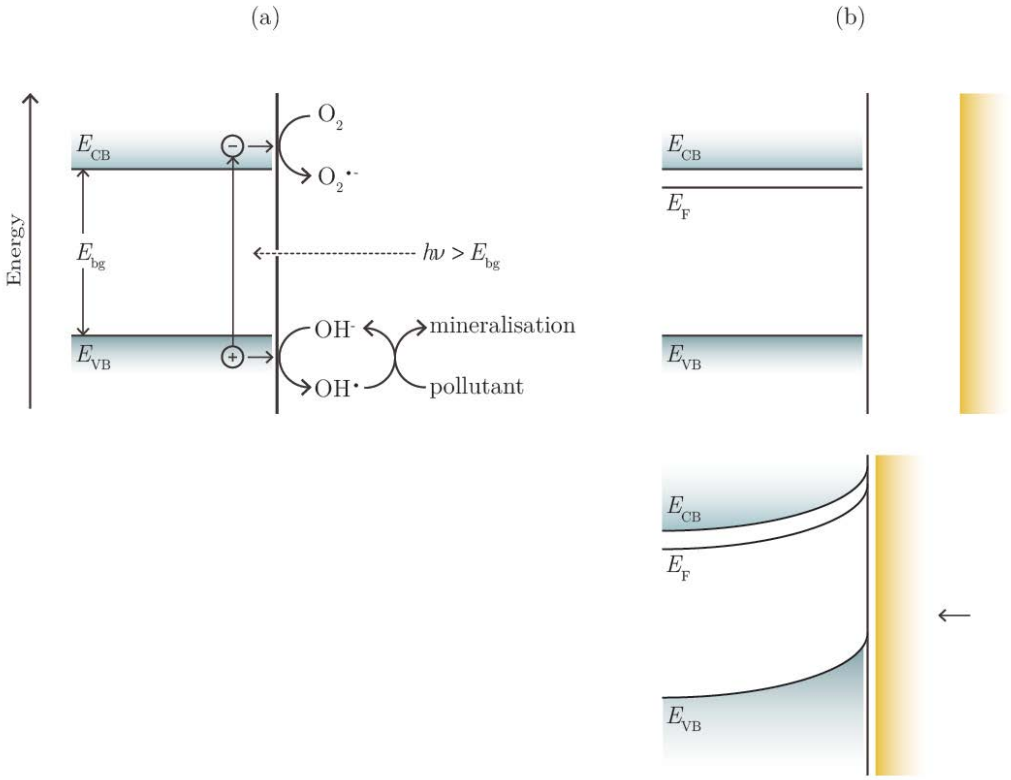


Figure 1.12: (a) Schematic representation of primary processes upon UV irradiation of photocatalytic semiconductor material. Light with the energy greater than E_{bg} excites the electron to conduction band. (b) Band structure change upon contact with electrolyte [55], [56].

$$TiO_2 + h\nu \rightarrow TiO_2\ (e^-_{CB} + h^+_{VB}) \tag{1.6}$$

Studies show that Ti(IV) cations on TiO_2 particles are reduced by the light-induced electrons forming Ti(III) cations [57]. In most cases, O_2 is present to act as the primary electron acceptor. Electrons, trapped as Ti(III), are transferred to adsorbed O_2 at the semiconductor surface yielding superoxide ($O_2^{-\cdot}$) (Eq. (1.7) and (1.8)) and possibly, depending on the pH, hydroperoxyl radical ($HO_2^\cdot$) (Eq. (1.9)).

$$e^- + O_2 \rightarrow O_2^{-\cdot} \tag{1.7}$$

$$O_2^{-\cdot} + HO_2^\cdot + H^+ \rightarrow H_2O_2 + O_2 \tag{1.8}$$

$$HOOH \rightarrow HO_2^\cdot + {}^\cdot OH \tag{1.9}$$

Besides the electron transfer from the semiconductor to adsorbed O_2 there is also the direct transfer to an organic molecule, yielding an organic radical anion. In contrast with reduction reactions caused by excited electrons, the positive holes react with water molecules on the surface of semiconductor producing hydroxyl radicals and protons (Eq. (1.10)) or hydrogen peroxide that dissociated to hydroxyl radicals (Eq. (1.11) and (1.12)).

$$h^+ + H_2O \rightarrow H^+ + {}^{\cdot}OH \tag{1.10}$$

$$2\ h^+ + 2\ H_2O \rightarrow 2\ H^+ + H_2O_2 \tag{1.11}$$

$$H_2O_2 \rightarrow 2\ {}^{\cdot}OH \tag{1.12}$$

It remains elusive whether holes react directly with the organic compounds or whether they react first with water molecules to produce hydroxyl radicals, which then react further. This question is causing controversy within the photocatalysis community, but work by *Fujishima* has shown that photocatalytic contributions from holes are important [58]. It was found that the measured quantum yield (QY) values that could be attributed to a reaction involving hydroxyl radicals were several orders of magnitude smaller than those that could be attributed to reactions involving holes. While the main reaction mechanism pathways on irradiated TiO_2 surface are known, a lot of research is still conducted on time-resolved analysis of photocatalytic process and determining distinct QY values for electron and hole transfer steps.

1.6.1.4 Determination of TiO_2 photodegradation efficiency

Total mineralisation is seldom achieved. While some ISO standards for photocatalysis measurements exist [59], many different degradation methods and model molecules are used. For fundamental research, molecules such as 2-propanol and phenol are suitable candidates due to their known degradation pathway. In the case of 2-propanol, a simple and direct photodecomposition to acetone can be observed with a high degree of sensitivity by gas chromatography. The mechanism of photodecomposition of 2-propanol does not involve chain reactions since a single photon participates in the generation of an acetone molecule. Quantum yield is therefore equal to the ratio of the number of generated acetone molecules to the number of absorbed photons.

Photocatalytic efficiency depends on a catalyst used and its amount, reaction conditions, intensity and wavelength of the light source, concentration of O_2 and model molecule. Degradation is usually presented as a percentage of degradation, degradation rate, or half-life. Because of largely unstandardised conditions and different experimental factors, the data is difficult to compare. Total quantum yield appears to be the most promising solution, not dealing with the type and rate of decomposing organics but rather with efficiency of photon-electron transfer. It is usually defined as the ratio between the number of molecules undergoing an event and the number of photons absorbed by the reactant.

Simple photocatalytic measurements can be successfully done by following the decolouration of dyes as in the case of methylene blue (MB) [60]. Prompt removal of colour can be observed after TiO_2/UV-based photocatalysis while simultaneously oxidising the dye, followed by mineralisation of carbon, nitrogen and sulphur heteroatoms into CO_2, NH^{4+}, NO^{3-} and SO_4^{2-}, respectively. Caffeine (1,3,7-trimethylxanthine) is also

used as a sample molecule as its degradation has been already investigated in an aqueous suspension. Another advantage of using the caffeine is a distinct spectral peak around 270 nm without overlapping which makes determining the time-dependent concentration changes with UV/VIS spectroscopy straightforward [61]–[63].

1.6.2 Coatings and surface wettability

Wettability is an important property of a material that describes the tendency of liquids to spread on a solid surface, measured in terms of the "contact" angle at the triple junction between phases. It is a result of intermolecular interactions between the liquid and the substrate, manifesting as attracting or repulsive forces.

Wetting shapes many processes in a wide size range. As a direct result of surface tension, it dictates crystallisation and solidification mechanisms. On a macroscopic scale, it is a key property for metallurgical binding. Quality of solid-solid interface bonding or adherence after soldering is directly linked to liquefied solder wetting interaction with the substrate. A liquid spreading on a substrate with no interaction with substrate material is known as non-reactive or inert wetting whereas the wetting process influenced by reaction between the spreading liquid and substrate material is known as reactive wetting.

The most basic wetting description is equilibrium of droplet on an ideal (physically and chemically inert, flat, smooth, homogeneous and rigid) surface, given by Young's equation (1.13) and schematically shown in Figure 1.13 [64]–[66]. Force equilibrium at the contact between gas, liquid and solid (represented by three interfacial tensions between phases γ_{ab} where a and b subscripts indicate *s, l, g*, that is the solid, liquid and gas phases, respectively).

$$\gamma_{sg} = \gamma_{sl} + \gamma_{lg}\cos(\theta) \tag{1.13}$$

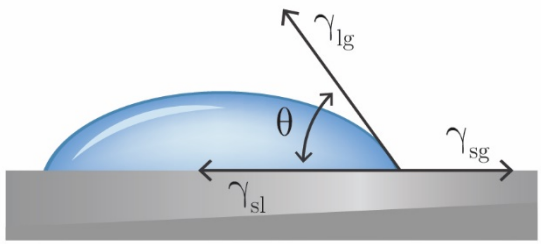


Figure 1.13: Force equilibrium at the triple junction of solid, liquid and gas phase represents Young's equation.

While Young's equation provides a fundamental insight into the surface relations, such conditions (non-reactive liquid, flat and smooth surface, etc.) are rarely met in practice. Nevertheless, Young's equation is the most fundamental starting point for understanding of the complex field of wetting. Dupre defined the work of adhesion between solid and liquid in Equation (1.14) [67].

$$W_{sl} = \gamma_{sg} + \gamma_{lg} - \gamma_{sl} \tag{1.14}$$

Combining Dupre's relation with Young's work gives Young–Dupre Equation (1.15).

$$W_{sl} = \gamma_{lg}(1 + \cos(\theta)) \tag{1.15}$$

Relation in the equation postulates that neither γ_{sg} nor γ_{sl} can be larger than the sum of the other two surface energies. For the given value γ_{lg} the increase in contact angle means decrease in solid-liquid adhesion. As a boundary condition, contact angle of 180° means zero adhesion on liquid-solid interface therefore a complete non-wetting condition. This is experimentally problematic to achieve; falling droplet in the air or moving up or down due to density difference in non-mixing liquid can facilitate such conditions in a moment just before hitting the surface/solid. For contact angles above 90°, the liquid is considered as non-wetting the solid. Moreover, contact angles below 90° indicate that liquid wets the surface. Water droplets tend to move around with ease on hydrophobic (contact angle 90° or higher) and are not stuck in holes and pores due to capillary effect. Good wettability is expected when the sum of γ_{sg} and γ_{sl} is as low as possible while γ_{lg} remains large (Figure 1.14).

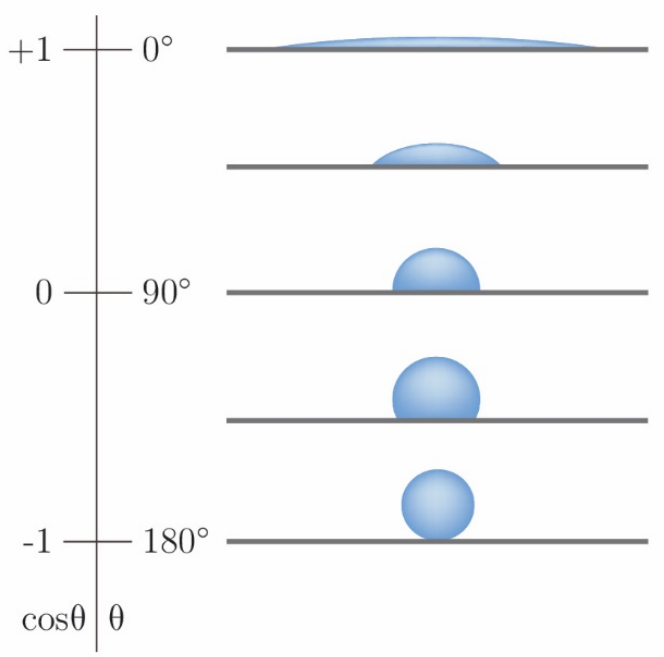


Figure 1.14: Droplet-surface relations and contact angle; from superhydrophilic (close to zero degree) to superhydrophobic (above 150 degrees).

Non-ideal surfaces introduce many problems and are somewhat problematic in the theoretical explanation of wetting. Due to local differences in roughness and other imperfections, a range of contact angles exists around the contact line of a static droplet. This can be demonstrated on a surface where a drop sticks to the solid even when tilted. The difference between advancing (largest) and receding (smallest) contact angles is the cause for contact angle hysteresis [68]. Such heterogeneous wetting pattern is common when geometrical material surface is a composite of two types of patches. An example of such surface is a combination of solid and gas due to extensive roughness and air trapped in between the rough surface features. Such surfaces are intrinsically more hydrophobic since the actual contact surface is much smaller than it would be on an ideal flat surface. In a case when the droplet size is comparable to the size of the surface features, capillary

effects and line tension should be considered. Wenzel and Cassie–Baxter models both attempt to describe relations between a liquid and the wetting of textured surfaces.

Wenzel introduced the correction roughness factor to the contact angle (Eq. (1.16)), describing homogenous wetting pattern on rough surface (Figure 1.15) [69]. The apparent contact angle (θ^*) is defined on rough but homogeneous surface and is referred to as Wenzel angle. Composite (or Cassie) angle describes the situation on smooth, heterogeneous surfaces. Roughness ratio (r) in Equation (1.16) describes how roughness affects a homogenous surface and is defined as a ratio between true and apparent area of a droplet.

$$\cos(\theta^*) = r\,\cos(\theta) \tag{1.16}$$

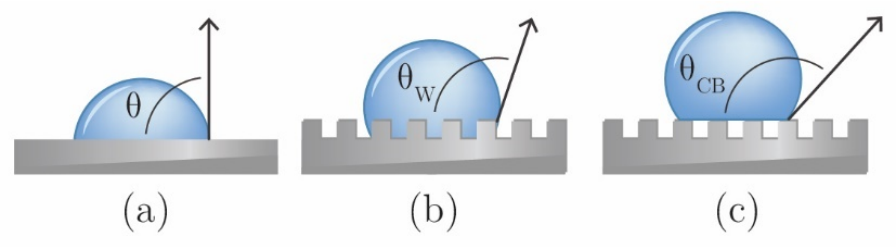


Figure 1.15: Different relations between the droplet and the surface: (a) ideal surface and Young's contact angle, (b) rough but homogeneous surface and Wenzel angle (θ_W) and (c) Cassie-Baxter hydrophobic state when various phases and materials are involved.

The Wenzel model does not account for non-homogeneity of the surface as well as contact angle hysteresis. When various phases and materials are involved, a new model was proposed, summarised in the Cassie-Baxter equation (1.17) [70], [71]. Following the Wenzel equation, Cassie and Baxter equation adds two factors that account for the difference between apparent and actual contact area. r_f is defined as roughness of a surface in contact with liquid and f as the fraction of a solid surface in contact. For $f = 1$, apparent surface is the same as actual surface and Cassie-Baxter equation becomes the Wenzel equation. In the Cassie-Baxter state, air is trapped in a composite structure solid-air, forming a hydrophobic surface, which results in a large contact angle.

$$\cos(\theta^*) = r_f\ f\cos(\theta) + f - 1 \tag{1.17}$$

The sum of all different surface fractions with a different roughness f_i is summarised in Equation (1.18), where γ_{lg} is the liquid-gas surface tension, $\gamma_{i,sg}$ and $\gamma_{i,sl}$ are surface tensions of each component for solid-gas and solid-liquid interface, respectively [72]. For the two-component system, such as hydrophobic substrate with air trapped in between underlying pillars (or other distinct morphology), Equation (1.18) translates to (1.19) under the assumption that the air that is exposed is under the droplet and is the only other substrate in the system, hence the expression (1 - *f*).

$$\gamma_{lg}\,\cos(\theta^*) = \sum_{n=1}^{N} f_i\,(\gamma_{i,sg} - \gamma_{i,sl}) \tag{1.18}$$

$$\gamma_{lg}\,\cos(\theta^*) = f_1\,(\gamma_{1,sg} - \gamma_{1,sl}) - (1 - f_1)\gamma_{lg} \tag{1.19}$$

The criterion for suspension in the Cassie-Baxter state or collapse to the Wenzel state can be calculated by contact line density (Λ) using the Extrand model [73]. Contact line density is defined as the total perimeter of asperities over a given surface area. Critical values of the contact line density can be calculated from contact angles, asperity shape, and information about the contact liquid, such as density and surface tension, surmised in Equation (1.20) where ρ is the density of the droplet, g is gravitational acceleration, V is the volume of the droplet, θ_a is the advancing apparent contact angle, $\theta_{a,0}$ is the advancing contact angle of a smooth substrate, γ is the surface tension of the liquid and ω is the rise angle of the side of the asperities (tower wall angle).

$$\Lambda_C = \frac{-\rho g V^{\frac{1}{3}} \left(\left(\frac{1-\cos(\theta_a)}{\sin(\theta_a)} \right) \left(3 + \left(\frac{1-\cos(\theta_a)}{\sin(\theta_a)} \right)^2 \right) \right)^{\frac{2}{3}}}{(36\pi)^{1/3} \gamma \cos(\theta_{a,0} + \omega - 90)} \tag{1.20}$$

Contact line density (Λ), which is the length of the asperity perimeter per unit area that could potentially suspend a liquid drop, is defined as the product of the feature perimeter (p) and δ (Eq. (1.21)).

$$\Lambda = p\delta \tag{1.21}$$

Contact line density for an array of square posts (Figure 1.16) is $\Lambda = 4x/y^2$.

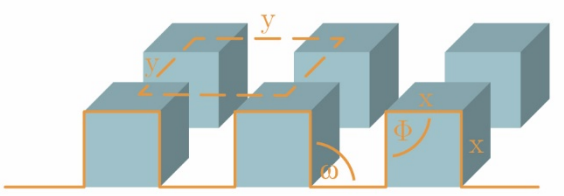


Figure 1.16: Extrand surface with ideal geometrical shapes. Asperities will cause a droplet into the Cassie-Baxter state for $\Lambda > \Lambda_C$.

The droplet will be suspended by the asperities in the Cassie-Baxter state when $\Lambda > \Lambda_C$ or it will collapse in the asperities and the contact will be solely liquid-solid (Wenzel). Advancing (θ_a) and receding (θ_r) contact angles (due to hysteresis) in the Cassie-Baxter state are calculated following equations (1.22) and (1.23) where λ_p is the linear fraction of the contact line on the asperities, $\theta_{r,0}$ is the receding contact angle of a smooth substrate and θ_g a contact angle on liquid-gas interface.

$$\theta_a = \lambda_p(\theta_{a,0} + \omega) + (1-\lambda_p)\theta_g \tag{1.22}$$

$$\theta_r = \lambda_p\theta_{r,0} + (1-\lambda_p)\theta_g \tag{1.23}$$

Contact angles on collapsed "Wenzel" drops are Eq. (1.24) for advancing angles and Eq. (1.25) for receding angles.

$$\theta_a = \lambda_p(\theta_{a,0} + \omega) + (1 - \lambda_p)\theta_{a,0} \tag{1.24}$$

$$\theta_r = \lambda_p(\theta_{r,0} - \omega) + (1 - \lambda_p)\theta_{r,0} \tag{1.25}$$

Proper and reliable measurements of the contact angle are important for analysing the wetting behaviour. Techniques involving sessile drop and wetting balance have been proven to provide reliable data and offer great versatility with the measuring method. With the sessile drop method, a goniometer with an optical subsystem is used. The liquid droplet is placed on a substrate in an optical pathway between a light source and a high-resolution camera. The contact angle is calculated by analysing the capture profile image of a droplet. A wide array of contact angles can be observed this way thanks to high frame rate cameras. By gradual volume addition on the same spot, a dynamic sessile drop method can measure the largest contact angle possible without increasing its solid-liquid area underneath (advancing angle). By the removal of liquid, the smallest possible angle is obtained (receding angle). Other measuring techniques are the pendant drop method, the dynamic Wilhelmy plate method and measurements of capillary rise with the Washburn's equation.

1.6.2.1 Superhydrophilicity of TiO_2 coatings

Titanium dioxide is one of the few materials that exhibit more than one photo-induced phenomenon: the well-known photocatalytic property, which was covered in detail before, and the so-called superhydrophilicity [74], or a state of high wetting, discovered in 1995. Many metal oxides display a variety of photoinduced effects and some of them have been examined for potential photocatalytic and/or hydrophilic properties. Even though they are both a consequence of UV irradiation, they are intrinsically different processes and must be observed as such. Superhydrophilicity, however, cannot happen without processes involved in photoexcitation and generation of electron/hole pairs. But good photocatalytic properties do not translate into high wetting and vice versa. Among metal oxide semiconductors, all four combinations are possible: that both the photocatalytic and the hydrophilic effect are observed, that either photocatalytic or hydrophilic effect is observed or that neither effect is observed.

There is no clear proposed mechanism for photo-induced superhydrophilicity on TiO_2. The method concerning the generation of surface vacancies, photo-induced reconstruction of Ti-OH bonds and photocatalytic decomposition of organic adsorbents have all received their share of support [75]–[78]. Upon UV illumination, electrons reduce Ti(IV) cations to the Ti(III) state and O^{2-} anions are oxidised by the positive holes. In this way, oxygen atoms are removed from the surface, creating oxygen vacancies which can be occupied by water molecules. Those, in turn, produce OH groups on the surface, making it hydrophilic (Figure 1.17). Longer UV irradiation produces more vacancies; in most cases, the contact angle drops to 15° or less in 30 min.

Droplets that fall on the superhydrophilic surface spread evenly across the surface, forming a film. This is the basic principle of anti-fogging mirrors. Usually, the reflection is distorted due to imperfections and shadowing when the light passes through the droplet and scatters. Those effects are avoided on the superhydrophilic surface as the uniform water film does not cause such effects.

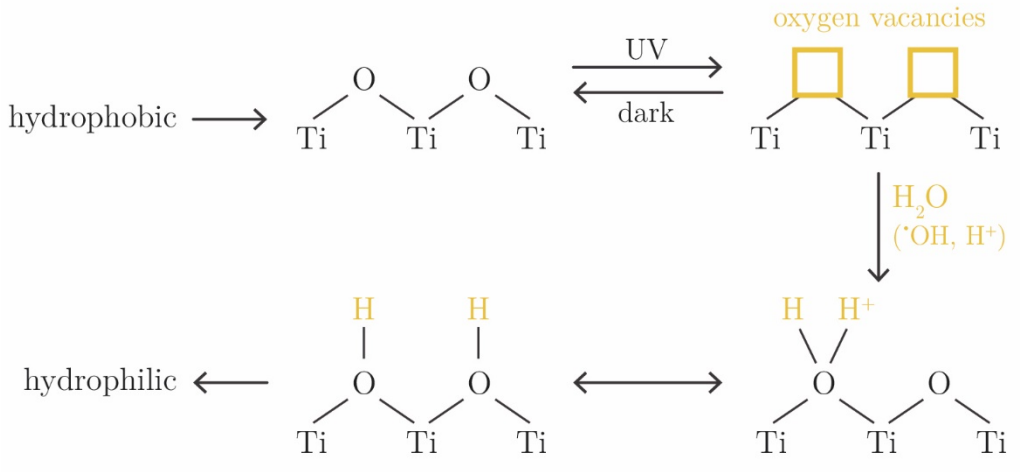


Figure 1.17: Schematic representation of oxygen vacancies generation as a consequence of UV irradiation. Further reactions with dissociated water produce superhydrophilic surfaces [75].

Photocatalytic properties of TiO_2 are enhanced by exposing more reactive facets. Similar is true for superhydrophilicity. Ejection of oxygen anions that are only bonded with two Ti^{4+} cations is more probable compared to those bonded with three. Crystal facets that contain a larger number of bridging oxygen atoms which also have a smaller number of bonds are easier to remove and therefore more likely to be hydrophilic. Rutile (100) and (110) facets behave as such. It was found that (001) facet acquires less OH groups and is in fact less hydrophilic than the other two facets (Figure 1.18).

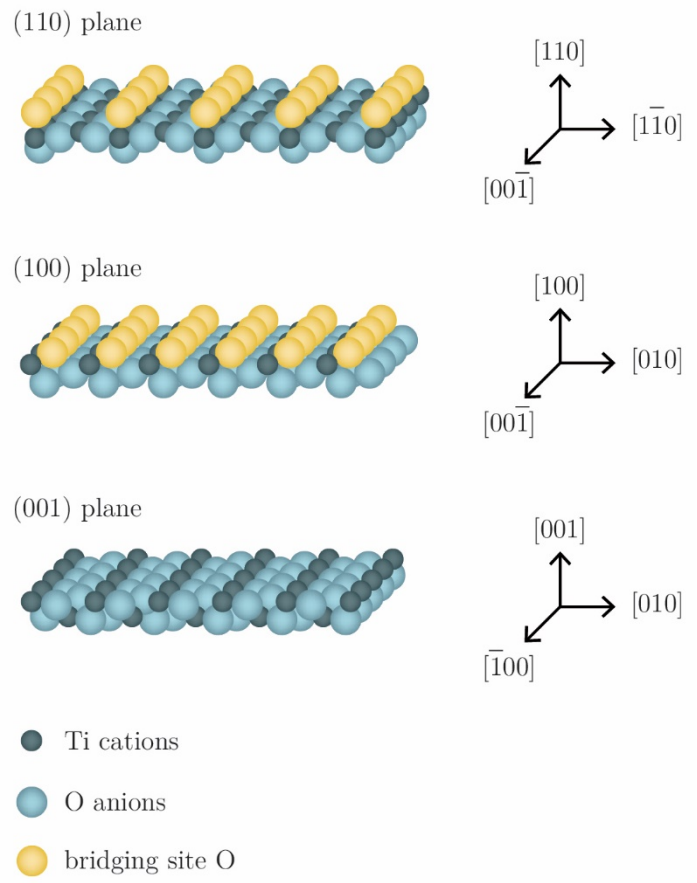


Figure 1.18: Ti facets have different terminal atom configuration. Facets with bridging oxygen atoms are more favorable for hydrophilic applications [75].

High wetting can also be temporarily achieved by plasma treatment of the surface but relaxation time is quite fast, typically around a few hours. Oxygen plasma, due to the oxygenation of the surface, produces a more hydrophilic characteristic than pure argon plasma.

1.6.2.2 Superhydrophobicity (Lotus effect) on ZnO coatings

Water repelling surfaces, in general, have received much attention with the advent of nanotechnological applications. Superhydrophobicity is a surface condition, governed by both the hierarchical geometrical structure and the chemical composition. The surface is considered superhydrophobic when the static contact angle is 150° or higher and the sliding angle is less than 15°. To achieve the Cassie-Baxter state, a dual-layer cooperative structure is necessary; substrate with low surface free energy (usually achieved by additional coating) and rough surface. Inspiration for such dual-layer structure comes from mimicking the nature. This phenomenon was first observed on the leaves of the lotus plant (*Nelumbo nucifera*), caused by characteristic micro- and nanoscale structures in surface roughness (Figure 1.19). The same effect was later observed on other plants, such as cane, prickly pear (*Opuntia*) and others, as well as on certain insects [79]. Dirt particles on the surface adhere to water droplets which then slide away easily due to great droplet mobility provided by superhydrophobicity, resulting in self-cleaning property.

Man-made superhydrophobic surfaces are produced either by the preparation of rough surface and coating it with low surface energy molecules that are intrinsically water repellent, or by roughening an already hydrophobic material. This can be achieved in many ways, most commonly by sol-gel, CVD, layer-by-layer deposition, etching, lithography and others [80]. Water repellent surfaces have a wide range of potential applications, such as non-icing windows and anti-snow tiling, low friction solid-liquid systems, protective coatings, antibacterial surfaces and others.

As previously mentioned, zinc oxide can crystallise in a variety of morphological shapes. Narrow hexagonal ZnO rods, growing from the same seed in the form of a spiked ball (hedgehog-like), a honeycomb-like structure and a ZnO nano-forest are a few of the possible structures that can work as a basis with sufficient roughness for further hydrophobic coating application.

Chemicals that are used for top-most hydrophobic coating have to have a cross-link, either between each other or to the surface (or both), nonpolar chain or steric barrier to induce hydrophobicity and general lack of affinity to water. Some examples are stearic acid, polystyrene and a variety of silanes (Si-based metalorganics with nonpolar chains).

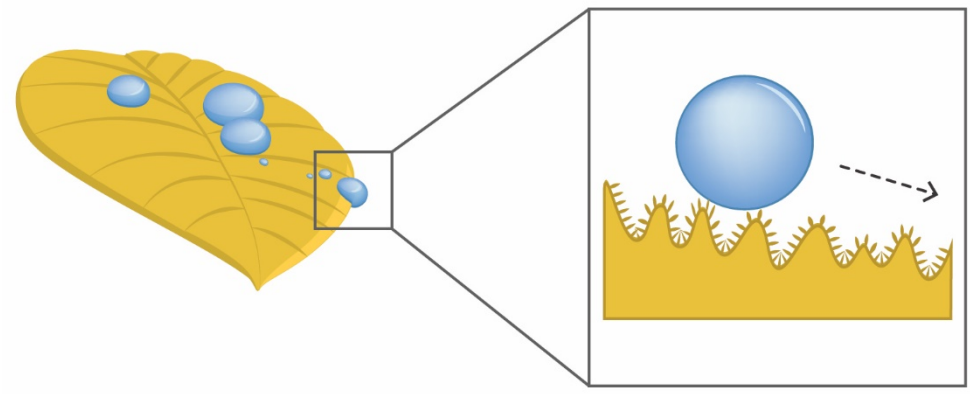


Figure 1.19: Self-cleaning effect on lotus leaf. Appropriate roughness and waxy hydrophobic coating make the surface of the lotus leave superhydrophobic.

1.6.3 Coating with improved dielectric response

Aluminium is an important material in the microelectronics industry, especially in the production of capacitors, either as an electrode in film capacitors or as a substrate for the dielectric layer in the form of aluminium-based oxides and hydroxides in electrolytic capacitors [81]. The dielectric layer in the latter is usually prepared by anodisation of aluminium in an acidic medium. In film capacitors [82], [83], pure aluminium is usually used. To improve the dielectric properties of the material the addition of another thin insulating barrier with suitable dielectric properties is proposed [84]. It has been reported that hydrothermal treatment provides an improvement in the production of high-stability, crystalline, anodic aluminium oxide for electrolytic capacitors. The nano-porous amorphous oxide layer obtained by anodisation is converted to a crystalline barrier layer [85]. Another study shows that the anodic growth can be enhanced with a prior hydration treatment [86].

Boehmite is a widely used aluminium oxyhydroxide (γ-AlO(OH)), used as a precursor for many aluminium oxide materials, such as membranes [87], [88], coatings [89], [90], in the preparation of ceramic catalysts [91], adsorbents [92] and materials for orthopaedic

and dental applications [93], [94]. Hydrothermal synthesis of boehmite 1D and 2D structures is well documented in the literature, mostly synthesised in the form of micro or nanoparticles from solution with aluminium precursor, such as $Al(NO_3)_3$ [95], [96].

Hydrothermal treatment provides economic and ecological advantages over anodizing, which requires additional electrical power and aggressive chemicals [97]. A simple hydration treatment of aluminium can be achieved, even in boiling water or elevated gravity conditions (centrifuge) [98], but studies show that below 90 °C an amorphous pseudo-boehmite is formed [35], [99]. The crystallinity increases with an increasing temperature of the synthesis and preparation conditions [100]. Pseudoboehmite is a disordered Al_2O_3 with the composition $Al_2O_3 \cdot x\ H_2O$ $(2.0 > x > 1.0)$ where $x = 1.0$ corresponds to a well-crystallized boehmite ($(\gamma$-AlO(OH)) [101].

Hydrothermal treatment of the aluminium foil material can improve the dielectric properties in foil capacitors by the addition of hydrothermally prepared insulating boehmite barrier layer at the surface of aluminium.

1.6.4 Bacteriostatic coatings

Bacterial adhesion on different surfaces is relevant for implications to the human health and the environment. It causes major problems in many fields, such as the pharmaceutical and food industry. Studies have shown that adhesion of bacteria and spores can be inhibited by proper surface treatment and understanding the processes involved with bacterial adhesion. The process is affected by various physical and chemical properties, both bacterial and those substrate-related. Environment (temperature, pH), surface roughness, surface charge and contact angle all contribute to the adhesion level as well as hydrophobicity, flagellation and motility of the bacteria.

The adhesion process is generally described as a two-step kinetic binding model with initial, rapid and reversible binding between the micro-organism and the substrate. The interaction free energy of the adhesion, mainly governed by electrostatic, van der Waals, and hydrophobic effects and contact interactions, has two minima. A weak and reversibly bound interaction appears at a separation of approximately 10 nm. The second minimum exists at a distance of 1 nm and is governed by strong and irreversible adhesion of bacteria due to adhesion proteins expressed on the surface and binding molecules on the substrate.

Bacterial adhesion to the surface is an essential step in bacterial pathogenesis. Like the *in vitro* tissue cells, bacteria prefer to grow on available surfaces rather than in the surrounding aqueous phase. Bacteria experiences frequent shear forces which need to be overcome if it wants to remain in the desired environment and form a colony or biofilm. Bacterial adhesins are selective molecules that bind to surfaces which is generally beneficial for bacterial growth. Changing the surface characteristics such as roughness or hydrophobicity can therefore have an impact on bacterial adhesion and growth. Various experimental methods are available for studying bacterial attachment [102]. Below is a brief overview of direct and indirect observation methods along with suitability for our application (Figure 1.20).

1.6.4.1 Direct bacteria attachment determination methods

Direct observation methods can detect microbial colonisation directly and usually offer great insight to both quantitative and qualitative adhesion characteristics.

Light microscopy is the oldest and well-proved method utilising simple, inexpensive and readily available equipment. As with many other microscopy techniques, it is possible to quickly estimate the degree of microbial attachment and colonisation, as well

as determine the exact attachment points such as individual cell attachment, clumps or biofilm growth, association with special surface structure or by the expression of extracellular materials.

For a more detailed observations and/or 3D structure of bacterial film, *laser-scanning confocal microscopy* can be used. Combining laser illumination, confocal imaging and computer based image processing, this method overcomes many limitations of basic light microscopy, producing 3D images of the specimen in high-resolution by combining precise 2D images at different focal levels. Specific elements can be further enhanced by introducing fluorescent dyes. This method is invaluable for the *in situ* morphological studies of complex microbe-surface interactions. With the instrument, it is possible to visualize specific elements in bacteria and see through the transparent specimens while constructing 3D images. Limitations of both light and confocal microscopy come from physical wavelength limitations due to diffraction (Abbe diffraction limit). Electron microscopy overcomes this limitation and allows the insight into the sub-micron size range.

Transmission electron microscopy (TEM) usually utilises gold-labelled antibodies which allow for identification of specific antigenic structures on the microbe. It is less suitable for bacteria count due to high magnifications, difficult sample preparation and often sparse bacteria attachment which may lead to the trouble locating cells in contact with the substratum.

Scanning electron microscopy (SEM) is probably the most diverse method for qualitative and quantitative analysis. It offers an insight into preferential attachment of bacteria, biofilm growth dynamics and the nature and 3D appearance of microbial biofilms due to the great depth of field. Quantitative observations involve counting the number of organisms over a given surface area, either manually by encircling or with the help of histogram exclusions on highly contrasted imager or by computer vision. SEM imaging allows bacteria counting on opaque or highly textured surfaces which are problematic with other methods. It has been used for bacteria counting on metals, ceramics, polymers, polyelectrolytes, and also directly on final products, such as intravascular and urethral catheters, corneas, kitchen appliances and others.

1.6.4.2 Indirect bacteria attachment determination methods

Indirect observation techniques include procedures that first detach the bacteria from the substrate and then count the detached organisms, and *in situ* procedures that count attached microorganisms by measuring a secondary attribute of the attached bacteria (radiolabelling, ELISA - Enzyme-linked immunosorbent assay, stained bacterial films, etc.). Plate count is a process where bacteria are enumerated indirectly by detaching the organisms and count the colony forming units. The procedure is straightforward and widely used as every colony will grow from single bacteria. The average size of the colony is around 1 mm^2 which sets the upper limit of the number of bacteria that can be observed on a given surface. Therefore, this method cannot be used for surfaces where bacterial coverage is extensive.

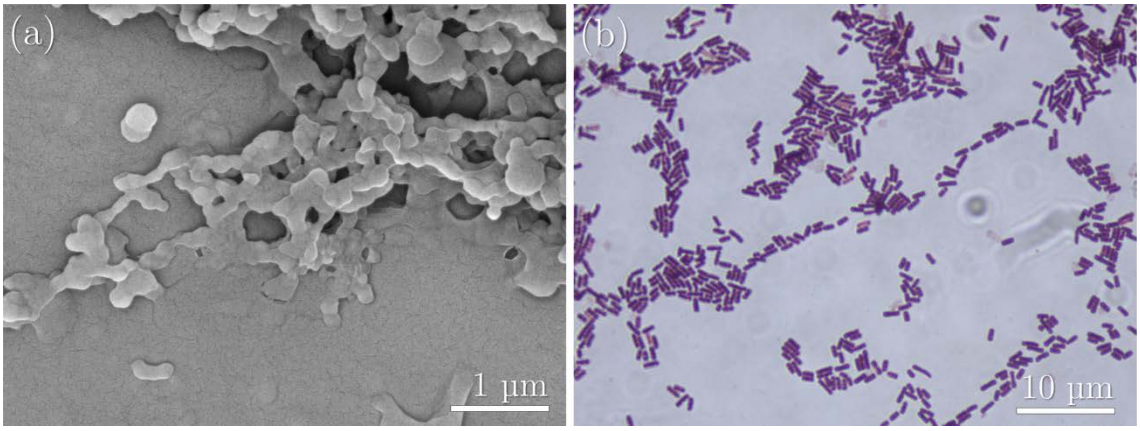


Figure 1.20: (a) direct observation of *Pseudomonas aeruginosa* by scanning electron microscopy and (b) optical microscopy micrograph of in-direct Gram staining by crystal violet.

Chapter 2

Aims and Hypothesis

In my thesis I propose a different approach to the immobilisation of nanoparticles and surface treatment using one-step hydrothermal synthesis. Precursor addition is generally essential for the hydrothermal process and commonly a soluble nitrate or acetate is used in the case of zinc and aluminium. I propose an introduction of the substrate directly to the autoclave, providing precursors due to ionic exchange of metal ions to the solution and a substrate that facilitates heterogeneous nucleation on the surface. Initial oxide corrosion barrier can therefore be expanded with a range of functionalised metal oxides that can be synthesised hydrothermally at temperatures below 200 °C.

I hypothesise that a one-step synthesis path to functionalised surface is achievable by carefully introducing new precursors for either base metal or for a different oxide, adjusting the hydrothermal treatment parameters, such as temperature, pressure (by filling of the autoclave), pH and addition of surface tension agents (surfactants, etc.).

Zinc oxide is a semiconductor material itself and is susceptible to photo-induced effect. Because it can easily crystallise in many different morphologies, it is a suitable base substrate for producing superhydrophobic surfaces. Another oxide with a wide array of applications is TiO_2. It can be prepared with rather simple sol-gel and hydrothermal procedures and exhibits both photocatalytic and superhydrophilic properties when nano TiO_2 is irradiated by UV light.

I hypothesise that better adhesion for hydrothermally grown coatings can be achieved comparably to spin or dip-coated ones due to direct growth from the substrate without a need for calcination at higher temperatures. One-step hydrothermal treatment also provides an economic method which is easy to scale-up for final treatment of base metals that are prone to forming oxides on their surface. A three-layer structure, composed of aluminium/boehmite/titanium dioxide, is a promising structure for immobilisation of titania nanoparticles. Surfaces with immobilised photocatalyst have an advantage over batch-style reactors which could cause secondary pollution by TiO_2 waste.

The study of aluminium/TiO_2 system by electron microscopy helps us understand the interaction between titania and aluminium oxide and hydroxide, their growth mechanism and follow how morphological changes influence their interaction and influence photocatalytic efficiency of the system.

In order to prepare superhydrophobic coating, a substrate with increased roughness is necessary. Due to the variety of morphologies ZnO can exhibit, I hypothesise that suitable surface morphology can be achieved by hydrothermal treatment of zinc. Superhydrophobic coatings are self-cleaning and can potential be highly bacteriostatic.

Our work has been carried out within a joint project J2-4309, together with IMPOL d.o.o. from Slovenska Bistrica, an aluminium producer, and Cinkarna Celje, d.d. as a producer of zinc sheets and macro- and nano-sized TiO_2. The project aim was to

research and evaluate the processes for the preparation of functionalised metals with novel properties, such as photocatalytic cleaning under UV, self-cleaning properties by influencing contact angle characteristics and the improvement in dielectric response.

Chapter 3

Materials and Methods

3.1 Processing and Sample Preparation

3.1.1 Chemicals and Materials

Substrate metal materials were obtained from our industrial partners in the project, Cinkarna Celje and IMPOL (Slovenska Bistrica). Aluminium AA 3105 (M 13) with elementary composition AlSi0.2Fe0.59Cu0.04Mn0.39Mg0.36 and zinc (≥99%) sheets were obtained and cut into circles with 14 mm diameter. The thickness of aluminium and zinc samples was 1 mm. Samples were cleaned and sonicated in acetone and dried at 90 °C. AISI 304 stainless steel was used for the preparation of the surfaces with different roughness. The chemicals used in the study were used without further purification.

Precursors:

- Titanium(IV) isopropoxide (TTIP), $Ti[OCH(CH_3)_2]_4$, 97%, Sigma-Aldrich
- Titanium(IV) butoxide (TBT), $Ti[O(CH_2)_3CH_3]_4$, ≥99%, Alfa Aesar
- Titanium tetrachloride, $TiCl_4$, 99.9%, ACROS Organics
- TiO_2 P 25, ≥99.5%, Degussa
- Zinc nitrate hexahydrate, $Zn(NO_3)_2 \cdot 6H_2O$, 99%, Alfa Aesar
- Zinc acetate dihydrate, $Zn(CH_3COO)_2 \cdot 2H_2O$, 98+%, Alfa Aesar

Other chemicals:

- Tetramethylammonium hydroxide (TMAH), $N(CH_3)_4^+ OH^-$, 25% in H_2O, Merck
- Nitric acid, HNO_3, Sigma-Aldrich 90%
- Acetic acid, CH_3COOH, Merck, 33%
- Fluoroalkyl oligosiloxane (FAS), Dynasylan F 8815, Evonik
- 1,6-Diaminohexane (DAH), $C_6H_{16}N_2$, Merck 99%
- 1,3-Diaminopropane (DAP), $C_3H_{10}N_2$, Merck 99%
- Hydrofluoric acid, HF, 48 wt. % in H_2O, ≥99.99%, Sigma–Aldrich
- Caffeine, 99.0% HPLC grade, Sigma–Aldrich
- Phosphate buffer saline (PBS, Oxoid, UK)
- Dimethylbenzene (xylene, Kemika, Zagreb)
- Isopropyl alcohol (IPA), C_3H_7OH, Carlo Erba Reagents
- Ethanol (EtOH), C_2H_5OH, absolute, anhydrous, Carlo Erba Reagents

3.1.2 Sol preparation

Sols, based on different ratios of ethanol, isopropyl alcohol and deionised water, were prepared by the addition of a precursor. The rate of hydrolysis was controlled by the water content. The total volume of the solution was 50 ml. Samples were first sonicated and then placed in the centrifuge to separate the desired dissolute from residual organic compounds. The process of separating the clear solution from the residue and the addition of fresh medium was repeated until the electrical conduction of a solution was stable, indicating no remaining dissociated organics. Hydrolysed precursor was added to the desired medium in a beaker and pH was adjusted accordingly by the addition of either diluted TMAH or nitric acid, depending on desired conditions. Lastly, capping agents HF, DAH and DAP were introduced, depending on the system.

3.1.3 Hydro- and solvothermal conditions

General-purpose autoclave with steel framework and Teflon (polytetrafluoroethylene) vessel was used. Due to the introduction of metallic substrates, a special holder was made out of Teflon to fix samples in the vertical position. When the samples were placed directly on the bottom, the coating formed only on the topside. Teflon has a melting point at 327 °C but starts decomposing and emitting dangerous fluorocarbon gases at temperatures above 250 °C. I decided to limit the top synthesis temperature at 200 °C due to safety reasons. Autoclaves were heated in an oven and cooled naturally to room temperature. After the treatment, samples were rinsed with deionised water and ethanol and dried at 75 °C for 10 hours. Powder was extracted from the residue that did not bind on the surface. Residue was spread on the petri dish and dried at 75 °C for 10 hours before it was milled into powder.

3.1.4 Other pre- and post-treatment processes

3.1.4.1 Dip-coating and annealing

Dip-coating technique was used to apply 10% FAS solution on the coated zinc surface. The solution was placed in a beaker and continuously stirred for 10 min. Samples were manually immersed for 10 seconds and slowly lifted from the solution. FAS cross-linking and binding to the surface was achieved by placing samples in a pre-heated oven at 150 °C for 5 min. The reaction mechanism is described with Equations (3.1), (3.2) and (3.3) and illustrated in Figure 3.1. The primary mechanism for film formation and surface binding is oxygen bridge formation (Si-O-Si and Si-O-surface) by means of polycondensation. This forms a uniform coating on the surface with Si-O-Si chains giving it structural support and outward pointing hydrophobic tails [103].

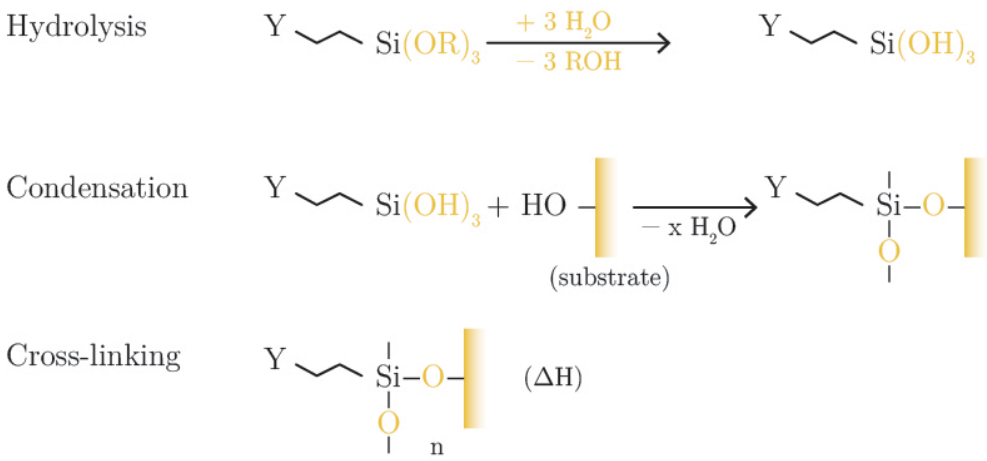


Figure 3.1: Three-step process of hydrophobic coating attachment to the surface. After initial hydrolysis, silane undergoes polycondensation that bridges Si sites between each other with oxygen bridges as well as cross-linking Si sites to the surface.

$$\mathrm{Si(OR)_n + nH_2O \rightarrow Si(OR)_{4\text{-}n}(OH)_n + nROH\ (Hydrolysis)} \tag{3.1}$$

$$\mathrm{Si\text{-}OR + HO\text{-}Si \rightarrow Si\text{-}O\text{-}Si + ROH\ (Condensation + alcohol)} \tag{3.2}$$

$$\mathrm{Si\text{-}OH + HO\text{-}Si \rightarrow Si\text{-}O\text{-}Si + H_2O\ (Condensation + water)} \tag{3.3}$$

3.1.4.2 Abrasion treatment

For bacteria adhesion tests on metallic surfaces, a set of samples with a different roughness was prepared. Electropolished AISI 304 stainless steel was used as a starting material. 3D polishing is a process based on laser polishing by remelting. Grinding is an abrasive machining process in which a spinning wheel covered in rough particles cuts chips of material from metallic substances. Electropolishing is an electrolytic polishing technique in which the metal (anode) on the surface is oxidized and dissolved in the electrolyte. Brushing is polishing with a grit belt and then softening with a grit greaseless compound. A pattern of very fine lines parallel to the brushing direction is obtained. 1x1 cm samples were cut for adhesion and surface investigations.

3.1.4.3 Surface plasma treatment

In order to obtain hydrophilic stainless steel samples for bacteria adhesion tests, surface treatment with Ar and Ar/O_2 plasma was used. Plasma cleaning effect is two-fold: it cleans the surface of any residual organic stains and also increases the presence of hydroxyl groups, resulting in hydrophilic surface. Relaxation time for AISI 304 samples was approximately 3 hours. Solarus Advanced Plasma Cleaning System, model 950 (GATAN Inc., Pleasanton, CA, USA) was used for this process.

3.2 Characterisation

3.2.1 X-ray powder diffraction (XRD) and low-angle Empyrean XRD

The phase composition and crystallinity of the samples were analysed using an X-ray diffractometer (XRD, PANalytical X'Pert PRO, $CuKa_{\alpha 1}$ = 1.5406 Å). Penetration depth of X-rays is affected by the absorption coefficient (μ) of the sample and the incident angle of the X-ray beam (α). The intensity of monoenergetic beam penetrating a layer of material with mass thickness t and density ρ emerges with intensity I given by the exponential attenuation law (Eq. (3.4)) and can be rewritten as Equation (3.5) to define mass absorption coefficient (μ/ρ).

$$\frac{I}{I_0} = e^{-(\frac{\mu}{\rho})t} \tag{3.4}$$

$$\frac{\mu}{\rho} = \ t^{-1}\ln(\frac{I}{I_0}) \tag{3.5}$$

Penetration depth $\tau_{1/e}$ and information depth τ which includes the weighted average of a sampling depth are defined as Equations (3.6) and (3.7), respectively [104].

$$\tau_{1/e} = \frac{sin(\alpha)}{\mu} \tag{3.6}$$

$$\mu = \frac{1}{\mu k_\alpha} + \frac{1}{1 - e^{\mu t k_\alpha}} \tag{3.7}$$

A low-angle XRD method (PANalytical Empyrean Multi-Function XRD, $CuKa_{\alpha 1}$ = 1.5406 Å) was used for the characterisation of nano-coatings.

3.2.2 Surface metrology (AFM, Profilometer)

Roughness and surface topography were determined by Atomic force microscope VEECO Dimension 3100 (AFM) in contact mode and a mechanical profilometer Form Talysurf Series 2 from Taylor-Hobson Ltd., Leicester, Great Britain. Arithmetic average of absolute values (R_a) and root mean square (R_q, R_{RMS}) methods were used to quantify the raw data from either method (Eq. (3.8) and (3.9), respectively). Gaussian filter cut-off values of either 0.8 or 0.25 mm were used according to ISO 4288-1996 standard.

$$R_a = \frac{1}{n}\sum_{i=1}^{n}|y_i| \tag{3.8}$$

$$R_q = \sqrt{\frac{1}{n}\sum_{i=1}^{n} y_i^2} \tag{3.9}$$

AFM offers surface characterisation on submicron scale along with the possibility of imaging surfaces with high resolution. Quantitative evaluation of selected surface features including statistical analysis helps to determine roughness parameters on the submicron scale. AFM scanning is ideal for very flat substrates where the difference between the highest and lowest point is fairly small. It is because of this that roughness measurements on larger areas (10 µm^2 and above) are impractical on the AFM.

Profilometer has the resolution of 3 nm in z-direction but only 1 µm in lateral directions. It allows for large area/line scanning for better statistics and determination of surface waviness along with surface roughness. Mechanical profilometer can sample surfaces of 1 mm^2 and above with ease as well as overcome bigger fluctuations in surface height.

3.2.3 Scanning electron microscopy (SEM) and FIB

Scanning electron microscopy was used to characterise the morphology and elementary composition of coated samples. The specimens for the SEM observations were fixed on the holder by an adhesive carbon conductive tape and coated with 2 nm thick carbon layer to ensure good electrical conductivity and electron discharge of the specimens under electron beam.

For standard observations, a scanning electron microscope (Jeol JSM-7600F, Jeol Ltd., Tokyo, Japan) with thermal filed-emission gun (FEG) and in-lens secondary electron detector (SEI), lower secondary electron detector (LEI), backscattered electron detector (BE) and energy-dispersive X-ray spectrometer (EDXS, X-MAX, Oxford Instruments, Oxfordshire, UK). Electron micrographs were obtained using SEI, LEI and BE detectors at accelerating voltages from 5–15 kV and working distances 2–15 mm.

To determine the thickness of each layer, focused ion beam (SEM-FIB, dual-beam FEI Helios Nanolab 650 focused ion beam) was used to perform a cross-section. The specimen was tilted to an angle of 52° and material was eroded using 30 keV Ga ions. By imaging the specimen at that angle I got a side view, where different layers were observed. Actual thickness (t) was calculated by (3.10), where t_m is the measured thickness on the micrograph and β is the tilt angle of the specimen.

$$t = t_m \cos(\beta)^{-1} \tag{3.10}$$

EDXS point analysis was done without the use of standards. Aluminium and titanium have distinct peaks to evaluate the presence of the specific element at certain parts of the sample. Exact structural information of crystalline phases was determined with XRD beforehand.

Samples for bacteria counting were coated with gold instead of carbon. In order to preserve the bacteria condition, substrates could not be extensively washed. Carbon coating on unclean surfaces often peels off in a form of a film and is therefore unsuitable for this application. A thin layer of gold (7 nm) was applied on the samples with GATAN Model 682 PECS system (Precision Ion Etching and Coating System, GATAN Inc., Pleasanton, CA, USA) to achieve good electron discharge. Quantitative analysis was made with visual assessment of bacterial adhesion on different substrates. For quantitative analysis, the choice of method depends on the type of micrograph. In cases where backscattered electrons were imaged I could achieve a contrast based on atomic Z-values if the substrate was not carbon-based. With high contrast between bacteria and the substrate, coverage can be determined by exclusion via histogram. When this method was not feasible, I manually encircled bacteria on the micrographs and

converted images to binary form. For editing and measuring the fraction of the surface covered with bacteria, I used ImageJ software package (Version 1.50b, 2015, Wayne Rasband, National Institutes of Health, Bethesda, MD, USA). Several images, representing a total area of 500 µm^2 per sample, taken at different sample positions, were analysed.

3.2.4 Transmission electron microscopy (TEM)

In order to study the interactions between different layers (aluminium, boehmite, TiO_2), we used two transmission electron microscopes:

- Jeol JEM-2010F TEM/STEM with field emission gun, Jeol Ltd., Tokyo, Japan, operating at 200 kV and equipped with Si(Li) EDXS detector (Link ISIS, Oxford Instruments, Oxfordshire, UK), CCD camera (Orius SC1000C, Gatan Inc., Pleasanton, USA), bright-field (BF), dark-field (DF) and high-angle annular dark-field detector (HAADF).
- Jeol ARM 200 CF TEM/STEM with cold field emission gun, Jeol Ltd., Tokyo, Japan, operating at 80-200 kV and equipped with high-angle annular dark-field detector (HAADF), annular bright-field (ABF) and Dual EELS system Quantum ER from Gatan and Jeol Centurio 100 mm^2 EDXS system with SDD detector.

Powder samples for TEM observation were prepared by dispersion of nanoparticles in ethanol and sonication to achieve deagglomeration. A drop of well-dispersed suspension was placed on the lacy carbon-coated copper grid and dried in a vacuum chamber overnight.

Cross-section samples were prepared by tripod polishing and additional ion-milling. To avoid potential damage caused by ion-milling, specimens were prepared by the mechanical tripod polishing method using an automatic tripod polisher (Allied Multiprep System). The specimens were cut into slabs (1.5 mm wide and 2 mm long) and attached to a Pyrex specimen holder using Crystal Bond thermoplastic wax. The specimen was first polished using a diamond-lapping film (DLF) with 9-µm grain size to provide a planar surface. For further polishing DLFs with grain sizes of 3, 1, 0.5, and 0.1 µm were used. The final polishing step was done on a polyurethane cloth using a silica solution with 50-nm sized particles (Allied Colloidal Silica Suspension) in order to avoid wedge chipping and scratches on the polished surface. Prior to polishing the opposite side, the sample was removed from the Pyrex holder by heating the polishing block on a hot plate. Then the specimen was turned upside down and glued onto the Pyrex specimen holder again. The specimen was thinned down to a thickness of 180 µm using a 9-µm DLF. A wedge angle of 5° was introduced, which makes the specimen more robust to handle. The specimens were further polished down to thicknesses of 70, 50, 30, 10 µm using 6-, 3-, 1- µm DLFs, respectively. Subsequently, final polishing was performed with 0.5-µm DLF and 50-nm colloidal silica to thin the sample to electron transparency [105]. The samples were then glued on 3 mm Mo support half-grid. The wedge-shaped specimens were additionally cleaned and Ar ion-beam thinned in a precision ion polishing system (PIPS, Gatan, Inc., USA) at 3.0 keV for 30 min, 2 keV for 15 min, 1.4 keV for 10 min and at 0.6 kev for 10 min. During the ion-milling process the specimens were cooled using liquid nitrogen (L-N_2).

Observation of oxide-hydroxide coating on aluminium proved to be difficult as it is very unstable and degrades rapidly under electron beam irradiation. Lower accelerating voltages (80kV) and specimen cooling stage (GATAN Double-tilt liquid nitrogen cooling

holder, model 636) were used to minimise the impact of beam exposure to the sample. BF and ABF imaging was used for morphological studies while EDXS and energy-filtered transmission electron microscopy (EFTEM) provided the chemical analysis and elemental mapping.

3.2.5 Dielectric measurements

Dielectric measurements were done on oxidised aluminium thin foil, used in the assembly of foil capacitors (Iskra, d.d. PE Kondenzatorji Semič). Surfaces of the samples were covered with sputtered electrodes (100 nm of gold on 10nm of chromium for better adhesion). The complex dielectric constant $\varepsilon^*(\omega, T) = \varepsilon' - i\varepsilon''$ was measured using a Novocontrol Alpha High Resolution Dielectric Analyzer in the frequency range 300 Hz–1 MHz, using the amplitude of the applied electric ac signal, equal to 100 mV. The real part of the complex ac conductivity $\sigma^* = \sigma' - i\sigma''$ was calculated via $\sigma' = 2\pi\nu\varepsilon_0\varepsilon''$ $\sigma' = 2\pi\nu\varepsilon_0\varepsilon''$ with ε_0 being the permittivity of free space, ν being the frequency and ε'' a complex part of dielectric constant, both experimentally obtained. After heating the samples up to 420 K, the dielectric response was detected during cooling runs with a rate of -0.75 K/min. The temperature of the samples was stabilized to within ±0.01 K using the lock-in bridge technique with a Pt100 platinum resistor as the thermometer. For an ideal sample, the measuring setup can be described as a system of capacitor (with capacitance C) and resistor (with resistance G) in parallel (Figure 3.2). Impedance of such a system is described in Equations (3.11) and (3.12) where capacitance (C_0) is defined with permittivity of free space and geometrical factor as $C_0 = \varepsilon_0(S/d)$ and real and complex part of dielectric constant (ε' and ε'') defined as $\varepsilon' = C/C_0$ and $\varepsilon'' = G/(\omega C_0)$.

$$Z^{-1} = R^{-1} + i\omega C = G + i\omega C \tag{3.11}$$

$$Z^{-1} = i\omega C_0\varepsilon^* = i\omega C_0(\varepsilon' - i\varepsilon'') \tag{3.12}$$

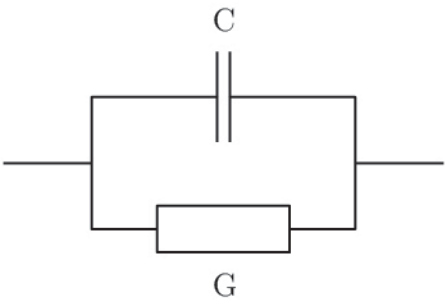


Figure 3.2: Schematic of measuring setup equivalent: capacitor (C) and resistor (G) in parallel.

3.2.6 Photocatalytic measurements

Photodegradation of organics on photocatalytic TiO_2 was measured with caffeine as a model molecule. Caffeine was used as an indicator for photocatalytic activity because the

mechanism of its degradation is well known and UV/VIS spectra of degradation products do not overlap with the main caffeine peak. A petri dish with 5 ml of 10 ppm caffeine solution was prepared. A magnetic stirrer and coated aluminium disc were placed side by side in the solution. The prepared sample was left for 30 min in the sterilizer (no UV) before it was sampled. After the sunlight simulating light was turned on, the solution was measured in hourly intervals and analysed in UV/VIS spectrophotometer (PerkinElmer Lambda 950) in 220–350 nm range. Lamps used in my experiments were OSRAM ULTRA-VITALUX Ultraviolet high-pressure lamps (white light emulating natural sunlight) in the ambient chamber and LED UV 365 nm for smaller reactor applications. Spectral distribution of both lamps was measured by spectrometer (Figure 3.3).

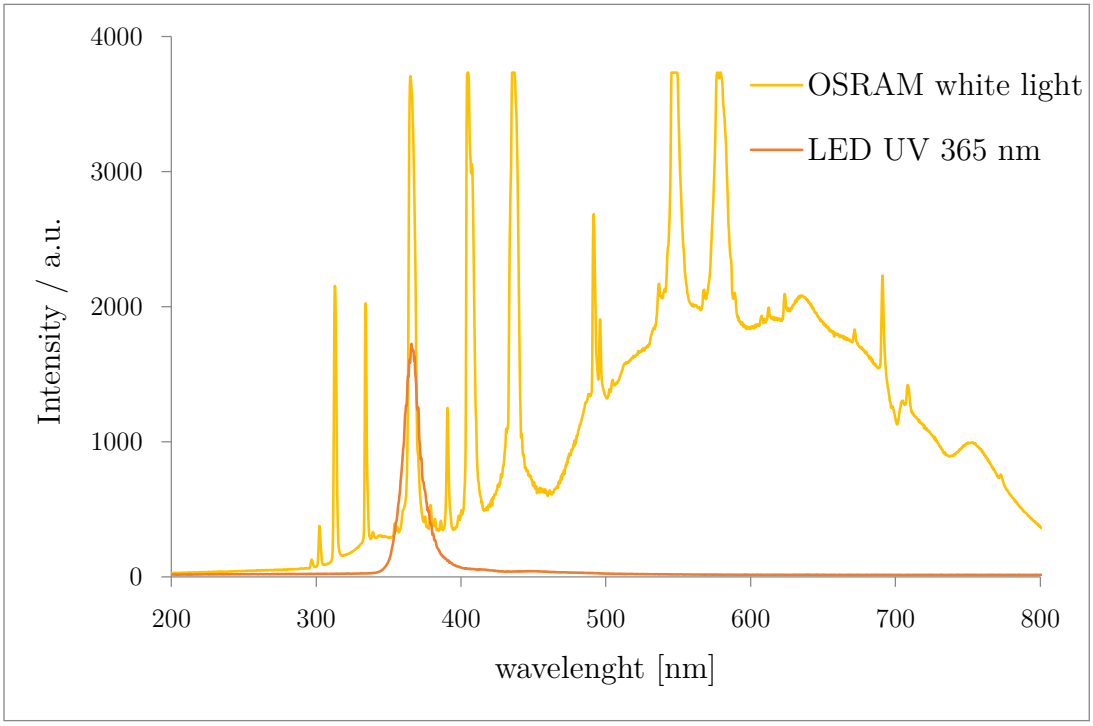


Figure 3.3: Spectral intensity of the two lights I used for photocatalytic degradation measurements: OSRAM ULTRA-VITALUX Ultraviolet high-pressure lamps light and LED UV 365 nm.

In order to avoid reaction volume deviation by batch sampling and study the possibilities of continuous flow applications, a reactor cell from UV-transparent acrylic glass (PMMA) was constructed, as presented in Figure 3.4. A set of four 1.2 mW/cm^2 UV LEDs (365 nm) combined with a power controller on a small printed-circuit board were used to illuminate the reactor at the optimal position (3 mm above the sample). Sampling caffeine solutions of different concentrations (10–50 ppm) were used. Peristaltic pump was used to move the solution around the system (Figure 3.5) in pulses, through the reactor and UV/VIS spectrometer, where it was sampled in 5 min intervals.

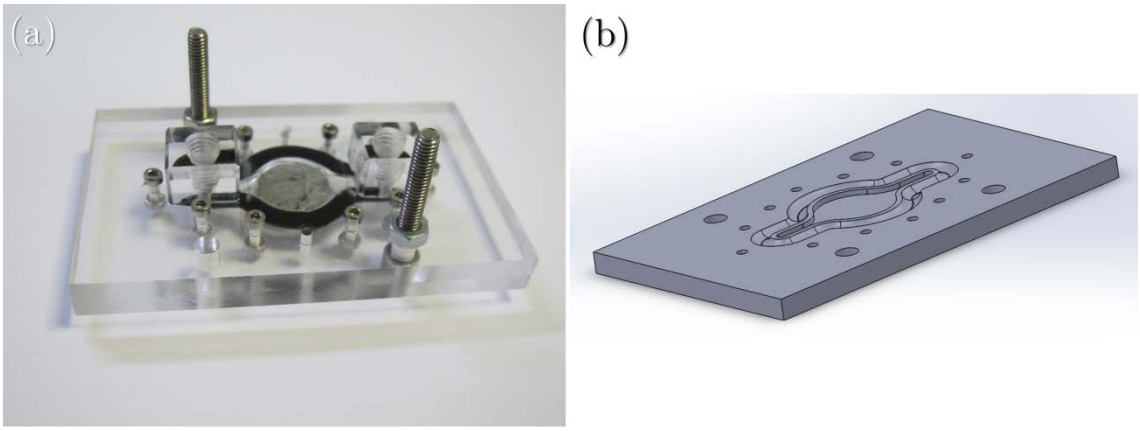


Figure 3.4: (a) Assembled reactor with the aluminium sample and (b) 3D model of the bottom halve.

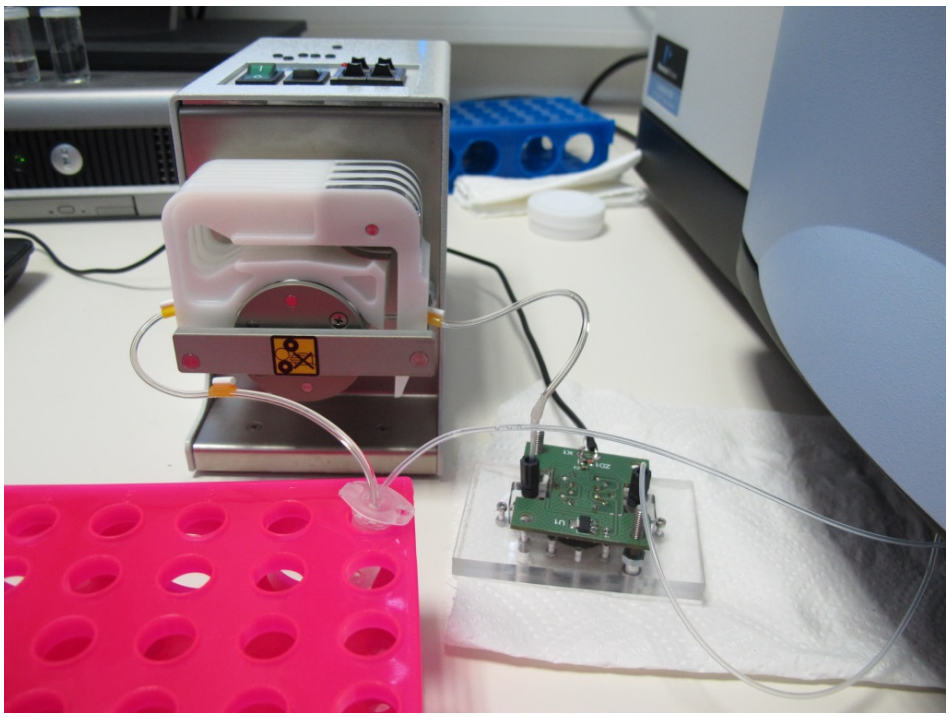


Figure 3.5: Reactor system with peristaltic pump, reactor with UV LED array, UV/VIS spectrometer and small reservoir.

3.2.7 Contact angle and hydrophobicity measurements

A Theta Light Optical Tensiometer (Attension, Stockholm, Sweden) was used for the determination of the contact angle between a drop of water and the substrate. The tensiometer consists of a light source, a camera, a liquid dispenser, and a sample stage where the substrate is placed. A small drop of water was placed on the substrate using a dispenser, and an image of the profile of the drop was taken by means of a digital camera and a light source at the opposite side of the drop. The angle between the substrate and the drop is determined from the image by fitting either a curve or a circle

to the droplet. The contact angle is a measure for the surface hydrophobicity/hydrophilicity. Droplets tend to disappear into the hygroscopic surfaces (such as filters) rapidly, thus sequential imaging was used to analyse conditions when the droplet hit the surface to obtain contact angle data.

Surface hydrophobicity of bacterial cells was determined with the procedure that included centrifugation of bacterial culture (2 ml) at 5000 rpm for 4 min, cell washing with phosphate buffer saline (PBS) 2 times, re-suspension of cells in 15 ml of PBS and measurement of absorption (A_0) with spectrophotometer (Tecan TIP, Mannedorf/Zuerich, Switzerland). Then 3.5 ml of bacterial suspension in PBS and 0.5 ml of xylene was mixed and agitated on Vortex at maximum speed of 2500 (twiddles) for 1 min. After two layers separation, absorption (A) of the aqueous phase was measured. The percentage of cells in xylene layer was calculated as % of Hydrophobicity by equation (3.13).

$$\%\ of\ hydrophobicity = \left(1 - \left(\frac{A}{Ao}\right)\right) \times\ 100 \tag{3.13}$$

3.2.8 Bacteria counting for adhesion determination

Bacteria count was done directly using SEM and indirectly by crystal violet (CV) assay. A method described by *Peeters et al.* [106] was used with minor modifications. 20 sterile disks per sample type were aseptically transferred to a fresh sterile Petri dish and inoculated in 3 ml overnight bacterial culture in TSB (tryptic soy broth) with the desired cell concentration (10^6–10^7 CFU/ml). A control set of 20 disks was placed in a Petri dish with 3 ml of fresh TSB. Incubation times were 48 h at 25 °C for *L. monocytogenes* and *B. cereus* for 24 h at 37 °C and other bacteria (*S. aureus*, *P. aeruginosa*, *S. typhimurium* and *E. coli*). After the incubation, the supernatant that contained non-adhered cells was removed by rinsing the Petri dish three times with sterile distilled water. Samples were dried at 60 °C for 10 min before 1.5 ml crystal violet (CV, Merck) solution (0.5 and 1%) was added. CV was removed after 15 min by repetitive rinsing and dried afterwards. Samples were transferred to a microtiter plate. Bound CV was released by adding 100 µl of absolute ethanol for Gram negative or acetic acid for Gram positive bacteria. The absorbance was measured at 584 nm and 620 nm on Tecan (TIP, Zürich, Switzerland). The average absorbance as a measure for strain adhesion was calculated by Equation (3.14) [107].

$$\Delta\bar{A} = \sum_{i=1}^{n} \frac{(A - \overline{A}_0)}{n} \tag{3.14}$$

Chapter 4

Results and Discussion

4.1 Aluminium

4.1.1 Structural and morphological properties

Aluminium samples were rinsed with acetone and sonicated before further treatment in order to remove organics and stains caused by the manufacturing process from the surface. Deionised water (dH_2O), ethanol and isopropyl alcohol were used as solvents for hydrothermal treatment. Before hydrothermal experiments, samples were placed in beakers with each of the solvents and left at ambient conditions for 24 h to evaluate the passive oxidation of the surface in a timeframe I will be using for hydrothermal treatment. SEM micrographs of the samples, along with the untreated one, are shown on Figure 4.1. Partial oxide formation can be observed on the sample, immersed in deionised water, in a form of small oxide clusters on the surface. No changes were observed on the samples in ethanol and isopropyl alcohol.

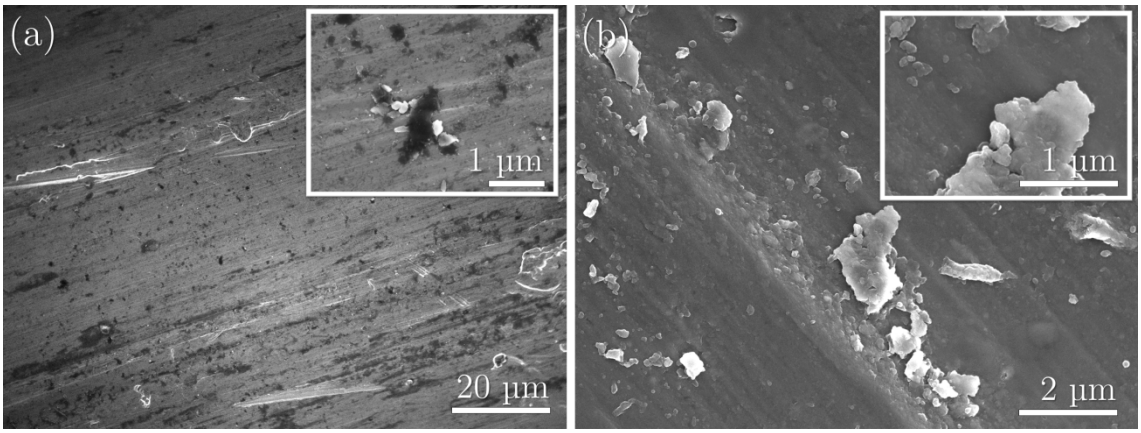


Figure 4.1: SE-SEM micrographs of (a) untreated aluminium surface and (b) aluminium sample after 24 h in dH_2O. Both samples still exhibit abrasions on the surface that are a consequence of mechanical deformation during rolling of the sheets. The formation of hydroxide particles can be observed in the inset of the treated sample.

Hydrothermal parameters that were used in my experiments are listed in Table 4.1. Synthesis temperatures varied between 120 and 200 °C with times up to 62 hours. pH of the initial solution was adjusted either with TMAH or nitric acid. Additional agents were added in order to promote the bipyramidal growth along with precursors for

Ti^{4+} ions. Filling ratio of the autoclave was always ~50% so reaction pressure was a function of temperature and type of solvent.

Table 4.1: Parameters for hydro- and solvothermal treatment of aluminium in deionised water, ethanol and isopropyl alcohol.

type	temperature	time	solvent	pH	precursor	additives
hydrothermal	120–200 °C	3–62 h	dH_2O	3–10	TTIP, TBT	HF
solvothermal	120–150 °C	12 h	EtOH	7.33	TTIP	–
solvothermal	120–200 °C	12 h	IPA	5.5	TTIP	–

4.1.1.1 Hydro and solvothermally treated aluminium

Boehmite coating evolution with the increasing temperature can be observed on XRD diffractogram in Figure 4.2. The increase in boehmite peaks at 2Θ 14.49° for (020), 28.21° for (120) and 49.3° for (200) (ICSD 21-1307) indicates the increase in thickness of the coating on aluminium substrate (ICSD 01-089-4037) with the increase in synthesis temperature from 150 °C to 200 °C. Thickness of the boehmite coating was measured from the SEM micrographs of the cross-section sample, prepared for TEM analysis. Figure 4.3 shows the top-down view of one side of the sample, with three distinct layers: aluminium, boehmite and epoxy resin. Thickness of the boehmite layer was 1.5–2 µm and was uniform over the whole section.

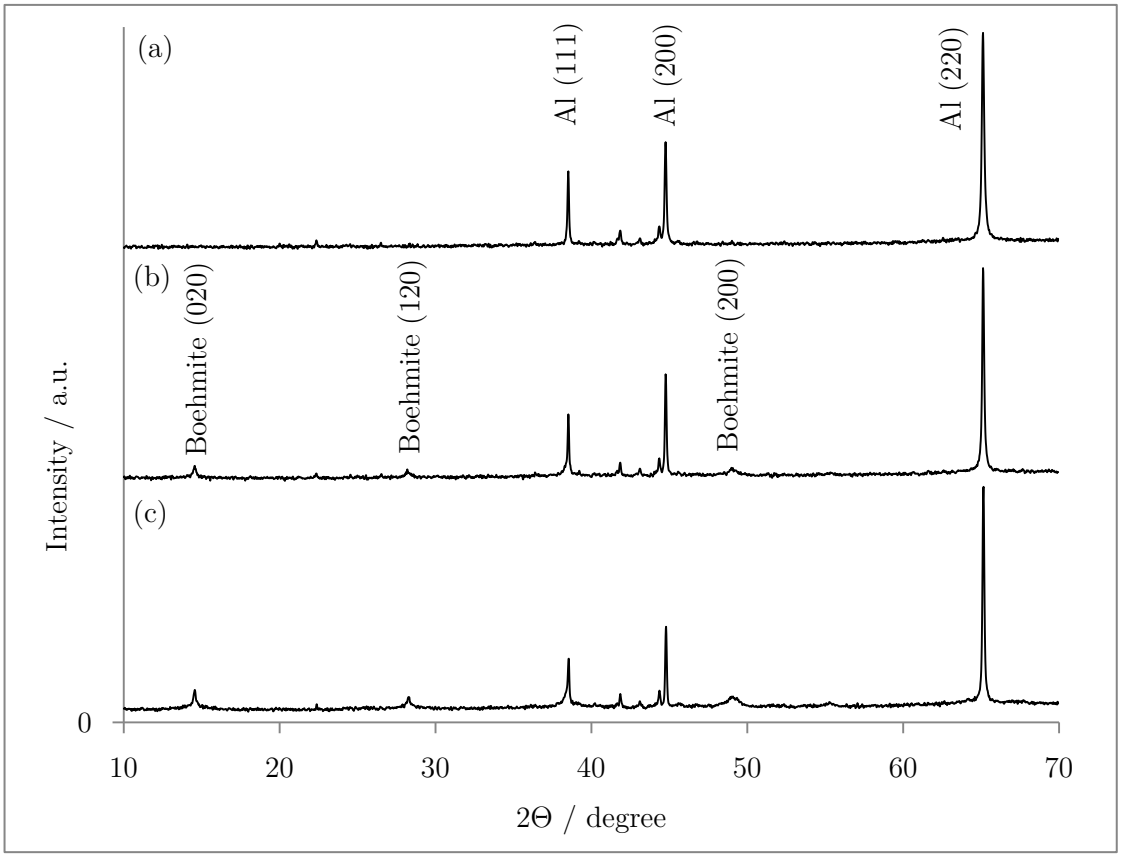


Figure 4.2: XRD diffractogram of boehmite layers on substrates: (a) untreated aluminium sample, (b) hydrothermally treated aluminium substrate at 150 °C / 12 h without Ti precursor and (c) hydrothermally treated aluminium substrate at 200 °C / 12 h without Ti precursor. The appearance and increase of boehmite peaks at 14.49°, 28.21° and 49.3° indicates the presence and increase in the thickness of boehmite layer with the increase of synthesis temperature from 150 °C to 200 °C.

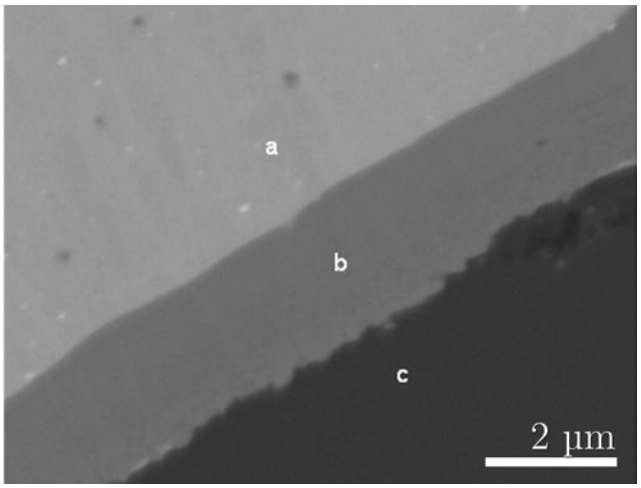


Figure 4.3: BE-SEM micrograph of cross-section aluminium substrate with boehmite coating, hydrothermally prepared at 200 °C / 12 h with TTIP precursor. (a) Aluminium substrate, (b) 1.75 µm thick boehmite layer and (c) epoxy resin.

SEM analysis showed the formation of small clusters of aluminium oxide hydroxide (boehmite, γ-AlO(OH)) on the surface at 120 °C / 12 h which confirms XRD results (Figure 4.2). Synthesis in ethanol with TTIP yielded small, globular, 20–50 nm wide amorphous particles. Samples in pure ethanol remained unchanged. Surface that was hydrothermally treated in isopropyl alcohol remained unchanged. Figure 4.4 shows the influence of the solvent on the surface morphology at 150 °C.

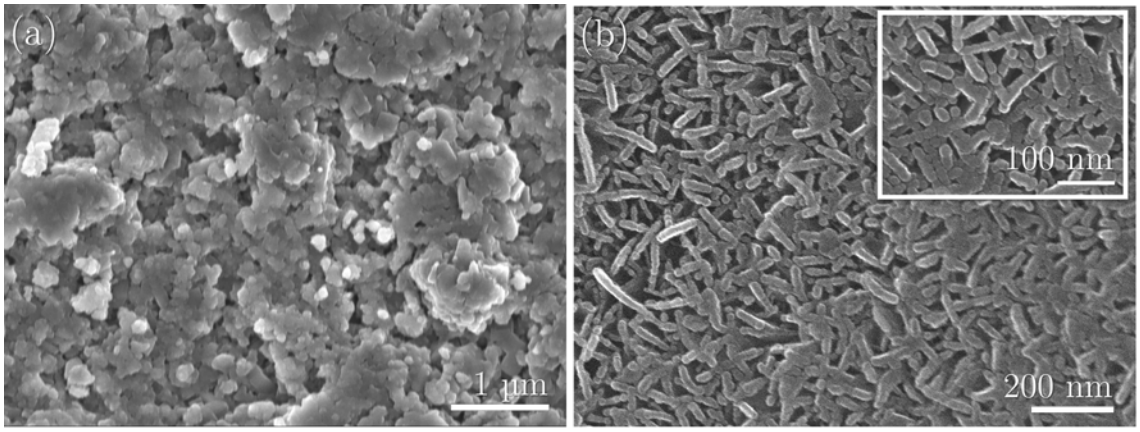


Figure 4.4: SEM micrographs of (a) hydrothermally treated aluminium surface at 150 °C / 12h without Ti precursors. Sub-micron boehmite crystal clusters form nonhomogeneously over the surface and (b) aluminium sample treated in abs. ethanol at 150 °C / 12 h with TTIP. Formations are amorphous.

Further increase in the temperature to 200 °C provided a driving force to cover the whole surface with boehmite on the sample in deionised water. Coating consists of homogenously distributed blocky boehmite crystals that are approximately 200 nm wide without visible defects. The sample in isopropyl alcohol was evenly covered with still amorphous coating of aluminium oxide/hydroxide with particle size between 100 and 200 nm (Figure 4.5) and EDXS analysis showed traces of titanium but no new crystallised phase was observed. The presence of water is therefore crucial for promotion of aluminium ion exchange and crystallisation on the surface as oxide/hydroxide.

Ethanol has a tendency to react with aluminium at temperatures close to the boiling point of ethanol (78.37 °C) in a totally dehydrated environment, according to *Vargel et al.* [108]. The protective surface oxide coating of the aluminium is attacked by dehydrated alcohols and forms aluminium alkoxides, $Al(RO)_3$. Example reaction with ethanol is described in Equation (4.1). Aluminium triethoxide is hygroscopic and will likely decompose into aluminium hydroxide and ethanol after it absorbs moisture.

$$6C_2H_5OH + 2Al \rightarrow 3H_2 + 2Al(C_2H_5O)_3 \tag{4.1}$$

Samples in ethanol that were treated above 150 °C all completely decomposed into black residue and were discarded from future studies.

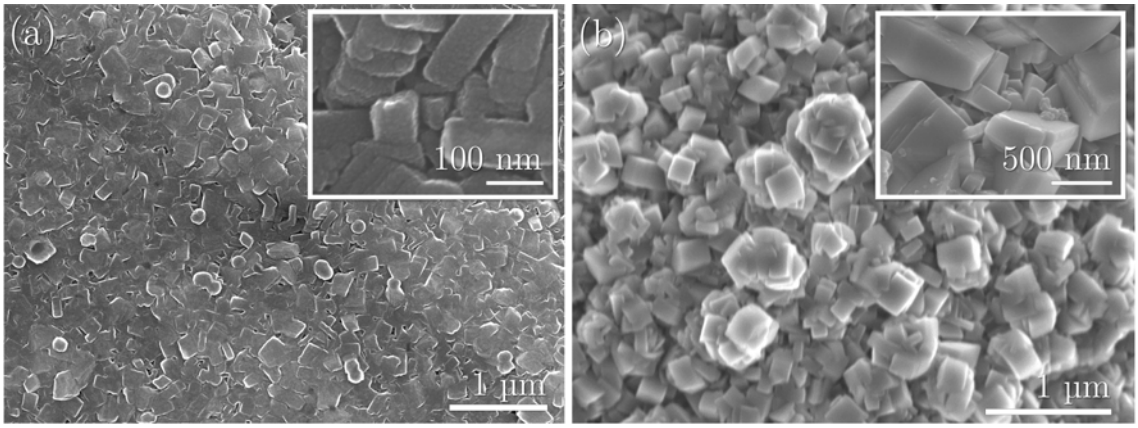


Figure 4.5: (a) SEM micrographs of solvothermally treated aluminium in isopropyl alcohol at 200 °C / 12h with TTIP. EDXS confirms the presence of titanium but no new crystallised phase was observed. (b) Aluminium sample, prepared in deionised water at 200 °C / 12h without Ti precursor. Blocky boehmite crystals are covering the whole surface.

4.1.1.2 Addition of titanium precursor to HT of aluminium

The addition of titanium precursor into the aqueous starting solution leads to the precipitation of TiO_2 particles under favourable hydrothermal conditions. Titanium(IV) isopropoxide (TTIP) and Titanium(IV) butoxide (TBT) aqueous solutions in the ratio 1:9 were prepared. The results of the synthesis with TTIP at 200 °C / 12h with no pH modifications and no additives are similar to the synthesis without the precursor. Thickness of the boehmite coating remains unchanged. Boehmite crystals are blocky with flat surfaces when prepared without TTIP but form more elongated crystals with visible planar defects when prepared with TTIP (Figure 4.6). Prolonged synthesis times up to 48 hours have a minor effect on the thickness of the coating and the size of the boehmite crystals is increased from 1 µm to 1.2–1.3 µm. EDXS analysis confirms the presence of titanium on the substrate but no TiO_2 nanoparticles were observed on SEM micrographs. This indicates that the incorporation of titanium in boehmite crystals is more favourable than TiO_2 crystallisation. Planar defect in the boehmite was further investigated with TEM.

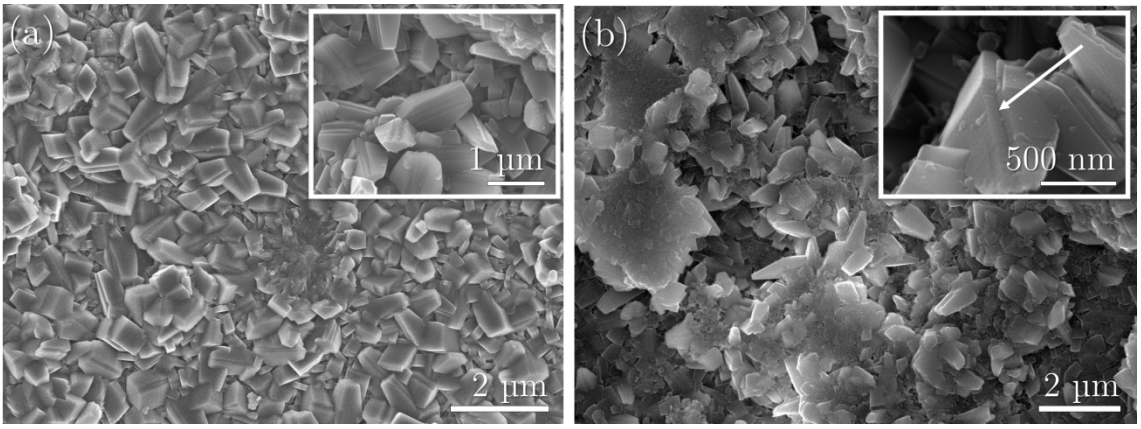


Figure 4.6: (a) Boehmite crystals with planar defects on hydrothermally treated aluminium samples at 200 °C / 12h with TTIP and (b) prolonged synthesis to 48 hours at the same conditions. Planar defects are marked in the inset.

TEM analysis has been performed on powder sample that was obtained by peeling of the coating with a scalpel and on a sample prepared in cross-section by tripod polishing and ion-milling. Aluminium and TiO_2 are both stable under electron beam but boehmite crystals are prone to beam damage and undergo rapid amorphisation which makes further analysis challenging. Liquid nitrogen cooling holder stage and lower accelerating voltages were used to improve the stability of the system under irradiation. EDXS was done on the selected area where defects are present and on an area without defects. Spectra in Figure 4.7 show the peaks at 4.512 eV for Ti-Kα_1 and 4.933 eV for Ti-Kβ_1 in the area of defects. No clear structure is proposed in the area of the defect due to the limitations mentioned above but layered structure suggests that the tivanite-like structure of (Al,Ti)-oxyhydroxyde is a likely candidate. EDXS mapping in Figure 4.8 shows anatase nanoparticle on the boehmite layer. The presence of titanium in boehmite is confirmed with Ti mapping.

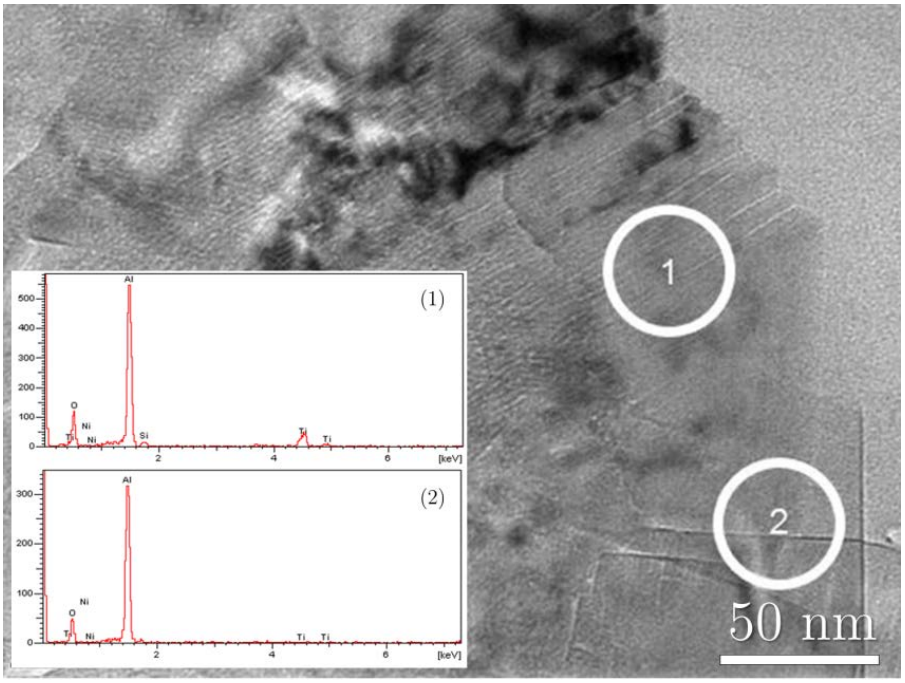


Figure 4.7: TEM image and EDXS spectra on (1) the area with defects and Ti present and (2) on the area without defects. Layered phase in the area with the defects could be a tivanite-like structure of (Al,Ti)-oxyhydroxyde.

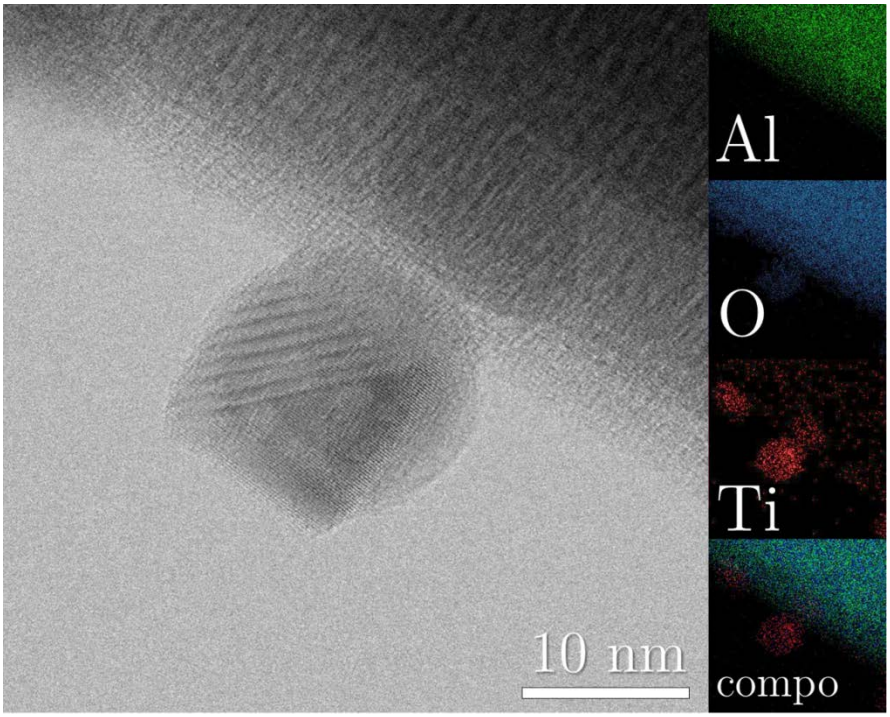


Figure 4.8: EDXS elemental mapping of TiO_2 nanoparticle on boehmite layer.

Adjustments in pH towards more acidic or alkaline environment have an influence on the substrate and TiO_2 crystallisation. Aluminium quickly corrodes outside 4–9 pH range [109]. Crystallinity and morphology of TiO_2 nano-coating were evaluated by SEM imaging (Figure 4.9). Neutral pH (7) was the most favourable condition, yielding homogeneously covered aluminium substrate with a two-layer structure: a boehmite layer covered by 10–30 nm wide TiO_2 nanoparticles (Figure 4.12).

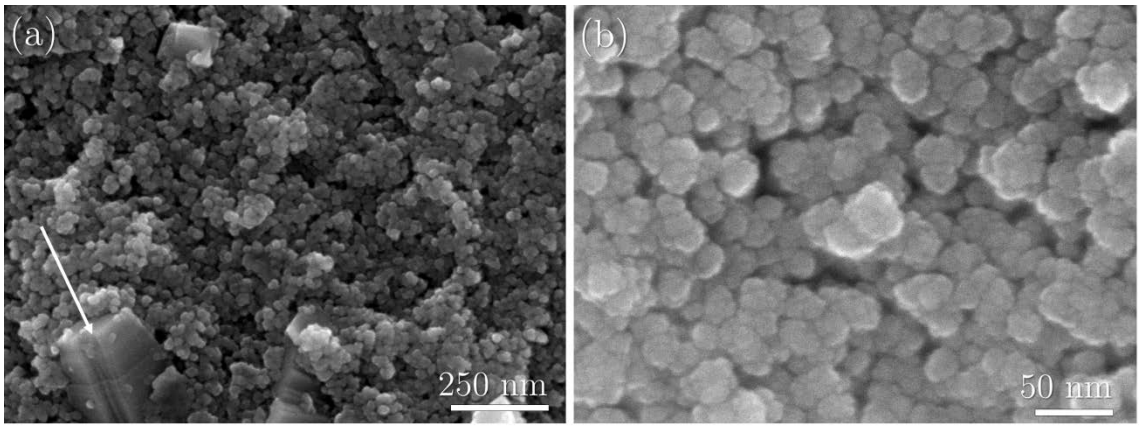


Figure 4.9: SEM micrographs of (a) boehmite crystals with TiO_2 globular nanoparticles on hydrothermally treated aluminium substrate at 200 °C / 12 h with TTIP at pH 7 and (b) higher magnification close-up. Boehmite crystal with the defects is marked with an arrow.

Calculated X-ray penetration depth for low incident angles where $\alpha \sim \alpha_c$ (critical angle) for TiO_2 is presented in Figure 4.10. In the case of a layered structure, it is important to understand the implications of the volume where the information is gathered. In the case of 20-50 nm thick TiO_2 top-most layer, conventional XRD provided unsatisfactory results. A low-angle XRD method was therefore used.

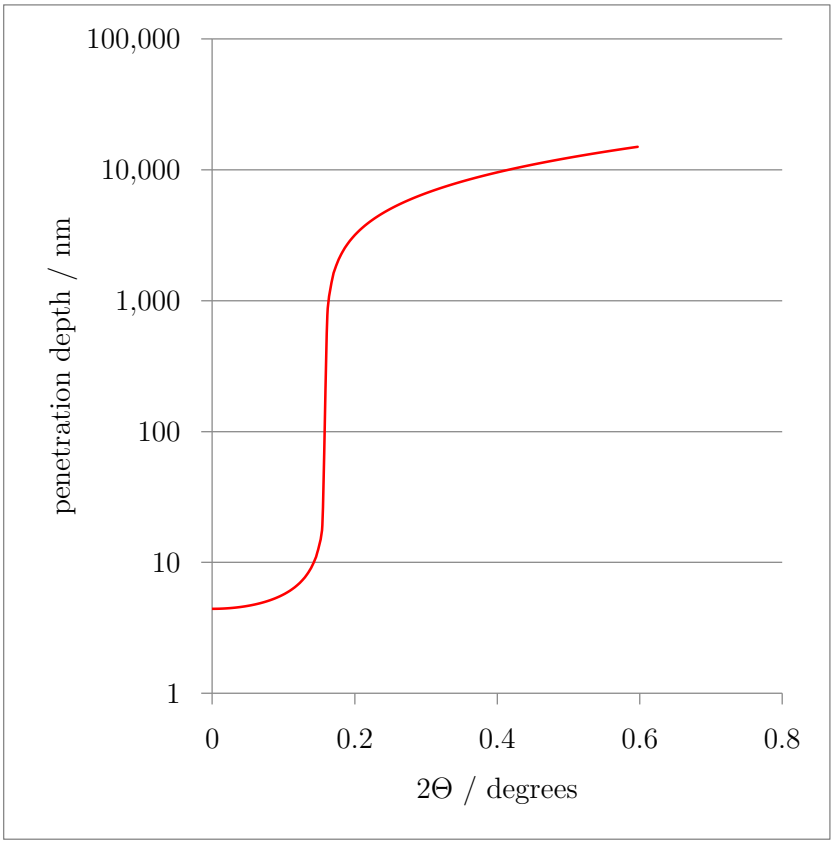


Figure 4.10: Calculated X-ray penetration depth for low incident angles where $\alpha \sim \alpha_c$ (critical angle) for TiO_2.

Due to low penetration depth, anatase and boehmite peaks are clearly seen on XRD diffractogram in Figure 4.11.

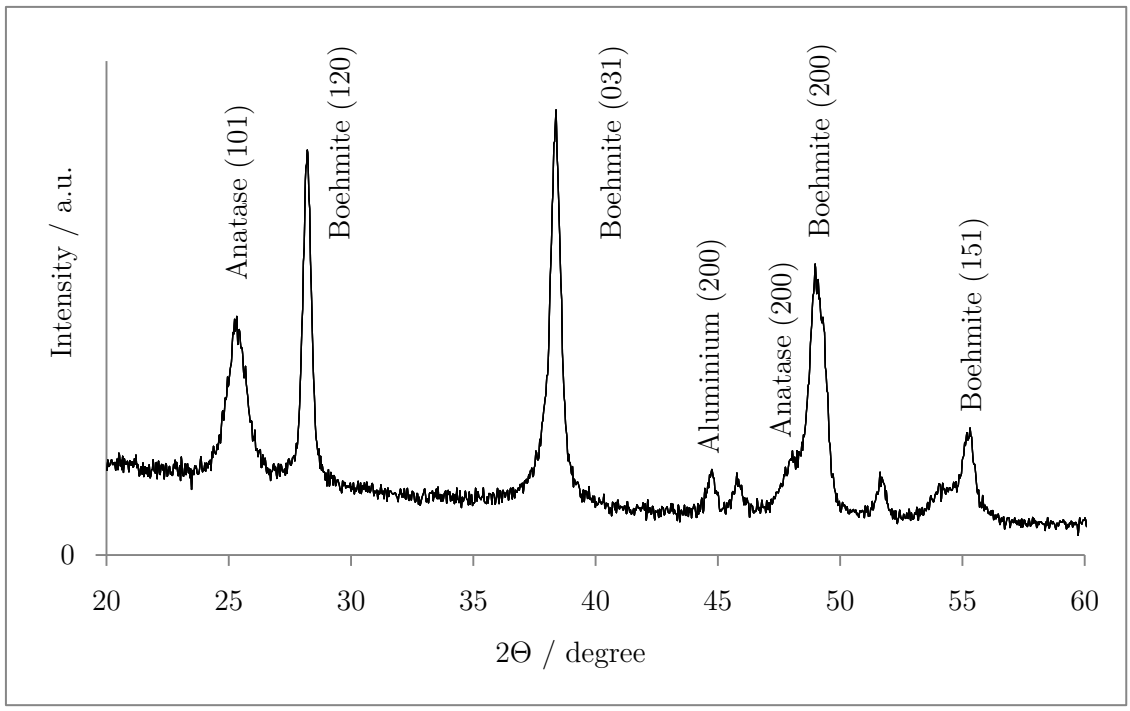


Figure 4.11: Low-angle XRD diffractogram of hydrothermally treated aluminium substrate at 200 °C / 12 h with TTIP. Anatase and boehmite peaks are clearly seen due to lower penetration depth compared to conventional XRD.

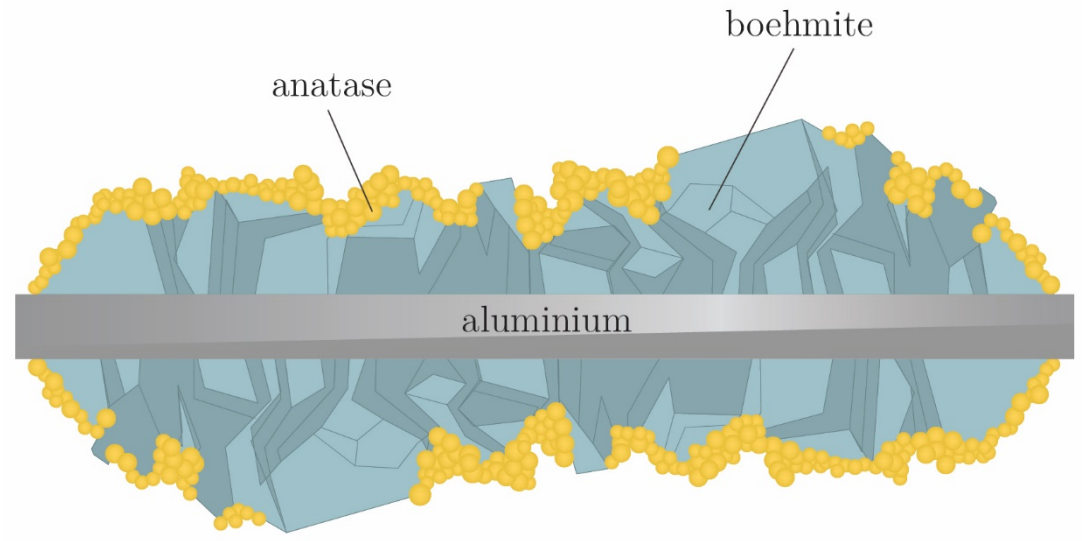


Figure 4.12: Schematic presentation of aluminium substrate covered with 1.5–2 μm thick boehmite layer and nano-sized TiO_2 particles prepared at 200 °C / 12 h with TTIP at pH 7.

Both titanium precursors used (TTIP and TBT) were used for synthesis at pH 7 and yielded substrates with similar boehmite/TiO_2 coverage. Titanium content was calculated per volume and adjusted accordingly to keep the Ti precursor concentration constant. Since no clear advantage of TBT usage over TTIP has been established, I used TTIP for

further experiments (Figure 4.13a). Prolonged synthesis times did not affect the size of TiO_2 nanoparticles but the growth of boehmite crystals was observed, similar to the case without the titanium precursor. Figure 4.13b shows SEM micrograph of aluminium/boehmite/TiO_2 surface after 62 hours of hydrothermal treatment. The size of boehmite crystals increases from 0.8 to approximately 1.5 µm compared to the sample, treated for 12 h.

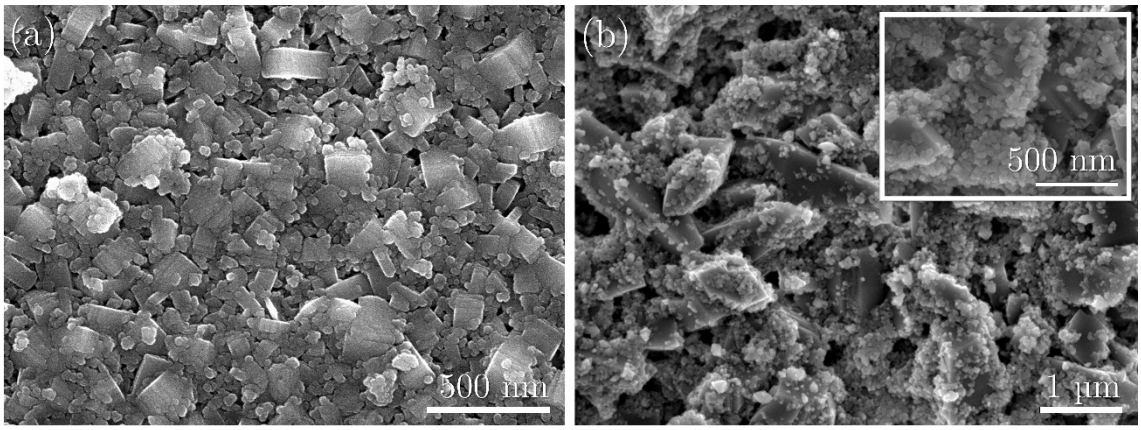


Figure 4.13: SEM micrographs of (a) hydrothermally treated aluminium substrate at 200 °C / 12 h with TBT at pH 7 and (b) prolonged synthesis (62h) at 200 °C with TTIP at pH 7.

At temperatures below 200 °C, the surface features are not well defined yet as seen on the sample prepared at 120 °C in water (Figure 4.4a). Experiments with shorter synthesis times also do not form the desired structure. In 3 h synthesis, no TiO_2 is formed on the surface. At 6 h, small clusters of TiO_2 are seen on the surface. The required time for homogenously dispersed TiO_2 nano-coating is therefore between 6 and 12 hours.

I calcined my samples at 200, 400 and 600 °C for 3–6 h to study how higher temperatures affect anatase nanoparticles. The morphology or size of TiO_2 particles did not change with annealing. Boehmite/TiO_2 coating showed the first cracks at temperatures above 400 °C due to the difference in linear thermal expansion coefficients compared to the substrate. Aluminium has, depending on an alloy, linear thermal expansion coefficient around 22×10^{-6} K^{-1} which is three times greater than the coefficient of aluminium oxides and hydroxides. There were no visible cracks on the surface at 200 °C but cracks can already be seen on a sample calcined at 400 °C (Figure 4.14). I did not observe anatase to rutile transformation during calcination. 600 °C was the highest temperature for after-treatment as alloy AA3105 has the melting point at 640 °C.

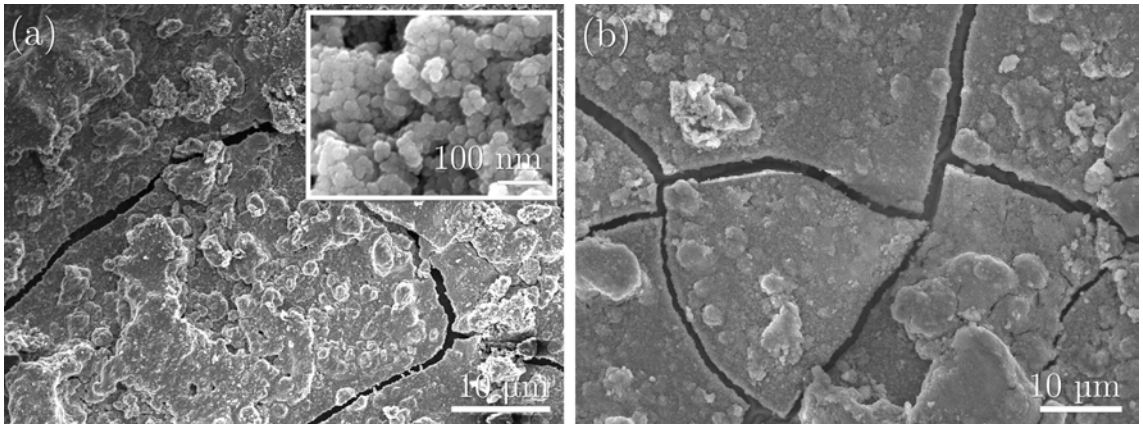


Figure 4.14: SEM micrographs of (a) calcined substrates at 400 °C for 3 h and (b) 600 °C for 6 hours. Cracks in boehmite/TiO_2 coating are due to the difference in linear thermal expansion coefficients.

TiO_2 nano-coating consists of mostly globular particles. In order to achieve better photocatalytic properties of anatase nanoparticles, HF was introduced as an additive to control and achieve crystallisation of bipyramidal shaped particles [110], [111]. HF reacts as a structuring agent and promotes {001} facet growth which is more reactive than {101} facet [112]. This is achieved by fluorination of {101} faceted surface at pH below 5.8 and sufficient HF concentration. My work has shown that the amount of TiO_2 on the aluminium is pH-dependent and pH 5.8 is not ideal for TiO_2 growth in conjunction with boehmite. I tried to compensate the inability to lower the pH with the increase in HF concentration but I could not achieve the desired effect on morphology. 3.4 mL of 0.03 M HF solution [113] was added to 46.6 mL of TTIP/dH_2O/TMAH suspension and placed in the autoclave. Hydrothermal treatment for 12 hours corroded the aluminium surface as seen in Figure 4.15. Neutralisation of HF after treatment was done by 5 M NaOH which also reacted with aluminium in caustic reaction.

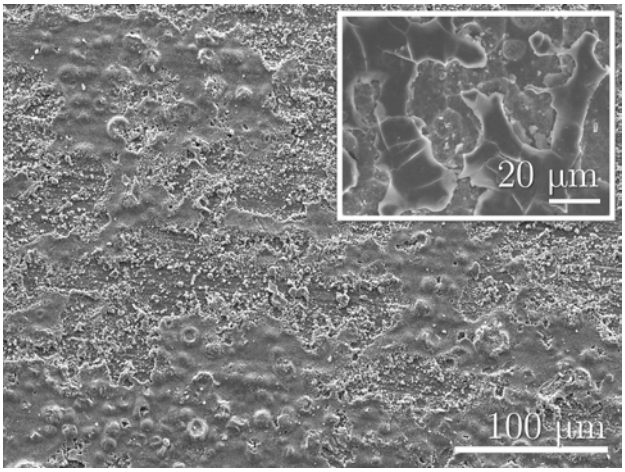


Figure 4.15: Corrosion of aluminium substrate due to the presence of HF.

4.1.2 Surface topology, roughness and contact angle measurements

Blocky boehmite crystal coating fundamentally changes the surface. Figure 4.16 shows a comparison between the treated and the untreated aluminium surface. Untreated surface exhibits general waviness as a consequence of the manufacturing process. Treated sample still has the same features but it is now covered with boehmite crystals. Roughness (R_a, Eq. (3.8)) increases from 0.21 µm for untreated samples to 0.91 µm on the samples with boehmite coating, measured on profilometer with Gaussian fitting and cut-off at 0.25 mm. Additional layer of TiO_2 smooths the surface and lowers the roughness to 0.71 µm as nanoparticles fill the pits and holes between boehmite crystals.

In order to evaluate the influence of substrate roughness on the growth of boehmite layer, I hydrothermally treated three samples: two polished on SiC P500 and SiC P1200 abrasive grinding paper and one that was electro-polished. No noticeable difference was observed on the final coatings apart from the lack of waviness (Figure 4.16) compared to untreated substrates which still retain traces of machine processing.

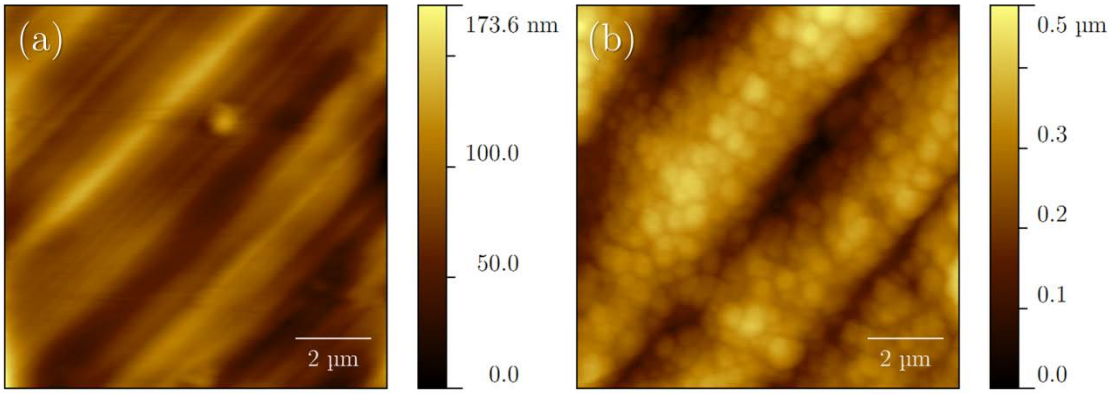


Figure 4.16: AFM imaging of (a) untreated and (b) hydrothermally treated aluminium substrate at 200 °C / 12 h. Fourfold increase in roughness is observed between the samples due to the presence of boehmite crystals. Waviness from manufacturing is retained.

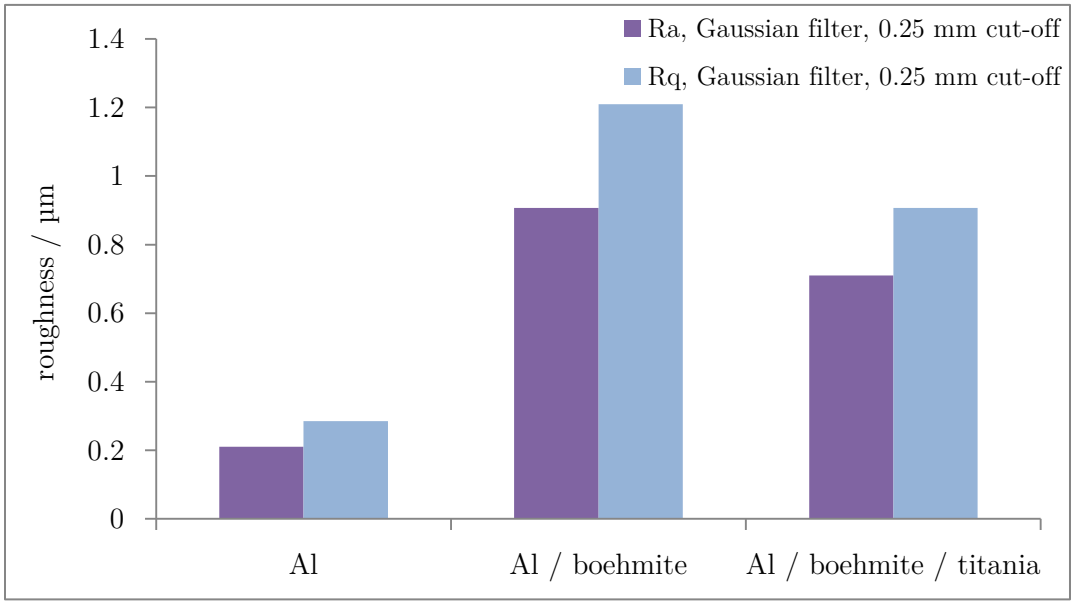


Figure 4.17: Roughness comparison between hydrothermally treated aluminium substrates. An increase in R_a and R_q is observed on the surface with boehmite crystals. Additional layer of TiO_2 smooths the surface as it fills the pits and holes between boehmite crystals.

Irradiation of the TiO_2 coated surface under UV light for a prolonged time changes the contact angle behaviour from slightly hydrophobic ($\gamma_{sg} \approx \gamma_{sl}$) to almost complete wetting ($\gamma_{sg} - \gamma_{sl} \geq \gamma_{lg}$). Three-layered structure aluminium/boehmite/TiO_2 cannot be considered superhydrophilic as those surfaces form a contact angle close to zero but generated oxygen vacancies still attract water molecules and improve wetting.

The results show that the unirradiated sample has a contact angle of 80° which drops below 15° when put under the UV light for more than 30 min (Figure 4.18).

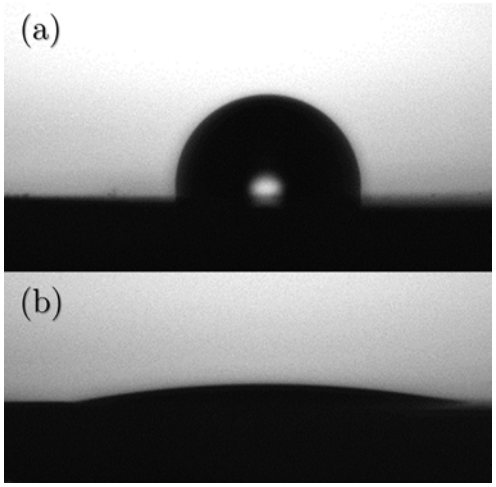


Figure 4.18: Contact angle measurements on (a) unirradiate aluminium/boehmite/TiO_2 surface and (b) UV irradiated TiO_2 coated substrate. A drop from 80° to below 15° is observed.

4.1.3 Photocatalytic activity

Figure 4.19 displays photoactivity of TiO_2 samples determined by degradation of caffeine under UV. No photocatalytic activity was observed for samples with boehmite coating without TiO_2. Samples with immobilised TiO_2 achieved 30% and 40% degradation in 3 hours with and without stirring, respectively. Comparably, Degussa P 25 powder of equivalent amount achieved total caffeine degradation in 40 minutes. The necessary amount of P 25 was determined from the volume of TiO_2 coating on aluminium. Powder and immobilised samples cannot be directly compared due to the difference in active surface between suspended powders and immobilised particles. During the hydrothermal preparation of coated aluminium samples some TiO_2 powder forms in the suspension and does not bind to the boehmite layer. The as prepared powder was dried and photocatalytic activity measured (HT 200 °C / 12 h TTIP pH7 powder). A smaller amount of active surface per volume is the main drawback of samples with an immobilised TiO_2 as their photodegradation potential is lower than powder equivalents. Although less efficient, reactors with immobilised photocatalyst are less prone to erosion of active substance to the environment. By having photocatalyst directly bonded to the substrate you avoid the need for constant photocatalyst removal and reintroduction to the system, minimising downtime.

Prolonged synthesis times, calcination and surface treatment did not influence the caffeine degradation on my catalytic coatings.

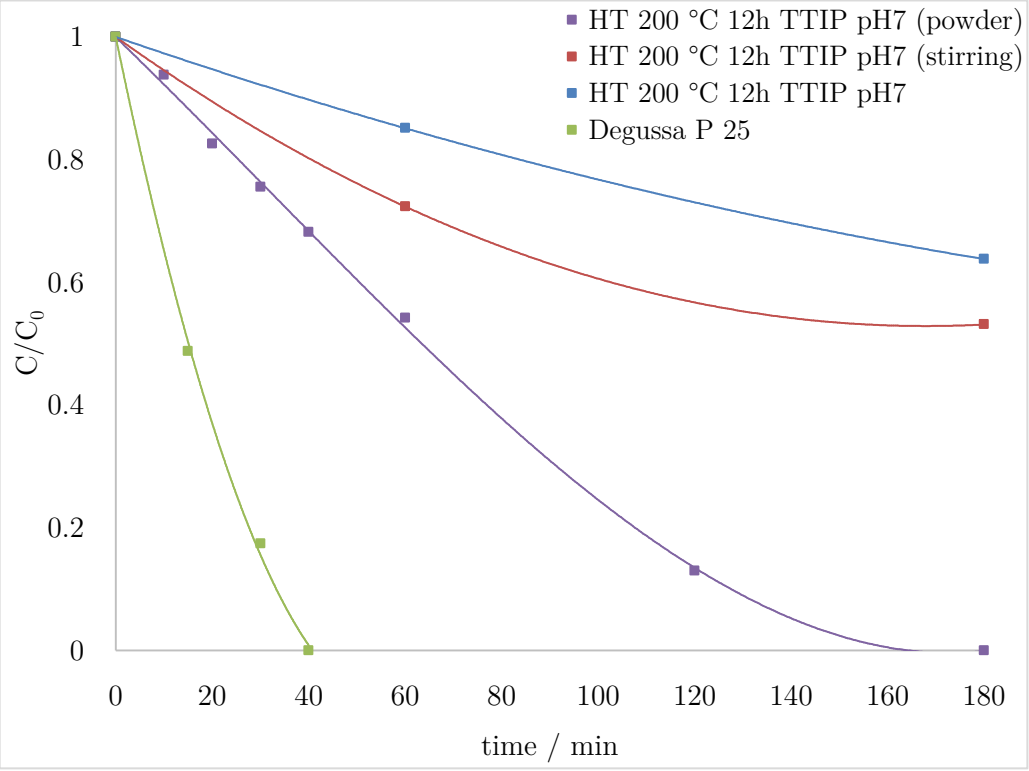


Figure 4.19: Caffeine degradation curves for Degussa P 25 (anatase/rutile) and HT 200 °C 12h TTIP pH7 sample: with and without stirring as well as extracted TiO_2 powder from the autoclave.

4.1.4 Dielectric response

Aluminium foil is commonly used as an electrode in foil capacitors. I aimed to improve the dielectric properties of the aluminium foil material for potential use in foil capacitors by the addition of hydrothermally prepared insulating boehmite barrier layer at the surface of aluminium [114]. Hydrothermal treatment was carried out in the range 100–200 °C in order to obtain most homogenous coating on a 4 µm thick foil used as an electrode in foil capacitors. Samples, hydrothermally treated at 120 °C for 12 h, are only partially covered with islands of oxyhydroxide coating as seen in Figure 4.20. Those consist of 1 µm wide amorphous globular aluminium oxyhydroxide particles that grew from aluminium substrate. Small clusters of 20–40 pseudoboehmite particles seem to share the same base from which the particles grow.

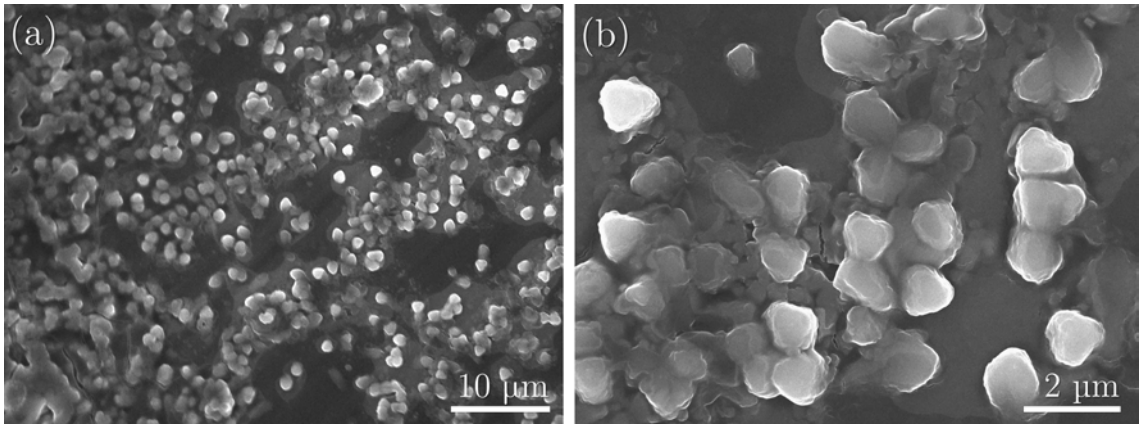


Figure 4.20: SEM micrographs of (a) hydrothermally treated aluminium foil at 120 °C / 12h at low magnification and (b) small clusters of pseudoboehmite particles.

Increase of synthesis temperature to 150 °C yields well crystallised coating that lacks the homogenous distribution of the oxyhydroxide over the whole surface. The original aluminium surface is rough and covered with small particles. Besides that, dispersed clusters, a few microns in size, are non-uniformly distributed over the surface. The number of those decreases with the increase of reaction temperature until a homogenously covered surface is formed at 200 °C as shown on Figure 4.5b. The influence of hydrothermal conditions on the size and morphology of the particles in the coatings are summarised in Table 4.2.

Table 4.2: Size, morphology and crystallinity of particles forming the coatings as a function of hydrothermal conditions.

synthesis conditions	size of particles (µm)	coating thickness (µm)	morphology and crystallinity
HT 120 °C, 12 h, pH 5.6	1–1.5	0–0.5	globular, poorly crystallised
HT 150 °C, 12 h, pH 5.6	0.2	1–2	blocky with clusters, crystallised
HT 200 °C, 12 h, pH 5.6	0.1–0.2	1.6–1.9	blocky, crystallised

The thicknesses of the coatings were measured from cross-sections made with FIB SEM (Figure 4.21), and were between 1.6–1.9 µm for the samples treated at 200 °C for 12 h. The coating homogeneously covers the whole substrate, with small fluctuations in the thickness. No pores were found inside the coatings. The boehmite growth process is the fastest at the beginning of the synthesis and slows down due to a decrease of Al atoms diffusion from the substrate to the top of the coating. The thickness of as-prepared coatings is therefore diffusion limited and does not grow more than a few microns thick. The morphology of the as-prepared boehmite crystals at 200 °C is blocky, with well-defined edges compared to the coarser, pseudoboehmite platelets and the lacy-like structure that are reported in the literature, especially at lower temperatures [115], [116]. The particle size ranges between 200–400 nm. After optimizing the preparation procedures and obtaining pore-free uniform coatings of boehmite submicron particles at the aluminium foil we characterised the dielectric properties of this material.

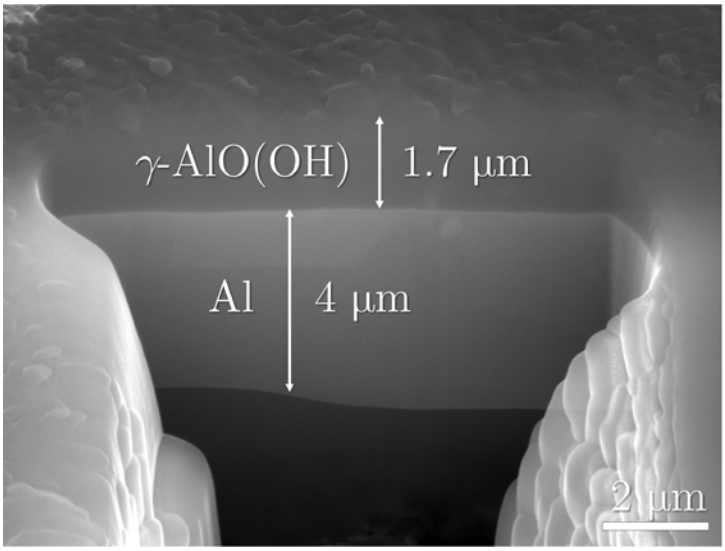


Figure 4.21: FIB cross-section on boehmite-coated aluminium foil, hydrothermally treated at 200 °C / 12 h.

Figure 4.22 shows the temperature-dependent dielectric response (the real part of the complex dielectric constant, the dielectric losses, and the real part of the complex electrical conductivity) in the boehmite layer on the aluminium foil, hydrothermally prepared at 200 °C for 12 h. With increasing temperature of measurements, the values of ε', $\tan\delta$ and σ' increase at lower frequencies; the increase in the real part of the complex electrical conductivity (σ') influences the ε' values due to the Kramers–Kronig relations and can be attributed to the thermally activated behaviour of the charge carriers.

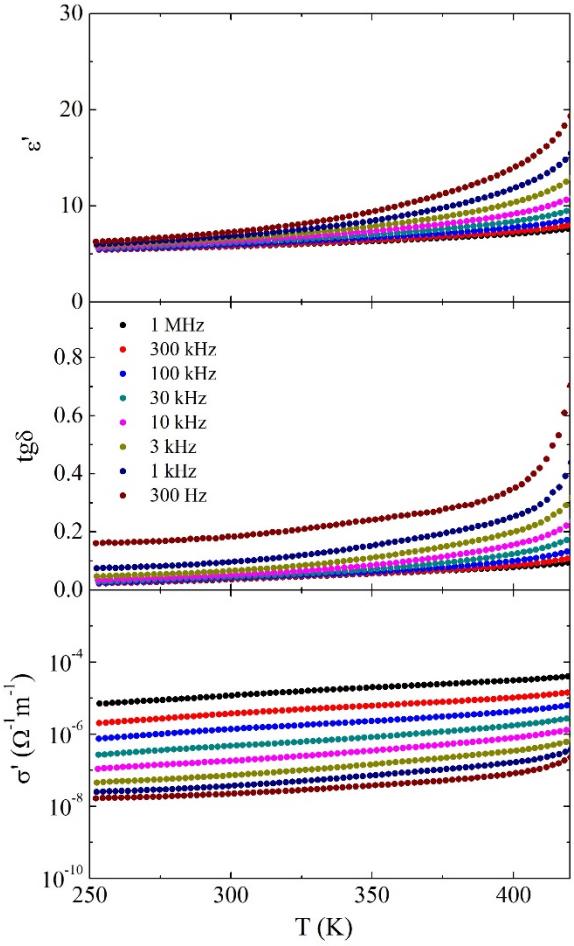


Figure 4.22: Temperature dependences of the real part of the complex dielectric constant, ε', the dielectric losses, $\tan\delta$, and the real part of the complex electrical conductivity, σ', of the boehmite layer on the aluminium foil.

In order to prepare the material with application potential, it needs to have a stable dielectric response. Figure 4.23 presents a 3D surface plot of the real part of the complex dielectric constant versus the temperature and the frequency, revealing such a response: in the boehmite layer on the aluminium foil the ε' values range from 5.5 to 6.5 over broad temperature (275–350 K) and frequency (1 kHz–1 MHz) ranges.

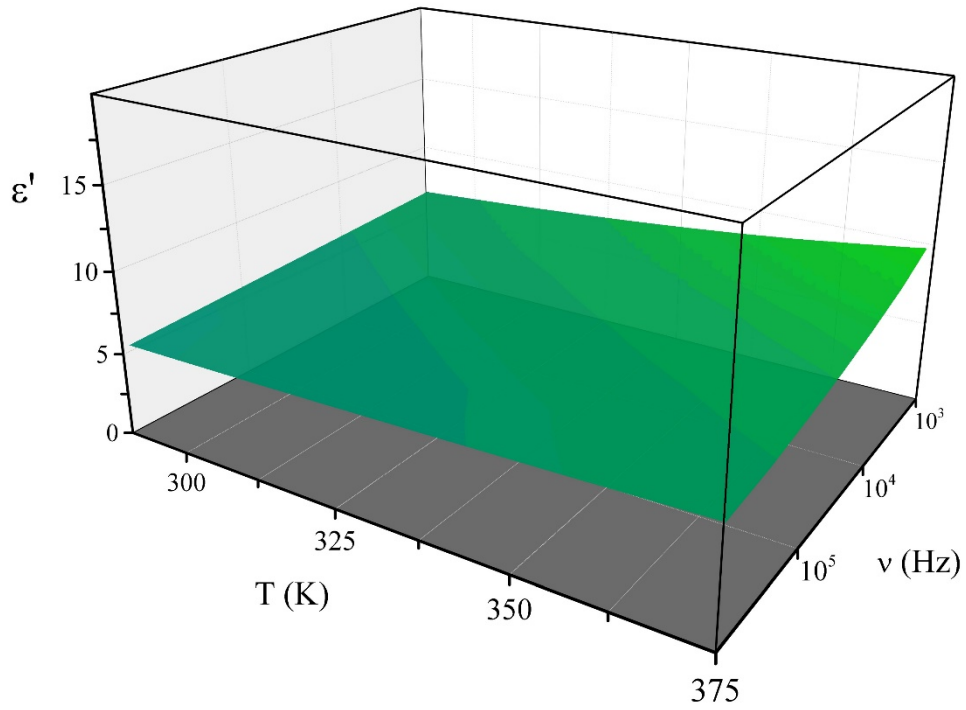


Figure 4.23: The real part of the complex dielectric constant vs. the temperature and frequency, revealing that the boehmite layer on the aluminium foil exhibits stable ε' values over broad temperature and frequency ranges.

4.2 Zinc

4.2.1 Structural and morphological properties

To cover oxidation processes on the surface of zinc I had to start at ambient conditions. Zinc oxide thin layer will quickly form on zinc surface that acts as a corrosion barrier. Most of the zinc metal is used for that exact reason; as corrosion resistance protection for other metals. Placing a piece of zinc in deionised water for 24 h results in the formation of inhomogeneous ZnO layer that can be observed with the naked eye. Experiments have shown that the oxidation process is greatly enhanced by hydrothermal treatment in water. The surface heavily corrodes and turns pitch black at temperatures about 120 °C. Synthesis in water was therefore limited to 120 °C. No passivation was observed after solvothermal treatment in pure ethanol and isopropyl alcohol up to 200 °C. Both anhydrous solvents efficiently inhibited the transport of Zn^{2+} ions that could potentially form ZnO on the surface. Additional Zn precursors were therefore introduced for solvothermal treatment. Zinc acetate dihydrate and zinc nitrate hexahydrate are both soluble in water. Synthesis parameters are summarised in Table 4.3.

Table 4.3: Parameters for hydro- and solvothermal treatment of zinc in deionised water, ethanol and isopropyl alcohol.

type	temperature	time	solvent	pH	precursor	additives
hydrothermal	80–120 °C	2–62 h	dH_2O	3–10	$Zn(NO_3)_2$, ZnAc	DAP
solvothermal	120–150 °C	6–48 h	EtOH	7.33	$Zn(NO_3)_2$	–
solvothermal	120–200 °C	6–48 h	IPA	5.5	$Zn(NO_3)_2$	–

4.2.1.1 Hydrothermally treated zinc

Growth and crystallinity of hydrothermally prepared ZnO layer can be observed on XRD diffractogram. Figure 4.24 (pattern a) diffractogram represents untreated Zn substrate (ICSD 00-004-0831) with major peaks at 36.3° for (002), 39° for (100), 43.2° for (101) and 54.3° for (102). Figure 4.24 (pattern b) shows hydrothermally treated sample at 120 °C / 12 h with clear ZnO (ICSD 01-074-0534) peaks at 31.8° for (100), 34.4° for (002), 47.5 for (102), 56.6° for (110) and 62.9° for (103). The intensity of zinc peaks drops compared to the untreated sample due to penetration depth limitations of X-rays. The sample with the addition of DAP in Figure 4.24 (pattern c) shows increased intensity in (002) direction due to the partial texturing of larger star-shaped ZnO structures on top of the well-ordered hexagonal ZnO layer seen in Figure 4.30.

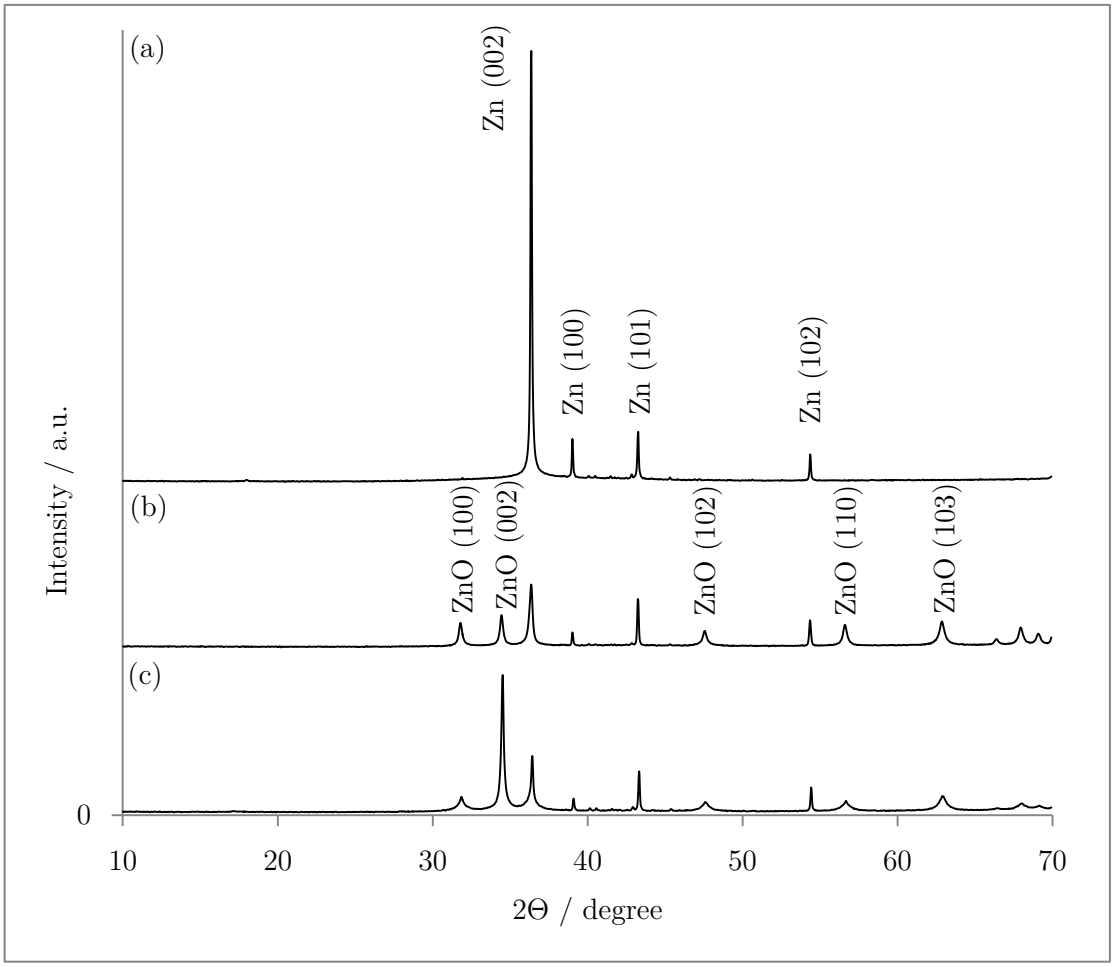


Figure 4.24: XRD diffractogram of (a) metallic untreated zinc substrate, (b) hydrothermally treated zinc at 120 °C / 12h with ZnO hedgehog-like morphology and (c) hydrothermally treated sample at 120 °C / 6 h with the addition of DAP structural agent.

Hydrothermal synthesis at 120 °C / 12 h without any additional Ti or Zn precursors completely covered the surface with hexagonal zinc oxide with a different morphology (Figure 4.25). The prevailing motif are 50–70 nm thick ZnO needles forming hedgehog-like structures approximately 8–10 µm in diameter.

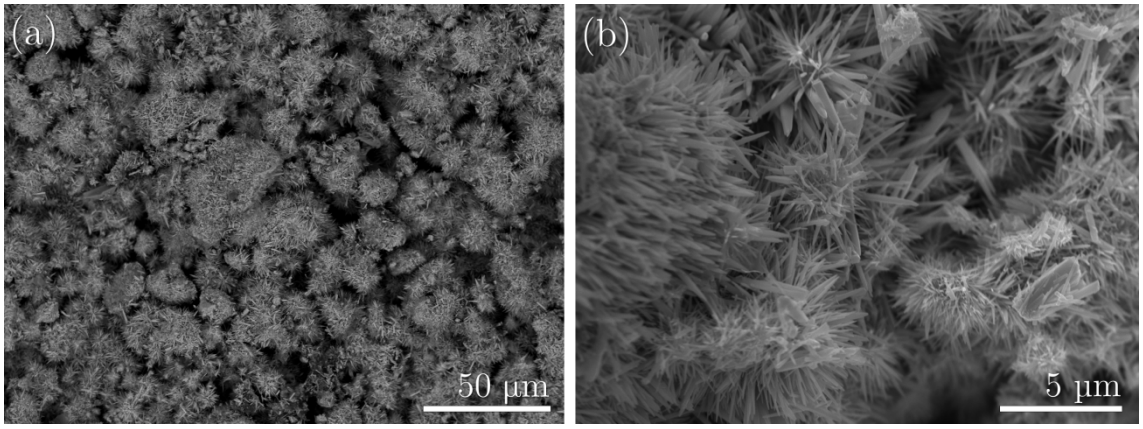


Figure 4.25: (a) Hydrothermally grown ZnO in water at 120 °C / 12h forms spikey hedgehog-like structures that homogeneously cover the substrate. (b) Higher magnification micrograph shows wurtzite needles forming structures that greatly increase the specific surface on the sample.

Adjustment in pH towards more alkaline changes the ZnO morphology without altering the other synthesis parameters. Hydrothermal treatment at 120 °C / 2h and pH 10 yielded ZnO rods instead of needles along with leaf-like hexagonal structures (Figure 4.26). ZnO have a strong preferential growth in [0001] direction. Alkaline conditions inhibit growth in [0001] and ZnO instead grows in prismatic directions $[10\bar{1}0]$, forming leaf-like hexagonal morphologies.

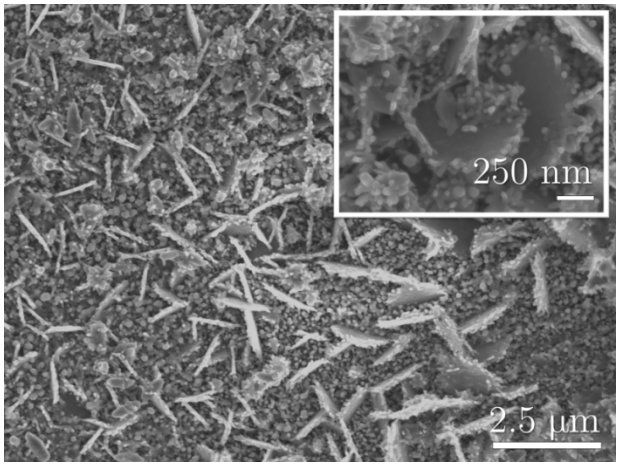


Figure 4.26: SEM micrographs of hydrothermally treated zinc sample at 120 °C / 2 h in alkaline medium (pH 10) with ZnO leaf-like hexagonal morphology.

The increase in zinc ion concentration by introducing 1.2 g of zinc acetate dihydrate into 50 ml starting solution promotes ZnO growth in the shape of thicker, 100–300 nm nanorods (Figure 4.27). This is achieved without adjustments in the pH. Rod-like morphology is more consistent across the surface compared to the samples without the precursor addition.

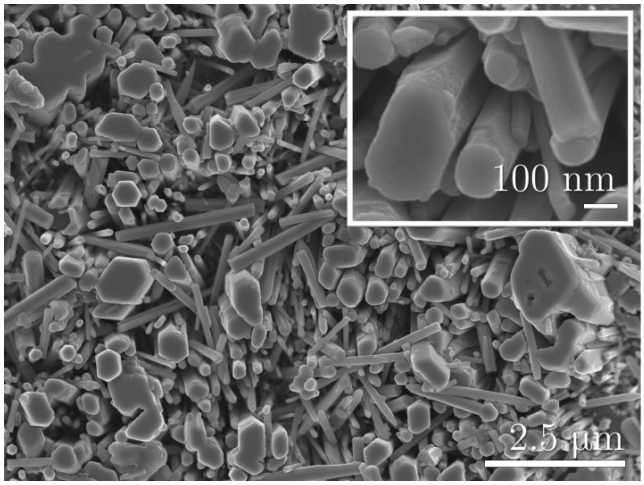


Figure 4.27: SEM micrographs of ZnO submicron rods on zinc substrate hydrothermally treated in water with the addition of the Zn precursor.

4.2.1.2 Solvothermally treated zinc

Oxidation of zinc surface in water is generally very fast. In order to achieve control over morphology and growth rate, different solvents were introduced that limit the Zn ion exchange. Synthesis in absolute ethanol without the Zn precursor leaves the surface unchanged. Different concentrations, up to 1.2 g in 50 ml, of zinc nitrate hexahydrate were added to the initial solution. For concentrations below 1.2 g the ZnO coating does not cover the whole surface and leaves parts of the surface exposed. Figure 4.28 shows a comparison between the samples with the addition of 0.6 and 1.2 g zinc nitrate hexahydrate, respectively, for solvothermally treated samples in ethanol at 120 °C / 12 h. In both cases, 200–300 nm wide hexagonal submicron ZnO rods form, stacked together to form a 0.8–1 µm thick coating. Synthesis in isopropyl alcohol behaves in the same way as the synthesis in alcohol with similar final morphology of ZnO coating; 200–300 nm wide hexagonal ZnO nanorods.

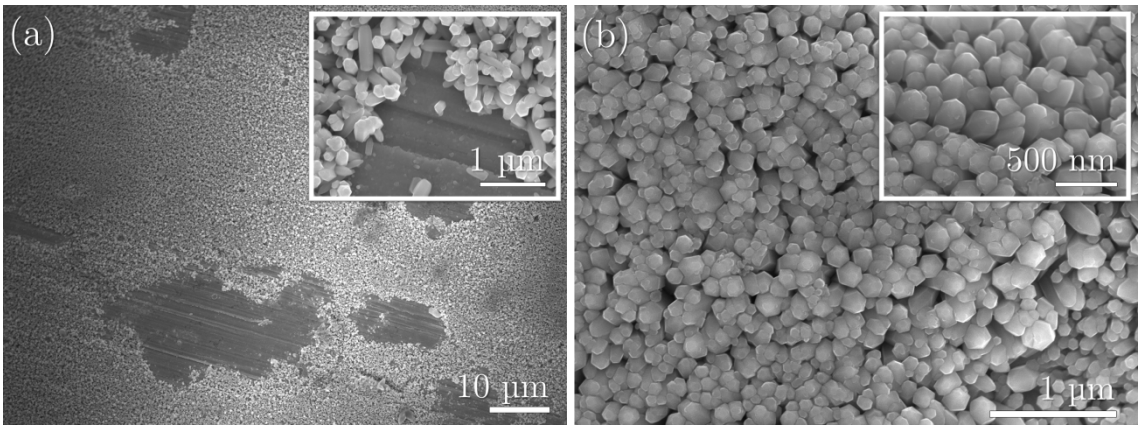


Figure 4.28: The amount of Zn precursor is crucial for homogenous coverage of ZnO in solvothermal treatment. (a) 0.6 g of zinc nitrate hexahydrate in 50 ml ethanol initial solution was not enough to achieve complete coverage at 120 °C / 12 h (b) while 1.2 g sufficed.

Prolongation of solvothermal synthesis to 48 h yielded a different coating for each of the solvents. The growth of oxide hydroxide layer on aluminium caps out at certain coating thickness due to inhibited Al transfer from the bulk to the surface. In the case of zinc, enough precursor is left in the solution to continue the growth after the initial layer of a few µm has been established. In ethanol, an overgrowth of thicker nanorods can be seen, forming 3–4 µm wide pillar-like structures coming out of the initial layer observed at synthesis times 12 h. Synthesis in isopropyl alcohol for 48 h, however, formed a completely different morphology compared to the sample at 12 h. Sharp-edged platelets, 100–400 nm in size, are covering the whole surface with no apparent ordering. Figure 4.29 shows solvothermally treated surfaces in ethanol and isopropyl alcohol for 48 h. The difference in the morphology in solvothermally treated samples in ethanol and isopropyl alcohol at 120 °C / 48 h could potentially be caused by the small amount of water in ethanol compared to completely anhydrous isopropyl alcohol. The sample in ethanol retains the preferential growth in [0001] direction while the growth in [0001] direction is inhibited on the sample in isopropyl alcohol and platelet-like crystals grow in prismatic $[10\bar{1}0]$ directions.

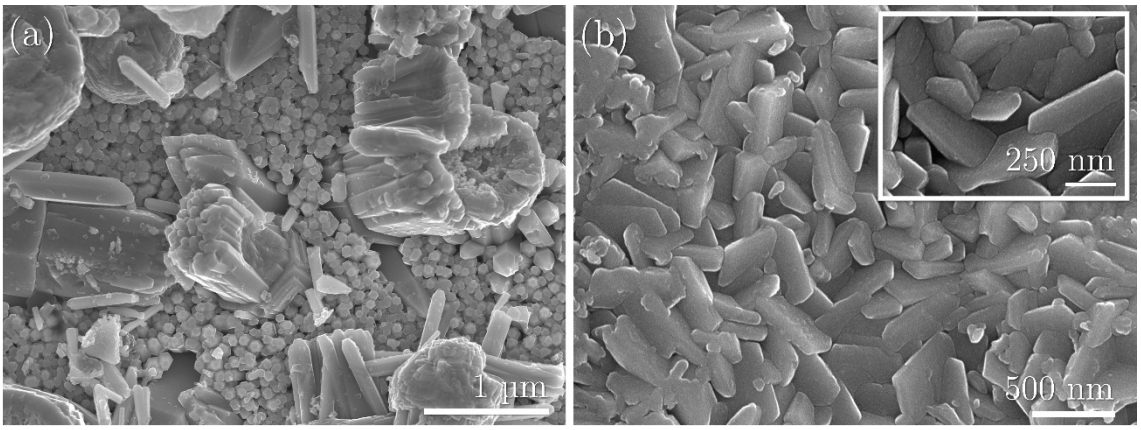


Figure 4.29: Prolonged solvothermal synthesis causes the abnormal growth over ordered hexagonal ZnO coating observed on samples treated at 120 °C / 48 h. (a) The sample in ethanol at 120 °C / 48 h retains the initial ZnO coating but forms 3–4 µm wide pillar-like structures on top. (b) The morphology of the coating in isopropyl alcohol at the same conditions completely changes and forms platelet-like morphology.

Morphology of zincite nanostructures can be tailored by the introduction of structural agents that have a preferential attachment to a certain facet and therefore inhibit the growth in that direction. A variety of structures can be synthesised this way, from very thin and sharp nano pencils to hollow microspheres (core/shell). Commonly used structural agents are trisodium citrate for core/shell structure formation [117], aminoalcohols for nanorods of different sizes as well as rice-like ZnO structure [118], cetyltrimethylammonium bromide (CTAB) shapes zincite as 50 nm thick hexagonal rods with flat terminal planes [119] and diamines for the formation of pencil-like structures that exhibit enhanced photocatalytic properties [120]. The addition of 1 ml 1,3-diaminopropane (DAP) to the 50 ml aqueous solution with 1.2 g zinc nitrate hexahydrate shaped ZnO as 40–50 nm thick nanorods that cover the whole surface. Introduction of Zn ions in solution dictates the growth of ZnO nanostructures. Comparing the surface with uneven morphology when no additives are added to the one

with them, the excess of Zn in the solution controls the rate of growth. In the case without the precursor, the growth seems to be dictated by the exchange of Zn ions from the substrate surface and therefore forms much less homogeneous coating. Samples with the addition of DAP exhibit additional, thicker star-shaped structures on top of ZnO nano-forest (Figure 4.30).

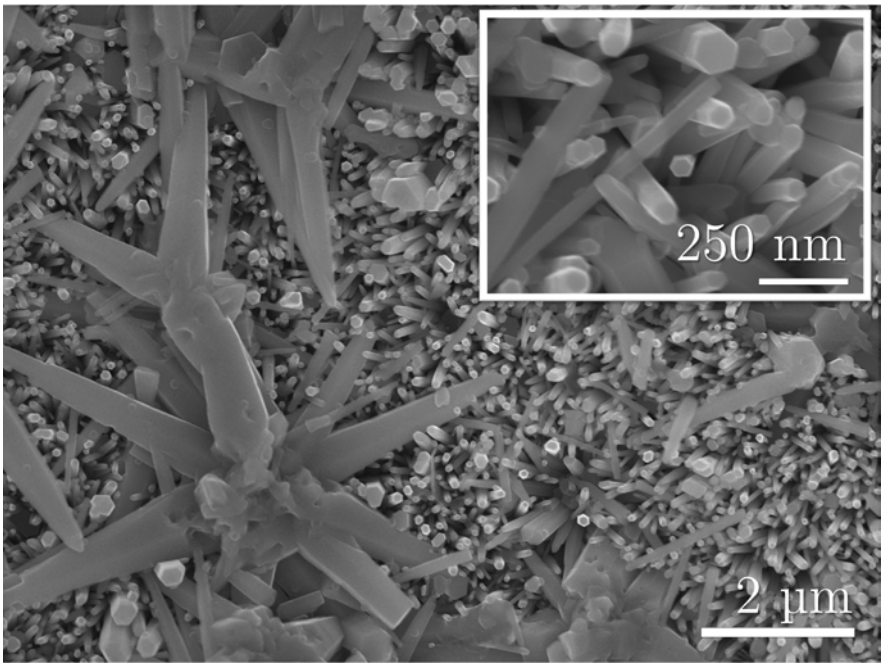


Figure 4.30: SEM micrograph and high-magnification insert of hydrothermally treated zinc substrate at 120 °C / 6 h with zinc nitrate hexahydrate and DAP structural agent.

4.2.2 Superhydrophobic coating on ZnO

Superhydrophobic conditions are achieved when very high contact angle allows for instantaneous roll-off of the droplet at low inclinations. The sheet of zinc without any treatment is hydrophobic with a contact angle around 110° (Figure 4.31). Once hydrothermally treated, oxygen and OH species on the surface increase the water attraction thus making the sample hydrophilic. The type of ZnO coating morphology does not influence the contact angle much, lowering it to approximately 40° after treatment.

To obtain superhydrophobic properties of the surface, hydrothermally treated samples were dip-coated in 10 mas% fluoroalkyl-functional siloxane (FAS) aqueous solution and fixated at 150 °C (Figure 3.1). Samples with spikey hedgehog-like morphology, prepared in water at 120 °C / 12 h, were the most suitable substrate due to higher roughness compared to solvothermally treated samples. An increase of contact angle to the range above 150° was observed. Exact measurements could not be achieved for high contact angles due to focus blur caused by limited depth of field of optical device. Figure 4.31 shows three different surface conditions on zinc: hydrophobic on untreated sample, hydrophilic on ZnO coated sample and superhydrophobic on ZnO coated sample, dip-coated in FAS. Droplet on superhydrophobic surface can be described with Cassie-Baxter state (Eq. (1.17)) where surface roughness factor (r) and fraction of different phases present under the droplet (f) play an important role in the determination of contact angle.

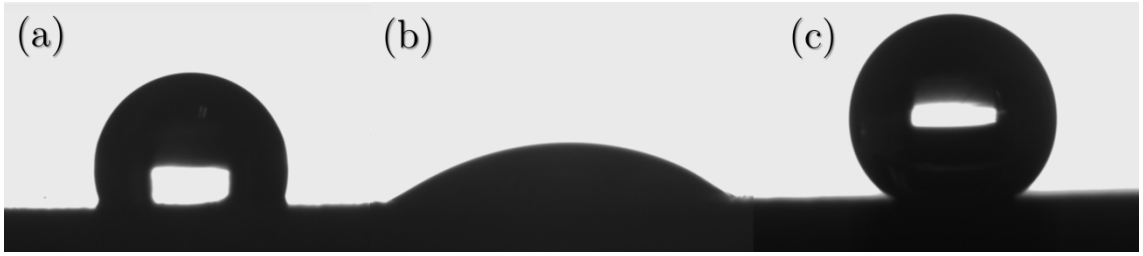


Figure 4.31: Water droplets on the zinc surfaces that underwent different treatment. (a) Untreated zinc is hydrophobic and has a contact angle of 110°. (b) Hydrothermally treated zinc with ZnO coating is hydrophilic with contact angle 40° while (c) the same surface that was treated with FAS displays superhydrophobic properties with a contact angle above 150°.

4.3 Bacterial Adhesion to Zinc and Steel Substrates

Bacterial adhesion can be dictated by surface characteristics, such as contact angle and roughness [121]. We studied how those two parameters influence the adhesion of a variety of bacteria on stainless steel and superhydrophobic hydrothermally treated zinc substrate. Bacterial adhesion characteristics on stainless steel are especially interesting since a lot of laboratory and medical equipment (laminar flow cabinets, incubators, scalpels, etc.) is made from this material. To prepare the array of surfaces with different characteristics, we used AISI 304 stainless steel substrate that was either untreated (3C) or modified by 3D polishing, brushing, grinding, electropolishing or was cleaned in Ar/O_2 plasma to lower the contact angle.

4.3.1 Roughness and contact angle measurements

Results of the profilometry and contact angle measurements in Figure 4.32 show root mean squared roughness (R_q) and contact angle of AISI 304 samples. The roughness of the 3D polished surface is the lowest (25.20 nm) whereas the highest roughness was obtained from the grinded surface (986 nm). The roughness of the electropolished surface is large compared to the 3D polished surfaces. The roughness of untreated (3C) and brushed surfaces is in the range of 100 nm. The lowest contact angle (22.3°) was measured on the plasma-cleaned surface, followed by untreated sample surface (72°). Brushing and grinding did not influence the contact angle much while 3D polishing increased the angle substantially, up to 91°. Superhydrophobic zinc surface and FAS dip-coated AISI 304 substrate are both hydrophobic with contact angles above 150° and 108°, respectively.

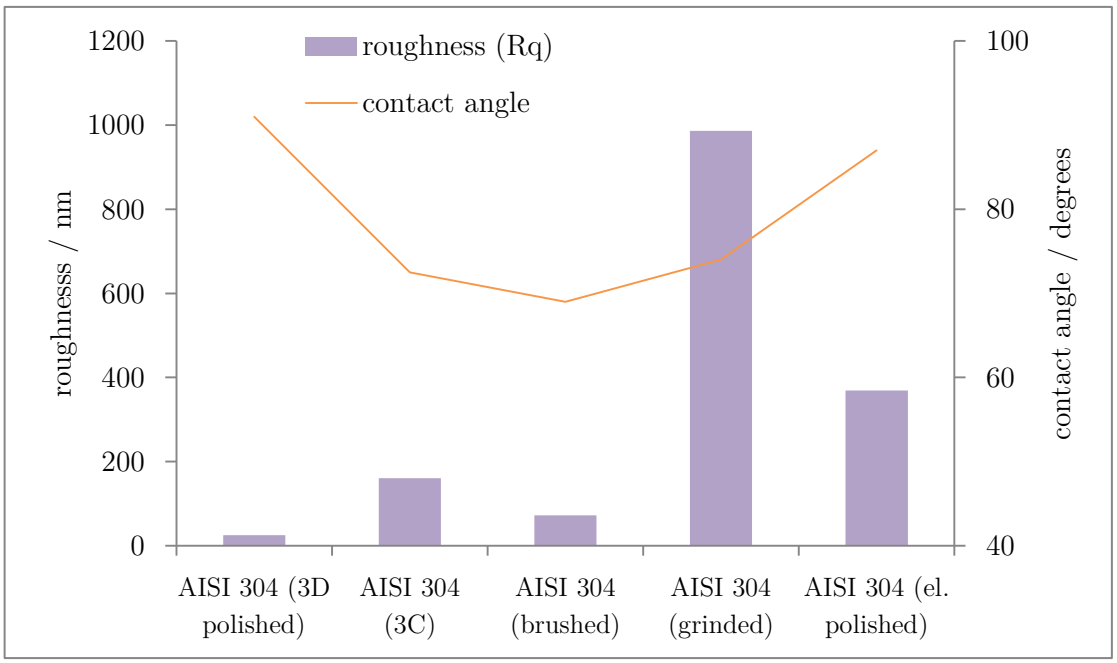


Figure 4.32: Roughness (R_q) and contact angle characteristics of AISI 304 substrates that underwent different procedures.

Contact angles on different coatings were measured as a function of time. Samples treated in plasma undergo complete relaxation back to untreated state in 3 hours. For bacterial adhesion measurements, samples were plasma-cleaned 20 min prior to overnight inoculation. To achieve hydrophobic (but not superhydrophobic) conditions on the surface of stainless steel, I dip-coated the samples in 10 mas% FAS solution and fixated them at 150 °C. An increase in contact angle from 85° to 108° was observed as seen in Figure 4.33.

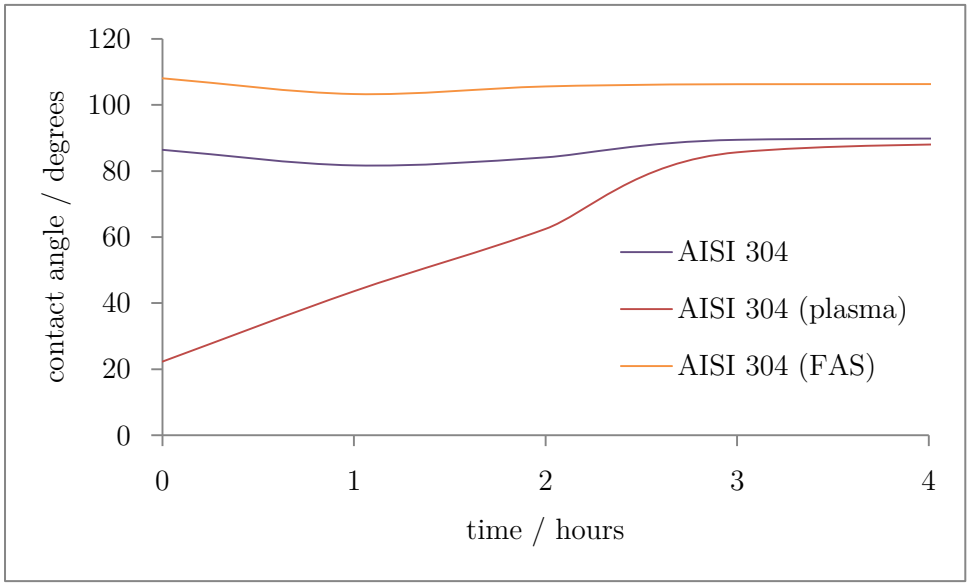


Figure 4.33: Time dependence of the contact angle. Plasma-treated sample achieves relaxation in 3 hours.

4.3.2 Bacterial adhesion to surfaces of different roughness

The study of bacterial adhesion starts with the characterisation of bacteria themselves. Bacterial surface hydrophobicity was determined with xylene and ranged from 3.5% to 42.5%. The majority of strains have a hydrophilic cell surface as their percentage of hydrophobicity was lower than 30% (Table 4.4). Exceptions were *S. aureus* ŽMJ 72 and *P. aeruginosa* ŽMJ 87. Isolates with hydrophobicity greater than 0.7 are arbitrarily classified as highly hydrophobic. Isolates with hydrophobicity rates between 0.5 and 0.7 are classified as moderate and isolates with hydrophobicity rates lower than 0.5 are classified as hydrophilic [122].

Table 4.4: Average bacterial cell hydrophobicity determined with xylene.

strain designation	% of hydrophobicity
Bacillus cereus ŽMJ 3	20.6 ± 1.6
Listeria monocytogenes ŽM 520	7.2 ± 0.9
Staphylococcus aureus ŽMJ 72	42.9 ± 14.4
Staphylococcus aureus ŽM 518	23.9 ± 6.6
Pseudomonas aeruginosa ŽMJ 87	35.5 ± 0.3
Pseudomonas aeruginosa ŽM 517	31.7 ± 17.6
Salmonella Typhimurium ŽM 375	8.2 ± 2.0
Escherichia coli ATCC 35218	23.0 ± 0.3

Adhesion of bacteria on stainless steel plates was measured by crystal violet staining. Figure 4.34 shows the average absorbance for different types of bacteria on all five types of stainless steel surfaces. The results of measured optical density (OD) at 584 nm show that the adhesion of bacteria not only depends on the surface characteristics of stainless steel but also on the type of bacteria. *B. cereus* ŽMJ 3 and *S. aureus* ŽM 72,

S. aureus ŽM 518, *P. aeruginosa* ŽM 87 and *S. Typhimurium* ŽM 375 strains adhered to all tested surfaces very weakly. On the contrary, *L. monocytogenes* ŽM 520 and *P. aeruginosa* ŽM 517 adhered strongly, especially to untreated and grinded stainless steel. Bacteria of the *Pseudomonas* genus are straight or slightly curved rods with a width of 0.5–1.0 µm and a length of 1.5–5.0 µm and strains are motile with polar flagellum. Strains of *L. monocytogenes* are also rod-shaped, measuring 0.4–0.5 µm in length and 0.5–2 µm in width and have four to six peritrichous flagella [123]. Adhesion of *E. coli* ATCC 35218 increased with the increasing roughness. It was the poorest on the 3D polished surface and was the highest on the roughest stainless steel plates (grinded).

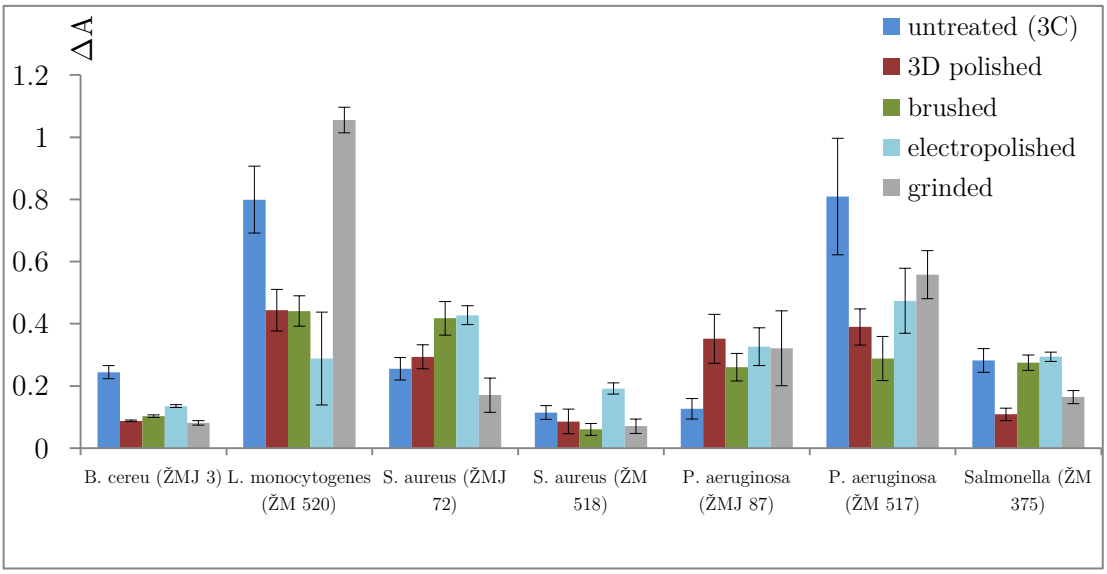


Figure 4.34: Relative adhesion rate for different bacteria on metal surfaces determined by optical density at 584 nm for different bacteria on metal disks.

The adhesion rate of bacteria on stainless steel surfaces increases with increasing the surface roughness and is statistically significant. The increased surface roughness means a larger effective surface and a higher number of cracks on the surface. The ratio between true and apparent surface area shows that the effective area can increase a few ten percent with respect to the apparent surface. This can only partly explain the up to five times larger optical density of adhered bacteria going in roughness from a few tens of nanometres to a few hundreds of nanometres. The problem of measuring the root mean squared roughness (R_q) is that the quantity does not contain any information on the morphology and the dimension of individual features (pits, holes, cavities, scratches, etc.) which obviously strongly influences the adhesion of microorganisms.

S. aureus ŽMJ 72 and *P. aeruginosa* ŽMJ 87 cells are the most hydrophobic bacteria among the tested and adhered well to stainless steel surfaces. These measurements are in agreement with the general rule that more hydrophobic bacteria adhere to the hydrophobic surface [124]. On the contrary, *L. monocytogenes* ŽM 520 was considered hydrophilic (7.2 ± 0.9) and adhered best to the untreated and grinded stainless steel surfaces. This result is in accordance with the indication [124] that material surface hydrophobicity plays a more important role than bacterial surface hydrophobicity.

Among the investigated bacteria only *L. monocytogenes* ŽM 520 and *P. aeruginosa* ŽMJ 517 adhered well to the AISI 304 surfaces. The adhesion of *L. monocytogenes* ŽM 520 was the highest on the grinded stainless steel surface which also has the highest

roughness. Grinded surfaces have the highest roughness so it was expected that adhesion would be the greatest for other bacteria as well, but in the case of *P. aeruginosa* ŽMJ 87, the best adhesion was achieved on untreated samples and slightly less on the grinded ones.

Surface roughness that is on average less than 800 nm is less prone to bacterial adhesion, and therefore more "hygienic" [125]. The roughness of untreated (3C), 3D polished, brushed, and electropolished AISI 304 samples had a lower roughness than 400 nm and in general bacterial adhesion was lower as compared to a grinded steel surface. Exceptions are *L. monocytogenes* ŽM 520 and *P. aeruginosa* ŽMJ 87 strains which exhibited better adhesion to 3C or grinded steel surfaces thus indicating the importance of bacterial strain type in influencing adhesion levels, which indicates the complexity of adhesion to abiotic surfaces. For predicting bacterial adhesion, surface roughness is only one of the controlling parameters with no universal rules of attachment having been determined yet. Other factors that are important for the adhesion of bacterial cells include the hydrophobicity of the substrate material and cell surface, production of extracellular-polymeric substances, and various environmental factors [126], [127].

4.3.3 Bacterial adhesion to surfaces of different contact angle

The influence of the contact angle on *E. coli* ATCC 35218 adhesion to the AISI 304 and zinc was measured in a wide range of contact angles, from hydrophilic plasma-treated sample to superhydrophobic zinc. The contact angle influences the bacterial adhesion to a much lesser extent than roughness. Adhesion on untreated and plasma-treated AISI 304 is largely the same. The increase of the contact angle on FAS-coated stainless steel substrate can be contributed to the silane coating that increased the contact angle but did not achieve superhydrophobicity. In the case of superhydrophobic zinc, there was no bacteria adhesion, hence the omission from the results in Figure 4.35. The lack of bacteria on zinc substrates was confirmed with SEM as well. It is therefore crucial to maintain a high contact angle (above 150°) in order to avoid pitfalls of introducing coatings that have a higher bacterial attraction than the substrate. AISI 304 sample with FAS coating was prepared in the same way as the hydrothermally treated zinc sample was, both having hydrophobic silane on top. The main reason for zinc superhydrophobicity is underlying complex ZnO structure and the lack of such features on the stainless steel substrate.

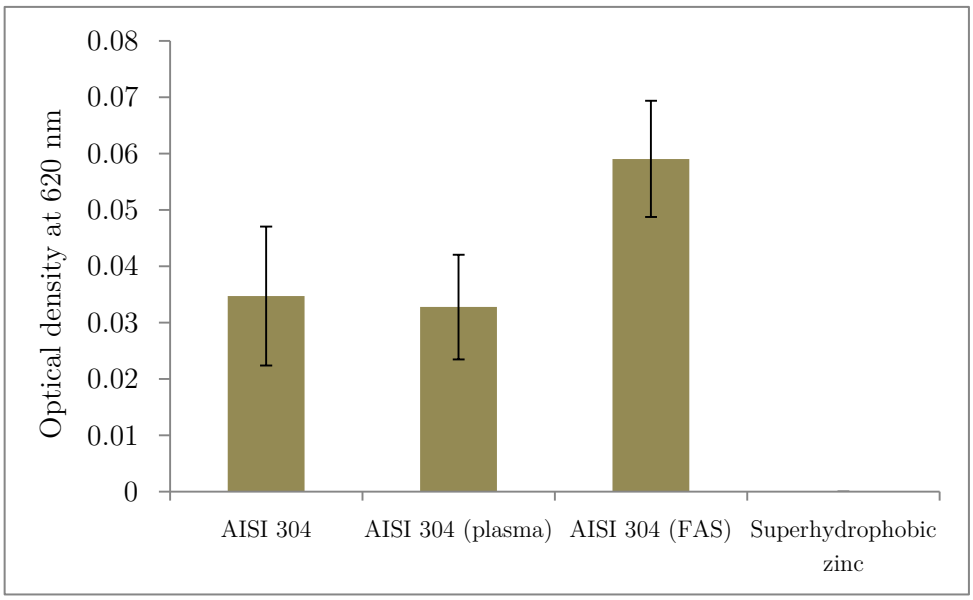


Figure 4.35: Adhesion of *E. coli* ATCC 35218 on AISI 304 substrates. No bacteria were observed on the superhydrophobic zinc substrate.

To find the locations of preferential adhesion of the microbes, the surfaces of the samples with adhered microorganisms were investigated using scanning electron microscopy (SEM). Electropolished and brushed surfaces are shown in Figure 4.36. On surfaces with a low roughness the microbes are preferentially adhered in pits, cavities and other non-regularities and they grow more or less laterally in one layer, as in the case of the brushed sample. On the surfaces with a higher roughness (electropolished AISI 304 for example) the microbes are concentrated in pores and scratches and grow in multilayers.

The time evolution of adhered bacteria showed that in the beginning the bacteria adhere around some gaps and voids of the material and the flat part of the material is not colonised. The initial adhesion of bacteria to a surface will begin at the non-regularities on the surface (cracks and grooves). The reason for this is the primitive survival instinct of bacteria as these points of interests supply protection from external forces.

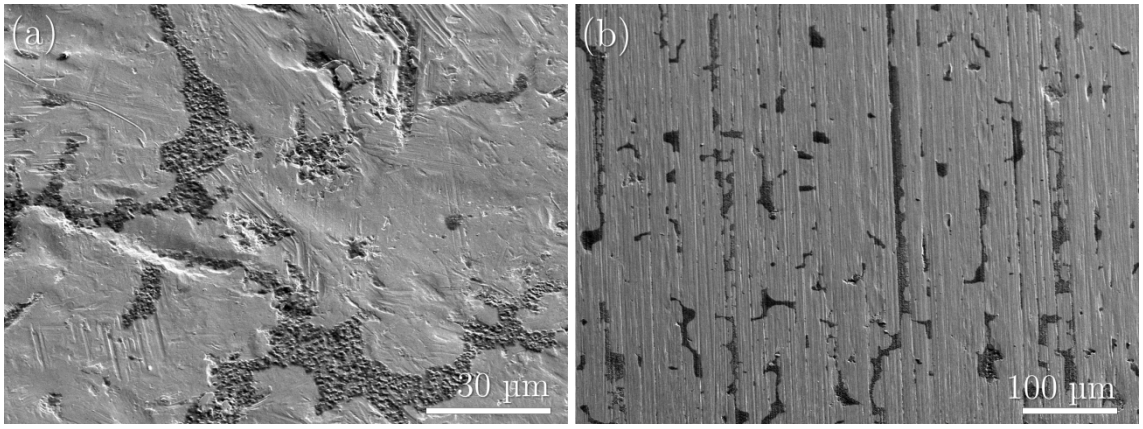


Figure 4.36: SEM micrographs with adhered bacteria for (a) brushed and (b) electropolished AISI 304 samples. The microbes preferentially adhere in pits, cavities and other non-regularities and grow laterally in one layer on surfaces with a low roughness (a). On the surfaces with a higher roughness, (b) the microbes are concentrated in pores and scratches and grow in multilayers.

Chapter 5

Conclusions

In this work, I showed that hydrothermal treatment is a versatile method for the preparation of oxide coatings on aluminium and zinc. Both metals are prone to oxidation at ambient conditions, forming thin oxide coatings. Treatment in aqueous solution only accelerates the process so special care needs to be taken in order to tailor the growth rate and, finally, the desired morphology.

Aluminium forms a 1.5–2 μm coating of aluminium oxide hydroxide (boehmite) while different morphologies of zinc oxide form on zinc substrate when hydrothermally treated at temperatures at and below 200 °C and 120 °C, respectively. As-prepared boehmite coating is suitable as an additional insulating coating in manufacturing of foil capacitors where aluminium foil is already used as an electrode. The dielectric ε' values range from 5.5 to 6.5 over broad temperature (275–350 K) and frequency (1 kHz–1 MHz) ranges which cover normal working range of foil capacitors. While the size of boehmite crystals increases slightly with prolonged synthesis times, the overall thickness of the layer changes very little due to the inhibited transport of Al atoms from the substrate through the boehmite layer.

Photocatalytic activity of hydrothermally grown TiO_2 nano-coating on aluminium achieved caffeine degradation of 40% in 3 hours with stirring while TiO_2 powder that was obtained during aluminium coating process and Degussa P25 reference achieved complete caffeine degradation in 150 and 40 min, respectively. The difference in photocatalytic activity was expected but by having the photocatalyst directly bonded to the substrate you avoid the need for constant photocatalyst removal and reintroduction to the system, minimising downtime and avoiding active substance erosion into the environment. I achieved the proposed one-step hydrothermal synthesis path for the preparation of photoactive TiO_2 coating on aluminium substrate.

Hydrothermal treatment of zinc was dominated by the rapid growth of ZnO layer with rough morphology of hedgehog-like structures composed of 50–70 nm thick ZnO needles when prepared at pH 5.6 without the addition of Zn precursor. The increase in pH and/or the addition of zinc nitrate hexahydrate into the starting solution covered the Zinc substrate with thicker nanorods over the whole surface. No ZnO layer formed in solvothermal treatment with ethanol and isopropyl alcohol unless the Zn precursor was added, showing the importance of water for the exchange of Zn atoms from the substrate.

Hydrothermally treated Zn sample at 120 °C / 6 h was dip-coated in 10 mas% FAS solution and fixated at 150 °C for 5 min to achieve superhydrophobic properties. As shown by bacterial adhesion measurements, surface roughness has a very important impact on the bacterial adhesion rate. The increased adhesion rate on more rough surfaces is forced by two factors. The first is the increasing number of non-regularities on the surface whereas the second is the increasing effective surface. We have also shown that bacterial adhesion depends on the rate of bacterial and material surface hydrophobicity as well as specific bacterial surface properties. Superhydrophobic zinc

surfaces exhibit no bacterial adhesion while AISI 304 samples all cultivated bacterial growth to some degree, depending on the surface treatment.

References

[1] K. Nakata and A. Fujishima, "TiO_2 photocatalysis: Design and applications," *J. Photochem. Photobiol. C Photochem. Rev.*, vol. 13, no. 3, pp. 169–189, 2012.

[2] A. Fujishima, T. N. Rao, and D. A. Tryk, "Titanium dioxide photocatalysis," *J. Photochem. Photobiol. C Photochem. Rev.*, vol. 1, no. 1, pp. 1–21, 2000.

[3] C. Baird and M. Cann, *Environmental Chemistry*. 2012.

[4] G. Burton and H. D. Stensel, *Wastewater engineering: Treatment and reuse*. 2003.

[5] M. Bideau, B. Claudel, C. Dubien, L. Faure, and H. Kazouan, "On the 'immobilization' of titanium dioxide in the photocatalytic oxidation of spent waters," *J. Photochem. Photobiol. A Chem.*, vol. 91, no. 2, pp. 137–144, 1995.

[6] R. Feynman, "There's Plenty of Room at the Bottom." Pasadena, 1959.

[7] D. Vollath, *Nanomaterials: An Introduction to Synthesis, Properties and Applications*. 2013.

[8] G. Cao and Y. Wang, "Nanostructures and Nanomaterials: Synthesis, Properties, and Applications." Imperial College Press, 2004.

[9] P. Rudolph, *Handbook of Crystal Growth: Bulk Crystal Growth*, vol. II. 2015.

[10] R. Landsiedel *et al.*, "Testing metal-oxide nanomaterials for human safety.," *Adv. Mater.*, vol. 22, no. 24, pp. 2601–27, Jun. 2010.

[11] K. Savolainen *et al.*, "Nanotechnologies, engineered nanomaterials and occupational health and safety - A review," *Saf. Sci.*, vol. 48, no. 8, pp. 957–963, 2010.

[12] A. Gajewicz *et al.*, "Advancing risk assessment of engineered nanomaterials: Application of computational approaches," *Adv. Drug Deliv. Rev.*, vol. 64, no. 15, pp. 1663–1693, 2012.

[13] M. Skočaj, M. Filipič, J. Petkovč, and S. Novak, "Titanium dioxide in our everyday life; is it safe?," *Radiol. Oncol.*, vol. 45, no. 4, pp. 227–47, 2011.

[14] J. A. Shin, E. J. Lee, S. M. Seo, H. S. Kim, J. L. Kang, and E. M. Park, "Nanosized titanium dioxide enhanced inflammatory responses in the septic brain of mouse," *Neuroscience*, vol. 165, no. 2, pp. 445–454, 2010.

[15] A. Weir, P. Westerhoff, L. Fabricius, K. Hristovski, and N. Von Goetz, "Titanium dioxide nanoparticles in food and personal care products," *Environ. Sci. Technol.*, vol. 46, no. 4, pp. 2242–2250, 2012.

[16] S. Novak, M. Lorenzetti, A. Drame, J. Vidmar, J. Ščančar, and M. Filipič, "Diversity of TiO_2 nanopowders characteristics relevant to toxicity testing," *J. Nanoparticle Res.*, vol. 18, no. 5, 2016.

[17] Y. Xu and M. A. A. Schoonen, "The Absolute Energy Positions of Conduction

and Valence Bands of Selected Semiconducting Minerals," *Am. Mineral.*, vol. 85, pp. 543–556, 2000.

[18] A. Pimpin and W. Srituravanich, "Reviews on micro- and nanolithography techniques and their applications," *Eng. J.*, vol. 16, no. 1, pp. 37–55, 2012.

[19] K. Byrappa and T. Adschiri, "Hydrothermal technology for nanotechnology," *Prog. Cryst. Growth Charact. Mater.*, vol. 53, no. 2, pp. 117–166, Jun. 2007.

[20] A. Byrappa and M. Yoshimura, *Handbook of hydorthermal technology.* Noyes Publications, 2001.

[21] R. A. Laudise, "Hydrothermal Synthesis of Single Crystals," in *Progress in Inorganic Chemistry*, John Wiley & Sons, Inc., 2007, pp. 1–47.

[22] A. Rabenau, "The Role of Hydrothermal Synthesis in Preparative Chemistry," *Angew. Chemie Int. Ed. English*, vol. 24, no. 12, pp. 1026–1040, 1985.

[23] R. Bunsen, *Annalen der Chemie und Pharmacie*, vol. 65. 1848.

[24] G. Spezia, *Atti della Reale Accademia delle scienze di Torino.* 1905.

[25] A. E. Danks, S. R. Hall, and Z. Schnepp, "The evolution of 'sol–gel' chemistry as a technique for materials synthesis," *Mater. Horizons*, vol. 3, pp. 91–112, 2016.

[26] D. Mukherjee, S. Barghi, and A. Ray, "Preparation and Characterization of the TiO_2 Immobilized Polymeric Photocatalyst for Degradation of Aspirin under UV and Solar Light," *Processes*, vol. 2, no. 1, pp. 12–23, 2013.

[27] R. L. Pozzo, M. a. Baltanás, and a. E. Cassano, "Supported titanium oxide as photocatalyst in water decontamination: State of the art," *Catal. Today*, vol. 39, no. 3, pp. 219–231, 1997.

[28] A. Y. Shan, T. I. M. Ghazi, and S. A. Rashid, "Immobilisation of titanium dioxide onto supporting materials in heterogeneous photocatalysis: A review," *Appl. Catal. A Gen.*, vol. 389, no. 1–2, pp. 1–8, 2010.

[29] J. A. Byrne, B. R. Eggins, N. M. D. Brown, B. McKinney, and M. Rouse, "Immobilisation of TiO_2 powder for the treatment of polluted water," *Appl. Catal. B Environ.*, vol. 17, no. 1–2, pp. 25–36, 1998.

[30] W. S. Miller *et al.*, "Recent development in aluminium alloys for the automotive industry," *Mater. Sci. Eng. A*, vol. 280, no. 1, pp. 37–49, 2000.

[31] M. Kendig, "Corrosion Inhibition of Aluminum and Aluminum Alloys by Soluble Chromates , Chromate Coatings , and Chromate-Free Coatings Corrosion Inhibition of Aluminum and Aluminum Alloys by Soluble Chromates , Chromate Coatings , and Chromate-Free Coatings," vol. 59, no. October, pp. 379–400, 2016.

[32] R. L. Twite and G. P. Bierwagen, "Review of alternatives to chromate for corrosion protection of aluminum aerospace alloys," *Prog. Org. Coatings*, vol. 33, no. 2, pp. 91–100, 1998.

[33] T. Ishiguro, T. Hori, and Z. Qiu, "Antireflective coating using aluminum hydroxide formed by hydrothermal treatment of sputtered aluminum films," *J. Appl. Phys.*, vol. 106, no. 2, pp. 2–5, 2009.

[34] R. S. Alwitt, "The Growth of Hydrous Oxide Films on Aluminum," *J. Electrochem. Soc.*, vol. 121, no. 10, pp. 1322–1328, 1974.

[35] G. C. Kennedy, "Phase relations in the system of Al_2O_3-H_2O at high temperatures and pressures," *Am. J. Sci.*, vol. 257, pp. 563–573, 1959.

[36] A. W. Laubengayer and R. S. Weisz, "A hydrothermal study of equilibria in the system alumina—water," *J. Am. Chem. Soc.*, vol. 483, no. 65, pp. 247–250, 1943.

[37] T. S. Kannan, P. K. Panda, and V. A. Jaleel, "Preparation of pure boehmite, α–Al_2O_3 and their mixtures by hydrothermal oxidation of aluminium metal," *J. Mater. Sci. Lett.*, vol. 16, pp. 830–834, 1997.

[38] D. D. MacDonald and P. Butler, "The thermodynamics of the aluminium-water system at elevated temperatures," *Corros. Sci.*, vol. 13, no. 4, pp. 259–274, 1973.

[39] P. T. Craddock, "The composition of the copper alloys used by the Greek, Ertruscan and Roman Civilisations," *J. Archaeol. Sci.*, vol. 4, pp. 102–123, 1977.

[40] X. G. Zhang, *Corrosion and Electrochemistry of Zinc*. Springer, 1996.

[41] Ü. Özgür *et al.*, "A comprehensive review of ZnO materials and devices," *J. Appl. Phys.*, vol. 98, no. 4, pp. 1–103, 2005.

[42] A. Mclaren, T. Valdes-Solis, G. Li, and S. C. Tsang, "Shape and size effects of ZnO nanocrystals on photocatalytic activity," *J. Am. Chem. Soc.*, vol. 131, no. 35, pp. 12540–12541, 2009.

[43] L. Vayssieres, "Growth of Arrayed Nanorods and Nanowires of ZnO from Aqueous Solutions," *Adv. Mater.*, vol. 15, no. 5, pp. 464–466, Mar. 2003.

[44] S. Baruah and J. Dutta, "Effect of seeded substrates on hydrothermally grown ZnO nanorods," *J. Sol-Gel Sci. Technol.*, vol. 50, no. 3, pp. 456–464, 2009.

[45] F. H. Alsultany, Z. Hassan, and N. M. Ahmed, "Low-power UV photodetection characteristics of ZnO tetrapods grown on catalyst-free glass substrate," *Sensors Actuators, A Phys.*, vol. 250, pp. 187–194, 2016.

[46] W. Zhong Lin, "Zinc oxide nanostructures: growth, properties and applications," *J. Phys. Condens. Matter*, vol. 16, no. 25, pp. R829--R858, 2004.

[47] N. Ekthammathat, T. Thongtem, A. Phuruangrat, and S. Thongtem, "Characterization of ZnO flowers of hexagonal prisms with planar and hexagonal pyramid tips grown on Zn substrates by a hydrothermal process," *Superlattices Microstruct.*, vol. 53, pp. 195–203, Jan. 2013.

[48] H. Li *et al.*, "Precursor-controlled synthesis of different ZnO nanostructures by the hydrothermal method," *Phys. Status Solidi Appl. Mater. Sci.*, vol. 211, no. 3, pp. 595–600, 2014.

[49] S. Baruah and J. Dutta, "pH-dependent growth of zinc oxide nanorods," *J. Cryst. Growth*, vol. 311, no. 8, pp. 2549–2554, 2009.

[50] H. Zhang and J. F. Banfield, "Understanding Polymorphic Phase Transformation Behavior during Growth of Nanocrystalline Aggregates: Insights from TiO_2," *J. Phys. Chem. B*, vol. 104, no. 15, pp. 3481–3487, 2000.

[51] O. Legrini, E. Oliveros, and A. M. Braun, "Photochemical processes for water treatment," *Chem. Rev.*, vol. 93, no. 2, pp. 671–698, Mar. 1993.

[52] T. Oppenlander, *Photochemical Purification of Water and Air: Advanced Oxidation Processes (AOPs) - Principles, Reaction Mechanisms, Reactor Concepts*. 2007.

[53] O. Carp, C. L. Huisman, and A. Reller, "Photoinduced reactivity of titanium dioxide," *Prog. Solid State Chem.*, vol. 32, no. 1–2, pp. 33–177, 2004.

[54] J. Schneider *et al.*, "Understanding TiO_2 Photocatalysis: Mechanisms and

Materials," *Chem. Rev.*, vol. 114, pp. 9919–9986, 2014.

[55] A. Mills and S. Le Hunte, "An overview of semiconductor photocatalysis," *J. Photochem. Photobiol. A Chem.*, vol. 108, no. 1, pp. 1–35, 1997.

[56] M. A. Fox and M. T. Dulay, "Heterogeneous Photocatalysis," *Chem. Rev.*, vol. 93, no. 1, pp. 341–357, 1993.

[57] P. K. J. Robertson, D. W. Bahnemann, J. M. C. Robertson, and F. Wood, "Photocatalytic Detoxification of Water and Air," in *Environmental Photochemistry Part II*, P. Boule, D. W. Bahnemann, and P. K. J. Robertson, Eds. Berlin, Heidelberg: Springer Berlin Heidelberg, 2005, pp. 367–423.

[58] K. Ishibashi, A. Fujishima, T. Watanabe, and K. Hashimoto, "Quantum yields of active oxidative species formed on TiO_2 photocatalyst," *J. Photochem. Photobiol. A Chem.*, vol. 134, no. 1–2, pp. 139–142, 2000.

[59] A. Mills, C. Hill, and P. K. J. Robertson, "Overview of the current ISO tests for photocatalytic materials," *J. Photochem. Photobiol. A Chem.*, vol. 237, pp. 7–23, 2012.

[60] A. Houas, H. Lachheb, M. Ksibi, E. Elaloui, C. Guillard, and J. Herrmann, "Photocatalytic degradation pathway of methylene blue in water," *Appl. Catal. B Environ.*, vol. 31, no. 2, pp. 145–157, 2001.

[61] M. Krivec, R. A. Segundo, J. L. Faria, A. M. T. Silva, and G. Dražić, "Low-temperature synthesis and characterization of rutile nanoparticles with amorphous surface layer for photocatalytic degradation of caffeine," *Appl. Catal. B Environ.*, vol. 140–141, pp. 9–15, 2013.

[62] L. C. Chuang, C. H. Luo, S. W. Huang, Y. C. Wu, and Y. C. Huang, "Photocatalytic Degradation Mechanism and Kinetics of Caffeine in Aqueous Suspension of Nano-TiO_2," *Adv. Mater. Res.*, vol. 214, pp. 97–102, 2011.

[63] S. Sauvé, K. Aboulfadl, S. Dorner, P. Payment, G. Deschamps, and M. Prévost, "Fecal coliforms, caffeine and carbamazepine in stormwater collection systems in a large urban area," *Chemosphere*, vol. 86, no. 2, pp. 118–123, 2012.

[64] G. Kumar and K. N. Prabhu, "Review of non-reactive and reactive wetting of liquids on surfaces," *Adv. Colloid Interface Sci.*, vol. 133, no. 2, pp. 61–89, 2007.

[65] N. Eustathopoulos, "Dynamics of wetting in reactive metal/ ceramic systems," *Acta Mater.*, vol. 46, no. 7, pp. 2319–2327, 1998.

[66] T. Young, "An Essay on the Cohesion of Fluids," *Philos. Trans. R. Soc. London*, vol. 95, no. 0, pp. 65–87, 1805.

[67] J. T. Davies and E. K. Rideal, "Interfacial Phenomena," *J. Chem. Educ.*, vol. 65, no. 7, pp. 1–52, 1988.

[68] R. E. Johnson and R. H. Dettre, "Contact Angle Hysteresis. III. Study of an Idealized Heterogeneous Surface," *J. Phys. Chem.*, vol. 68, no. 7, pp. 1744–1750, 1964.

[69] J. Drelich and E. Chibowski, "Superhydrophilic and superwetting surfaces: Definition and mechanisms of control," *Langmuir*, vol. 26, no. 24, pp. 18621–18623, 2010.

[70] A. B. D. Cassie and S. Baxter, "Contact angle," in *Discussions of the Faraday Society*, 1948, p. 3:11.

[71] W. D. Kaplan, D. Chatain, P. Wynblatt, and W. C. Carter, "A review of wetting versus adsorption, complexions, and related phenomena: The rosetta stone of wetting," *J. Mater. Sci.*, vol. 48, no. 17, pp. 5681–5717, 2013.

[72] G. Whyman, E. Bormashenko, and T. Stein, "The rigorous derivation of Young, Cassie-Baxter and Wenzel equations and the analysis of the contact angle hysteresis phenomenon," *Chem. Phys. Lett.*, vol. 450, no. 4–6, pp. 355–359, 2008.

[73] C. W. Extrand, "Model for contact angles and hysteresis on rough and ultraphobic surfaces," *Langmuir*, vol. 18, no. 21, pp. 7991–7999, 2002.

[74] A. A. Ashkarran and M. R. Mohammadizadeh, "Superhydrophilicity of TiO_2 thin films using $TiCl_4$ as a precursor," *Mater. Res. Bull.*, vol. 43, no. 3, pp. 522–530, 2008.

[75] A. Nakajima, S. Koizumi, T. Watanabe, and K. Hashimoto, "Effect of repeated photo-illumination on the wettability conversion of titanium dioxide," *J. Photochem. Photobiol. A Chem.*, vol. 146, pp. 129–132, 2001.

[76] H. Irie and K. Hashimoto, "Photocatalytic Active Surfaces and Photo-Induced High Hydrophilicity / High Hydrophobicity," in *The Handbook of Environmental Chemistry, Environmental Photochemistry Part II*, vol. 2, no. September, 2005, pp. 425–450.

[77] M. Takeuchi, K. Sakamoto, G. Martra, S. Coluccia, and M. Anpo, "Mechanism of photoinduced superhydrophilicity on the TiO_2 photocatalyst surface," *J. Phys. Chem. B*, vol. 109, no. 32, pp. 15422–15428, 2005.

[78] L. Zhang, R. Dillert, D. Bahnemann, and M. Vormoor, "Photo-induced hydrophilicity and self-cleaning: models and reality," *Energy Environ. Sci.*, vol. 5, no. 6, pp. 7491–7507, 2012.

[79] T. Darmanin and F. Guittard, "Superhydrophobic and superoleophobic properties in nature," *Mater. Today*, vol. 18, no. 5, pp. 273–285, 2015.

[80] A. T. Abdulhussein, G. K. Kannarpady, A. B. Wright, A. Ghosh, and A. S. Biris, "Current trend in fabrication of complex morphologically tunable superhydrophobic nano scale surfaces," *Appl. Surf. Sci.*, vol. 384, pp. 311–332, 2016.

[81] A. Eftekhari, "Aluminum as a suitable substrate for the deposition of conducting polymers: Application to polyaniline and enzyme-modified electrode," *Synth. Met.*, vol. 125, no. 3, pp. 295–300, 2002.

[82] P. K. Kabada and B. Dobbs, "Dielectric study of anodized foils of aluminum electrolytic capacitors," *Mater. Sci. Eng.*, vol. 54, no. 2, pp. 279–283, 1982.

[83] J. Yoo, J. Kim, and Y. S. Kim, "Liquid electrolyte-free cylindrical Al polymer capacitor review: Materials and characteristics," *J. Power Sources*, vol. 284, pp. 466–480, 2015.

[84] A. Mata Arjona and J. J. Fripirat, "Part 2. - Dielectric and Diffusion Measurements in Boehmite," in *Proton Mobility in Solids*, Trans. Faraday Soc., 1967, pp. 2936–2944.

[85] A. Mozalev, M. Sakairi, H. Takahashi, H. Habazaki, and J. Hubálek, "Nanostructured anodic-alumina-based dielectrics for high-frequency integral capacitors," *Thin Solid Films*, vol. 550, pp. 486–494, 2014.

[86] A. C. Geiculescu, J. L. Stevens, T. F. Strange, S. J. Medical, C. Operation, and M. M. Highway, "Nano-Composite Barrier Anodic Aluminum Oxide for ICD Capacitors," *NSTI-Nanotech 2006*, vol. 3, pp. 3–6, 2006.

[87] X. Liu, C. Niu, X. Zhen, J. Wang, and X. Su, "Novel approach for synthesis of boehmite nanostructures and their conversion to aluminum oxide nanostructures for remove Congo red," *J. Colloid Interface Sci.*, vol. 452, pp. 116–125, 2015.

[88] M. Teixeira *et al.*, "Boehmite-phenolic resin carbon molecular sieve membranes—Permeation and adsorption studies," *Chem. Eng. Res. Des.*, vol. 92, no. 11, pp. 2668–2680, 2014.

[89] C.-Y. Yang, W. Y. Shih, and W.-H. Shih, "Gelation, Consolidation, and Rheological Properties of Boehmite-Coated Silicon Carbide Suspensions," *J. Am. Ceram. Soc.*, vol. 83, no. 8, pp. 1879–1884, 2000.

[90] C.-Y. Yang and W.-H. Shih, "Effect of Acid on the Coating of Boehmite onto Silicon Carbide Particles in Aqueous Suspensions," *J. Am. Ceram. Soc.*, vol. 82, no. 2, pp. 436–440, 1999.

[91] M. V. Twigg and J. T. Richardson, "Fundamentals and applications of structured ceramic foam catalysts," *Ind. Eng. Chem. Res.*, vol. 46, no. 12, pp. 4166–4177, 2007.

[92] F. Granados-Correa and J. Jiménez-Becerril, "Chromium (VI) adsorption on boehmite," *J. Hazard. Mater.*, vol. 162, pp. 1178–1184, 2009.

[93] T. J. Webster, E. L. Hellenmeyer, and R. L. Price, "Increased osteoblast functions on theta+delta nanofiber alumina," *Biomaterials*, vol. 26, no. 9, pp. 953–960, 2005.

[94] R. L. Price, L. G. Gutwein, L. Kaledin, F. Tepper, and T. J. Webster, "Osteoblast function on nanophase alumina materials: Influence of chemistry, phase, and topography.," *J. Biomed. Mater. Res. A*, vol. 67, no. 4, pp. 1284–93, 2003.

[95] X. Y. C. and H. S. H. and S. W. Lee, "Hydrothermal synthesis of boehmite (γ-AlOOH) nanoplatelets and nanowires: pH-controlled morphologies," *Nanotechnology*, vol. 18, no. 28, p. 285608, 2007.

[96] P. D. S. Santos, A. C. V. Coelho, H. D. S. Santos, and P. K. Kiyohara, "Hydrothermal synthesis of well-crystallised boehmite crystals of various shapes," *Mater. Res.*, vol. 12, no. 4, pp. 437–445, 2009.

[97] C. S. Chi *et al.*, "Transition of hydrated oxide layer for aluminum electrolytic capacitors," *Mater. Sci. Eng. A*, vol. 448–451, pp. 314–317, 2007.

[98] A. C. Geiculescu and T. F. Strange, "Aluminum oxide thin dielectric film formation under elevated gravity conditions," *Thin Solid Films*, vol. 503, no. 1–2, pp. 45–54, 2006.

[99] S. Castet, J.-L. Dandurand, J. Schott, and R. Gout, "Boehmite solubility and aqueous aluminum speciation in hydrothermal solutions (90–350 °C): Experimental study and modeling," *Geochim. Cosmochim. Acta*, vol. 57, no. 20, pp. 4869–4884, 1993.

[100] E. I. Shkolnikov, N. S. Shaitura, and M. S. Vlaskin, "Structural properties of boehmite produced by hydrothermal oxidation of aluminum," *J. Supercrit. Fluids*, vol. 73, pp. 10–17, 2013.

[101] D. Mishra, S. Anand, R. K. Panda, and R. P. Das, "Hydrothermal preparation and characterization of boehmites," *Mater. Lett.*, vol. 42, no. January, pp. 38–45, 2000.

[102] Y. H. An and R. J. Friedman, *Handbook of Bacterial Adhesion: Principles, Methods, and Applications*. 2010.

[103] X. Shi, D. Graiver, and R. Narayan, "Hydrolysis and Condensation of Hydrophilic Alkoxysilanes Under Acidic Conditions," *Silicon*, vol. 4, no. 2, pp. 109–119, 2012.

[104] Mario Birkholz, P. F. Fewster, and C. Genzel, *Thin Film Analysis by X-Ray Scattering*. 2006.

[105] V. Srot, M. Gec, P. A. van Aken, J. H. Jeon, and M. Čeh, "Influence of TEM specimen preparation on chemical composition of $Pb(Mg_{1/3}Nb_{2/3})O_3$-$PbTiO_3$ single crystals," *Micron*, vol. 62, pp. 37–42, 2014.

[106] E. Peeters, H. J. Nelis, and T. Coenye, "Comparison of multiple methods for quantification of microbial biofilms grown in microtiter plates," *J. Microbiol. Methods*, vol. 72, no. 2, pp. 157–165, 2008.

[107] J. Harvey, K. P. Keenan, and A. Gilmour, "Assessing biofilm formation by *Listeria monocytogenes* strains," *Food Microbiol.*, vol. 24, no. 4, pp. 380–392, 2007.

[108] C. Vargel, M. Jacques, and M. P. Schmidt, *Corrosion of Aluminium*. 2004.

[109] R. D. Armstrong and V. J. Braham, "The mechanism of aluminium corrosion in alkaline solutions," *Corros. Sci.*, vol. 38, no. 9, pp. 1463–1471, 1996.

[110] H. G. Yang *et al.*, "Anatase TiO_2 single crystals with a large percentage of reactive facets," *Nature*, vol. 453, no. 7195, pp. 638–641, 2008.

[111] G. Liu, C. Sun, S. C. Smith, L. Wang, G. Q. (Max) Lu, and H.-M. Cheng, "Sulfur doped anatase TiO_2 single crystals with a high percentage of {001} facets," *J. Colloid Interface Sci.*, vol. 349, no. 2, pp. 477–483, 2010.

[112] H. Zhang *et al.*, "Anatase TiO_2 crystal facet growth: Mechanistic role of hydrofluoric acid and photoelectrocatalytic activity," *ACS Appl. Mater. Interfaces*, vol. 3, no. 7, pp. 2472–2478, 2011.

[113] M.-V. Sofianou *et al.*, "Solvothermal synthesis and photocatalytic performance of Mg^{2+}-doped anatase nanocrystals with exposed {001} facets," *Catal. Today*, vol. 230, pp. 125–130, 2014.

[114] A. Abram, A. Eršte, G. Dražić, and V. Bobnar, "Structural and dielectric properties of hydrothermally prepared boehmite coatings on an aluminium foil," *J. Mater. Sci. Mater. Electron.*, vol. 27, no. 10, pp. 10221–10225, 2016.

[115] Y. Mathieu, B. Lebeau, and V. Valtchev, "Control of the morphology and particle size of boehmite nanoparticles synthesized under hydrothermal conditions.," *Langmuir*, vol. 23, no. 18, pp. 9435–42, 2007.

[116] L. Liu, F. Xu, Z. Yu, and P. Dong, "Facile fabrication of non-sticking superhydrophobic boehmite film on Al foil," *Appl. Surf. Sci.*, vol. 258, no. 22, pp. 8928–8933, 2012.

[117] Y. F. Zhu, D. H. Fan, and W. Z. Shen, "Template-Free Synthesis of Zinc Oxide Hollow Microspheres in Aqueous Solution at Low Temperature," *J. Phys. Chem. C*, vol. 111, no. 50, pp. 18629–18635, 2007.

[118] K. Thongsuriwong, P. Amornpitoksuk, and S. Suwanboon, "The effect of aminoalcohols (MEA, DEA and TEA) on morphological control of nanocrystalline ZnO powders and its optical properties," *J. Phys. Chem. Solids*, vol. 71, no. 5, pp. 730–734, 2010.

[119] Y. H. Ni, X. W. Wei, X. Ma, and J. M. Hong, "CTAB assisted one-pot hydrothermal synthesis of columnar hexagonal-shaped ZnO crystals," *J. Cryst. Growth*, vol. 283, no. 1–2, pp. 48–56, 2005.

[120] A. Moulahi and F. Sediri, "Pencil-like zinc oxide micro/nano-scale structures: Hydrothermal synthesis, optical and photocatalytic properties," *Mater. Res. Bull.*, vol. 48, no. 10, pp. 3723–3728, 2013.

[121] K. Bohinc *et al.*, "Metal surface characteristics dictate bacterial adhesion capacity," *Int. J. Adhes. Adhes.*, vol. 68, pp. 39–46, 2016.

[122] A. Nostro, M. A. Cannatelli, G. Crisafi, A. D. Musolino, F. Procopio, and V. Alonzo, "Modifications of hydrophobicity, *in vitro* adherence and cellular aggregation of *Streptococcus mutans* by *Helichrysum italicum* extract," *Lett. Appl. Microbiol.*, vol. 38, no. 5, pp. 423–427, 2004.

[123] K. P. Lemon, D. E. Higgins, and R. Kolter, "Flagellar motility is critical for *Listeria monocytogenes* biofilm formation," *J. Bacteriol.*, vol. 189, no. 12, pp. 4418–4424, 2007.

[124] M. Katsikogianni and Y. F. Missirlis, "Concise review of mechanisms of bacterial adhesion to biomaterials and of techniques used in estimating bacteria-material interactions," *Eur. Cells Mater.*, vol. 8, no. August, pp. 37–57, 2004.

[125] L. C. Hsu, J. Fang, D. A. Borca-Tasciuc, R. W. Worobo, and C. I. Moraru, "Effect of micro- and nanoscale topography on the adhesion of bacterial cells to solid surfaces," *Appl. Environ. Microbiol.*, vol. 79, no. 8, pp. 2703–2712, 2013.

[126] K. Myszka and K. Czaczyk, "Bacterial biofilms on food contact surfaces - a review," *Polish J. Food Nutr. Sci.*, vol. 61, no. 3, pp. 173–180, 2011.

[127] I. Carvalho, M. Henriques, and S. Carvalho, "New strategies to fight bacterial adhesion," *Microb. Pathog. Strateg. Combat. them Sci. Technol. Educ.*, pp. 170–178, 2013.

Bibliography

Journal Articles

K. Bohinc, G. Dražić, A. Abram, M. Jevšnik, B. Jeršek, D. Nipič, M. Kurinčič and P. Raspor, "Metal surface characteristics dictate bacterial adhesion capacity," *International journal of adhesion and adhesives*, vol. 68, p. 39-46, 2016.

A. Abram, A. Eršte, G. Dražić, V. Bobnar, "Structural and dielectric properties of hydrothermally prepared boehmite coatings on an aluminium foil," *Journal of materials science: Materials in electronics*, vol. 27, no. 10, p. 10221-10225, 2016.

D. Kovačević, R. Pratnekar, K. Godič Torkar, J. Salopek, G. Dražić, A. Abram, K. Bohinc, "Influence of polyelectrolyte multilayer properties on bacterial adhesion capacity," *Polymers*, vol. 8, no. 10, p. 345-1-345-12, 2016.

Conference Paper

K. Bohinc, Á. Deák, K. Godič Torkar, G. Dražić. A. Abram, L. Janovák, I. Dékány "Bacterial adhesion to material surfaces covered by thin films," EURADH 2016 and *Adhesion '16: 11th European Adhesion Conference and 13th International Triennial Conference on the Science and Technology of Adhesion and Adhesives*, Glasgow, UK, 2016. IOM Communications, 2016, p. 54-57.

T. Zabukovec Jezovšek, M. Bele, A. Abram, M. Gaberšček and G. Dražić, "Characterisation of solvothermally synthesised fibrous TiO_2/Au," *12th Multinational Congress on Microscopy*, Eger, Hungary, 2015.

A. Abram, N. Daneu and G. Dražić, "Morphology and surface properties of hydrothermally prepared boehmite/TiO_2 coating on aluminium," *SPASEC-20, The 20th International Conference on Semiconductor Photocatalysis and Solar Energy Conversion*, San Diego, California, 2015.

A. Abram and G. Dražić, "Preparation of hydrophobic zinc substrates by solvothermal route," *22. mednarodna konferenca o materialih in tehnologijah*, Portorož, Slovenija, 2014.

A. Abram and G. Dražić, "Hydrothermal synthesis of TiO_2 photocatalytic coatings on aluminium," *The 2nd International Conference on Photocatalytic and Advanced Oxidation Technologies for Treatment of Water, Air, Soil and Surfaces, (PAOT-2)*, Gdansk, Poland, 2013.

G. Dražić, B. Horvat, M. Krivec and A. Abram, "Photocatalytic TiO_2 - from hierarchical structures to a microreactor," *4rd IC4N - 2013, 4rd International Conference from Nanoparticles & Nanomaterials to Nanodevices and Nanosystems and NanoTechnology Transfer Workshop on: from the Lab to the Marketplace*, Corfu, Greece, 2013.

A. Abram and G. Dražić, "Photocatalytic activity of hydrothermal prepared TiO_2 coatings on aluminum," *3rd European Symposium on Photocatalysis*, Portorož, Slovenia, 2013.

A. Abram and G. Dražić, "Hydrothermal passivation of zinc substrates." *PSS2013, Photocatalytic and Superhydrophilic Surface Workshop*, Manchester, UK, 2013.

Work Reports

A. Abram, V. Kevorkijan, P. Cvahte and G. Dražić, "Hidrotermalna priprava fotokatalitičnih prevlek na aluminiju, (IJS delovno poročilo, 11719)," 2014.
A. Abram, B. Borota, V. Vrečko and G. Dražić, "Hidrotermalna priprava funkcionalnih prevlek na cinku, (IJS delovno poročilo, 11720)," 2014.

Biography

The author of this thesis was born in 1986 and completed his Matura exam in 2005 on Gimanzija Nova Gorica. He enrolled in the program "Material Science" at the Faculty of Natural Sciences and Engineering, University of Ljubljana in the same year. He graduated under the mentorship of Prof. Dr. Boštjan Markoli. During his undergraduate studies he was actively participating in the development of new LTCC composites and studies of Ruthenium-based systems at the Electronic ceramics department at the "Jožef Stefan" Institute. He started his PhD in 2012 under the mentorship of Asst. Prof. Dr. Goran Dražić at the Department of Nanostructured Materials at the "Jožef Stefan" Institute. He is the author and co-author of five publications in the international journals with impact factor. He will continue to work with TiO_2 and surface treatment techniques on biomaterials and dental ceramics in the scope of P2-0087 program "Engineering and bio-ceramics" at the "Jožef Stefan" Institute.